Guest effects on the solid-state dynamics of selected inclusion compounds

by Emile R. Engel

Submitted in partial fulfilment of the requirements for the degree
Doctor of Philosophy

Promoter: Prof. Leonard J. Barbour

Department of Chemistry and Polymer Science

Faculty of Science

University of Stellenbosch

December 2016

Declaration

By submitting this dissertation electronically, I declare that the entirety of the work contained therein is my own, original work, that I am the sole author thereof (save to the extent explicitly otherwise stated), that reproduction and publication thereof by Stellenbosch University will not infringe any third party rights and that I have not previously in its entirety or in part submitted it for obtaining any qualification.

December 2016

Abstract

Guest inclusion has always been a central feature of supramolecular chemistry. The present work describes guest effects on particular properties of selected inclusion compounds. Guest replacement is demonstrated as a means of modifying thermal expansion behaviour and porosity. The body of this thesis consists of three manuscripts (two published and one under review).

The first manuscript describes a nitromethane solvate of 18-crown-6 that was investigated by means of temperature-resolved single-crystal X-ray diffraction. The compound exhibits exceptionally large positive thermal expansion in two axial directions and exceptionally large negative thermal expansion along the third. The underlying mechanism relies exclusively on weak electrostatic interactions to yield a linear thermal expansion coefficient of $-129 \times 10^{-6}\,K^{-1}$, which is, to the best of our knowledge, the largest negative value yet recorded for an organic inclusion compound. Our discovery of a reported analogue with acetonitrile led us to prepare an isoskeletal series of compounds for further inquiry.

The second manuscript demonstrates that guest replacement in a series of isoskeletal organic inclusion compounds can produce remarkable changes in thermal expansion behaviour. The three inclusion compounds have 18-crown-6 as host molecule and nitromethane, acetonitrile or iodomethane as guests. Along principal axis X1 the linear component of thermal expansion is negative for the nitromethane and acetonitrile solvates but zero for the iodomethane solvate. The compounds show varying degrees of large volumetric thermal expansion, with coefficients of $378(22)$, $226(3)$ and $256(8) \times 10^{-6}\,K^{-1}$ for the nitromethane, acetonitrile and iodomethane solvates, respectively. Crystal structure analysis and computational methods were used to elucidate general features of the underlying mechanism of thermal expansion for the series. Interestingly, the thermosalient effect was observed for the acetonitrile version. To our knowledge this is the first example of thermosalience reported for an inclusion compound.

The success with molecular organic crystals prompted similar experimentation with a different class of materials. As inorganic inclusion compounds, MOFs are an obvious choice for experiments involving guest replacement because of their proven capability for guest exchange, and the great interest in MOFs as potential porous sorbents for molecular storage and separation in industry.

The final manuscript describes a non-interpenetrated MOF with a paddle-wheel SBU that has been activated by direct thermal evacuation, guest exchange with a volatile solvent, and supercritical CO_2 drying. Conventional thermal activation results in a mixture of crystalline phases and some amorphous content. Exchange with a volatile solvent and subsequent vacuum activation produces a pure breathing phase with high sorption capacity, selectivity for CO_2 over N_2 and CH_4, and substantial hysteresis. Supercritical drying can be used to access a guest-free open phase. Pressure-resolved differential scanning calorimetry was used to investigate the systematic loss of sorption capacity by the breathing phase as a function of successive cycles of sorption and desorption.

Opsomming

Die insluiting van gas molekules is nog altyd ’n sentrale kenmerk van supramolekulere chemie. Hierdie tesis beskryf die effek van verskillende gas molekules op sekere fisiese eienskappe van uitgesoekte multikomponent kristalle. Dit word bewys dat die vervang van gas molekules ’n manier is om termiese uitsetting en poreusheid te manipuleer. Die resultate is beskryf in drie artikels; twee wat gepubliseer is en een wat nog onder hersiening is.

Die eerste artikel beskryf ’n molekulêre kompleks van 18-kroon-6 en nitrometaan wat ondersoek is deur veranderende-temperatuur enkelkristal X-straal diffraksie. Die kompleks ondergaan groot positiewe termiese uitsetting op twee asse en uitsonderlik groot negatiewe termiese uitsetting op die derde as. Die onderligende meganisme van hierdie ongewone termiese uitsetting is eksklusief afhanklik van relatief swak elektrostatiese interaksies wat ’n liniêre termiese uitsettingskoeffisient van $-129 \times 10^{-6}\,K^{-1}$ gee. Sover ons kennis strek is hierdie die grootste negatiewe waarde vir ’n organiese insluitingsverbinding wat nog ooit gepubliseer is.

Die tweede artikel wys dat die vervang van gaste in ’n reeks isostrukturele organiese insluitingsverbindings kan lei tot merkwaardige verkille in termiese uitsetting. Die drie insluitingsverbindings het 18-kroon-6 as gasheer en nitrometaan, asetonitriel en jodometaan as gaste. Op die hoof-as X1 is die liniêre komponent van termiese uitsetting negatief vir die nitrometaan en asetonitriel solvate maar nul vir die jodometaan solvaat. Die komplekse het verskillende grade van groot volumetriese termiese uitsetting, met koeffisiente van $378(22)$, $226(3)$ en $256(8) \times 10^{-6}\,K^{-1}$ vir die nitrometaan, asetonitriel en jodometaan solvate, afsonderlik. Kristalstruktuuranalise en berekeningsmetodes is gebruik om die algemene kenmerke van die onderliggende meganisme van die reeks uit te lig. Dit is interessant dat die “thermosalient” effek opgemerk is vir die asetonitriel solvaat. Sover ons kennis strek is hierdie die eerste voorbeeld van “thermosalience” vir ’n insluitingsverbinding.

Die sukses met molekulêre kristalle het ons aangemoedig om soortgelyke experimente uit te voer met ’n ander klas materiale. As anorganiese insluitingsverbindings is metaal-organiese raamwerke ’n natuurlike keuse vir eksperimente wat gasuitruiling behels, omdat kristalle van die klas oor die algemeen gasuitruiling maklik verduur, asook omdat metaal-organiese raamwerke so bekend is vir hul potensiële industriële gebruik vir die stoor en skeiding van verskeie molekules.

Die finale artikel beskryf ’n nie-geïnterpenetreerde metaal-organiese raamwerk met ‘n skeprat sekondêre bou-eenheid wat geaktiveer is deur direkte termiese ontruiming, gasuitruiling met ‘’n vlugtige oplosmiddel en superkritiese CO_2 aktivering. Gewone termiese aktivering lei tot ’n mengsel van kristallyne fases en ’n amorfiese komponent. Uitruiling met ’n vlugtige oplosmiddel, gevolg deur aktivering teen kamertemperatuur, lei tot ’n “asem haal” fase met ’n hoë kapasiteit vir CO_2 adsorpsie bo N_2 en CH_4 en groot histerese. Differensiële skandeer kalorimetrie met veranderende druk is gebruik om die sistematiese afname in adsorpsiekapasiteit deur die “asem haal” fase as ’n funksie van opeenvolgende siklusse van adsorpsie en desorpsie te ondersoek.

Acknowledgements

I am thankful to Prof. Len Barbour for welcoming me back to his research group after forays elsewhere, and for allowing me to explore my own research ideas and work independently. I have appreciated his excellent mentorship, his thoughts on scientific philosophy and the role of science in society, his encouragement of travel and conference participation, and his kindness in introducing me to a number of inspiring, highly accomplished researchers.

I am immensely grateful my parents, Myrna and Richard, and my brother, Tyrone, for their unwavering support.

I am appreciative of help and support that I received from members of the Supramolecular Materials Research Group, including visiting students and researchers, and support staff. I am especially thankful to Dr Vincent Smith, Phumile Sikiti, Charl Bezuidenhout, Dr Himanshu Aggarwal and Debbie Isaacs for essential scientific, technical and moral support.

I also thank Prof. Mir Wais Hosseini of the University of Strasbourg for hosting me as a visiting PhD student, Dr Abdelaziz Jouaiti for incredibly kind supervision, and, for help and amazing hospitality, the members of the Molecular Tectonics Laboratory, especially Dimby Rasoloarison.

I acknowledge the National Research Foundation, the Wilhelm Frank Trust and the French Embassy in South Africa for funding.

This work is dedicated to my grandparents.

Publications

1. E. R. Engel, V. J. Smith, C. X. Bezuidenhout, L. J. Barbour, Uniaxial Negative Thermal Expansion Facilitated by Weak Host–guest Interactions, *Chem. Commun.* **2014**, *50*, 4238–4241.
2. E. R. Engel, V. J. Smith, C. X. Bezuidenhout, L. J. Barbour, Thermoresponsive Organic Inclusion Compounds: Modification of Thermal Expansion Behavior by Simple Guest Replacement, *Chem. Mater.* **2016**, *28*, 5073–5079.
3. Emile R. Engel, Abdelaziz Jouaiti, Charl X. Bezuidenhout, Mir Wais Hosseini, Leonard J. Barbour, Activation-dependent Breathing in a Flexible Metal-organic Framework and the Effects of Repeated Sorption/Desorption Cycling. *Manuscript under review*.

Conferences

1. 1st Strasbourg Summer School: Challenges in Supramolecular Chemistry in Strasbourg, France on 8 to 12 September 2014. Poster: *Negative thermal expansion facilitated by weak host-guest interactions*.
2. Pan African and South African Meeting of the International Year of Crystallography: IYCr2014Africa in Bloemfontein, South Africa on 12-17 October 2014. Poster: *Negative thermal expansion facilitated by weak host-guest interactions*.
3. 1st Meeting on Porous Molecular Solids in Stellenbosch, South Africa on 9-10 April 2015. Poster: *Accessing porous phases of a metal-organic framework by solvent exchange.*
4. 15th International Seminar on Inclusion Compounds in Warsaw, Poland on 17-21 August 2015. Poster: *Large guest-dependent anisotropic thermal expansion in a series of organic inclusion compounds*.
5. 29th European Crystallographic Meeting in Rovinj, Croatia on 23-28 August 2015. Poster: *Large guest-dependent anisotropic thermal expansion in a series of organic inclusion compounds*.

Abbreviations

DMF	Dimethyl formamide
DSC	Differential scanning calorimetry
Et_2O	Diethyl ether
EtOAc	Ethyl acetate
MOF	Metal-organic framework
NTE	Negative thermal expansion
PTE	Positive thermal expansion
PXRD	Powder X-ray diffraction
SBU	Secondary building unit
s-CO_2	Supercritical carbon dioxide
TGA	Thermogravimetric analysis

Atom colour key


Carbon


Hydrogen


Oxygen


Nitrogen


Zinc


Iodine


Chlorine

Table of contents

Chapter 1
Introduction

1.1 Supramolecular materials

The modern discipline of supramolecular chemistry uses non-covalent interactions to construct large, multi-molecular architectures. As a research field it emerged with the work of Charles Pederson on the discovery of crown ethers and their binding of alkali cations,[1,2] and shortly thereafter the work of Jean-Marie Lehn on cryptands[3,4] and Donald Cram on spherands.[5,6] Lehn referred to supramolecular chemistry in 1978 as "the chemistry of molecular assemblies and of the intermolecular bond".[7] Later, in his Nobel Prize lecture of 1988, he described the field as "covering the structures and functions of the entities formed by association of two or more chemical species".[8]

Supramolecular chemistry research has drawn much inspiration from naturally-occurring macromolecular structures, since biological processes such as protein folding, enzyme-substrate binding and the zipping and unzipping of DNA all rely on non-covalent intermolecular interactions. In recent years the field has matured beyond the probing of supramolecular interactions to facilitating our current understanding for the development of supramolecular materials with appealing properties such as molecular separation and storage, negative thermal expansion, sensing and catalysis.

1.2 Supramolecular interactions

A wide range of chemical interactions are exploited in the design and synthesis of supramolecular materials but directional interactions are generally most useful for the purpose of rational design. The strong directional interactions that are of particular importance in this thesis are coordination linkages and hydrogen bonds. Weaker interactions that are of relevance here include π interactions, dipole-dipole interactions and London dispersion forces. The danger of overstating the directing effect of weak intermolecular interactions on the basis of crystal packing alone is noted.[9] As such, discussions about weak intermolecular interactions herein have been accompanied by calculated relative interaction energies.

1.2.1 Hydrogen bonds

The term hydrogen bond was first used by Pauling in his investigation of the structure and entropy of ice,[10] and he later estimated the energy of this particular hydrogen bond in the Nature of the Chemical Bond.[11] The hydrogen bond is a directional interaction between a proton donor and a proton acceptor moiety. It takes the form D-H···A where D is the

hydrogen bond *donor* and A the electrostatically negative *acceptor* atom, which usually has a lone pair. The hydrogen bond angle ∠DHA typically approaches 180° for strong interactions. The IUPAC defines the hydrogen bond formally as "…an attractive interaction between a hydrogen atom from a molecule or a molecular fragment D-H in which D is more electronegative than H, and an atom or group of atoms in the same or different molecule in which there is evidence of bond formation."[12]

Desiraju popularised the term 'supramolecular synthon' as an analogy to synthons in reticular synthetic organic chemistry.[13] They are common organic intermolecular interactions observed in single-crystal X-ray structures, mostly based on hydrogen bonding motifs. Some examples are illustrated in Figure 1.

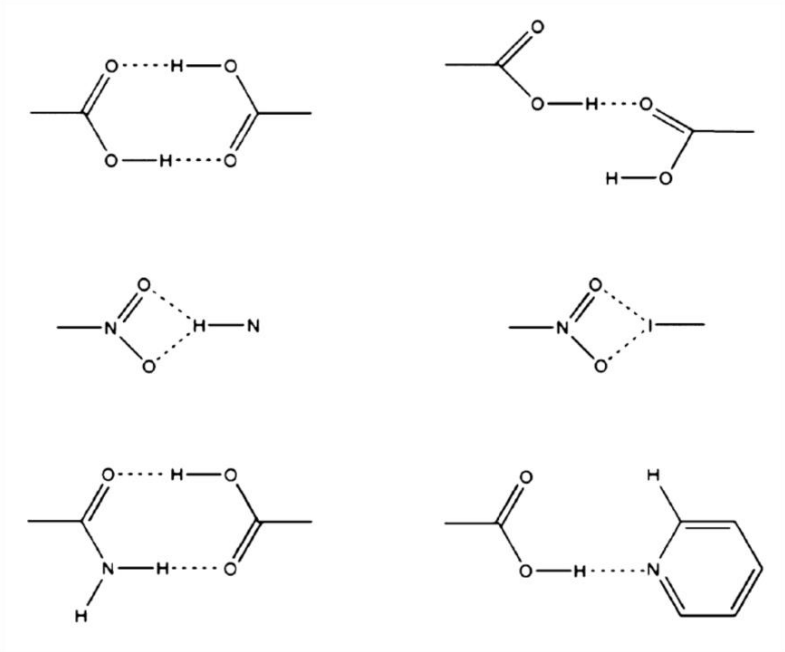

Figure 1. Representative supramolecular synthons as described by Desiraju.[14]

Energy calculations by Dunitz and Gavezzoti provided some quantitative insight into the limitations of supramolecular synthons as a predictive tool.[15] In particular they found that, where weak interactions are abundant, they compete with hydrogen bonding and supramolecular synthon geometries become less regular.

In determining crystal structures by single-crystal X-ray crystallography, hydrogen atoms are generally placed using a riding model because the assignment of hydrogen positions based on difference electron density peaks has long been considered dubious. Where accurate hydrogen positions are needed, neutron diffraction is usually employed. We have followed the convention of placing hydrogen atoms using riding models and considering only D-A distances when assessing hydrogen bond lengths. Importantly, recent evidence suggests

that it is in fact possible to assign accurate hydrogen positions from single-crystal X-ray data using Hirshfeld atom refinement.[16]

1.2.2 Coordination linkages

The bonds formed between ligand donor atoms and metal ions are generally of similar strength or weaker than covalent bonds but much stronger than hydrogen bonds. While the strengths of metal-ligand coordination bonds are difficult to estimate accurately, it is known that bond lengths for anionic ligands with N and O donor atoms are approximately 0.2-0.5 Å shorter than for the identical neutral ligand.[17] Yaghi and co-workers have reported estimated bond energies for Zn-O in MOF-5 as very strong at 360 kJ mol^{-1}, Cu-O in paddle-wheel type frameworks at 186 kJ mol^{-1} and Cu(I)-N at 55 kJ mol^{-1} and Cu(II)-N at 90 kJ mol^{-1}, based on heats of formation of $CuCl{\cdot}3NH_3$ and $CuCl_2{\cdot}2NH_3$.[18]

1.2.3 Dipole-dipole stabilisation

Hydrogen bonds are a subset of dipole-dipole interactions. In general dipole-dipole interactions occur between molecules that have permanent dipoles based on an electronegativity difference between atoms. The partial negative charge of one molecule is generally stabilised by an interaction with the partially positive atom of an adjacent molecule in a manner similar to the two examples for iodine monochloride given in Figure 2.

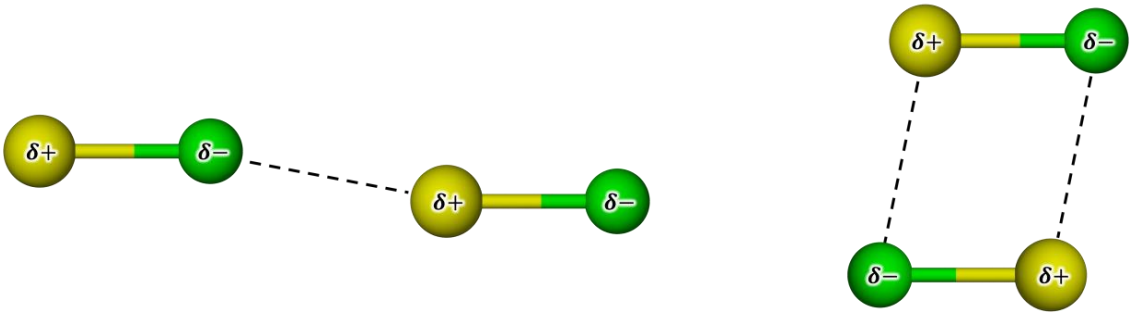

Figure 2. Schematic illustration of possible dipole-dipole interactions for iodine monochloride.

1.2.4 London dispersion forces

London dispersion forces (after Fritz London) or van der Waals forces are the weakest electrostatic interactions and are non-directional.[19,20] The proximity of one molecule to another will induce polarisation either by repulsion of the two electron clouds or attraction of the electron cloud of one molecule to an adjacent nucleus of the other. This induced dipole effect is mostly very weak and rapidly fluctuating but is sufficiently strong to create the overall effect of intermolecular attraction.

1.2.5 π interactions

By π interactions we refer particularly to interactions involving the π surfaces of aromatic rings. Benzene has a quadrupole moment with the large face of the ring being electrostatically negative and its narrow edges electrostatically positive. In the solid state aromatic moieties frequently interact by face-to-face stacking, offset parallel stacking or by an edge-to-face C-H···π interaction. The quadrupole moment of benzene and typical geometries of aromatic interactions are illustrated in Figure 3.

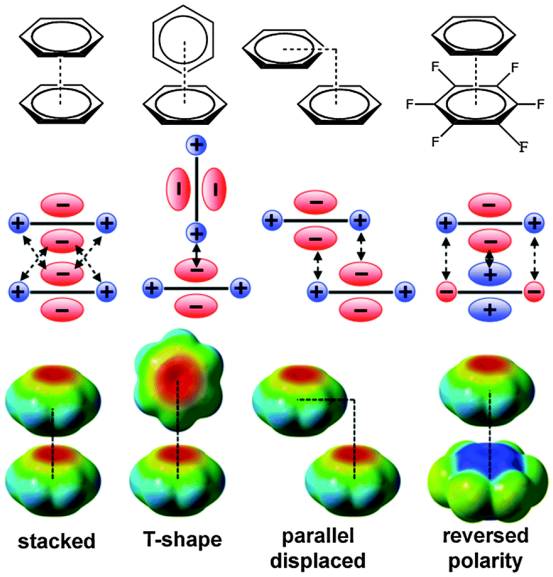

Figure 3. Typical geometries of aromatic π interactions with quadrupole moments schematically depicted. Electrostatic surface potentials are shown with areas of positive potential in blue and areas of negative potential in red. Figure reproduced from Matthews *et al.*[21]

1.3 Inclusion compounds

In 1977 Cram and co-workers described molecular complexes[22] as "composed of two or more molecules or ions held together in unique structural relationships by electrostatic forces other than those of full covalent bonds or of ionic crystals…molecular complexes are usually held together by hydrogen bonding, by ion pairing, by π acid to π base interactions, by metal to ligand binding, by van der Waals attractive forces, by solvent reorganising, and by partially made and broken covalent bonds (transition states)." Host-guest complexes are defined in the same article; the host molecule (or ion) is referred to as having *convergent* binding sites, while the guest is said to have *divergent* binding sites.

Cram and contemporaries had at the time conceived of molecular organic hosts but since then, in practice and by definition, the category of inclusion compound has expanded to include inorganic and polymeric hosts. The IUPAC defines an inclusion compound or complex as "a complex in which one component (the host) forms a cavity or, in the case of a crystal, a crystal lattice containing spaces in the shape of long tunnels or channels in which

molecular entities of a second chemical species (the guest) are located. There is no covalent bonding between guest and host, the attraction being generally due to van der Waals forces. If the spaces in the host lattice are enclosed on all sides so that the guest species is 'trapped' as in a cage, such compounds are known as clathrates or 'cage compounds'."[23]

In supramolecular synthesis, inclusion compounds are most commonly formed when a host compound crystallises from a solution or reaction mixture containing the host and guest. Slow evaporation from the solution is the simplest version of this. The host is dissolved in the guest solvent and the solvent is allowed to evaporate slowly, which drives crystallisation of the inclusion compound. In solvothermal synthesis, typically components that will form a host framework are combined in a solvothermal reaction vessel (Teflon-lined autoclave) with solvent, and the mixture is heated to a relatively high temperature and pressure. Crystals of the inclusion compound form with the reaction solvent as guest.

Calixarenes, pyrogallolarenes and metallocycles are common host molecules. Examples of typical inclusion complexes with these hosts are reproduced in Figure 4. The bowl-shaped *para*-sulfonatocalix[4]arene binds norspermidine (*N*-(3-ammoniopropyl)propane-1,3-diamine) as guest molecule.[24] Pyrogallol[4]arene forms a hexameric capsule containing 3 molecules of pyrene when the components are melted together and cooled.[25] The Ag metallocycle with toluene as guest was obtained from the as-synthesised version by guest exchange.[26]

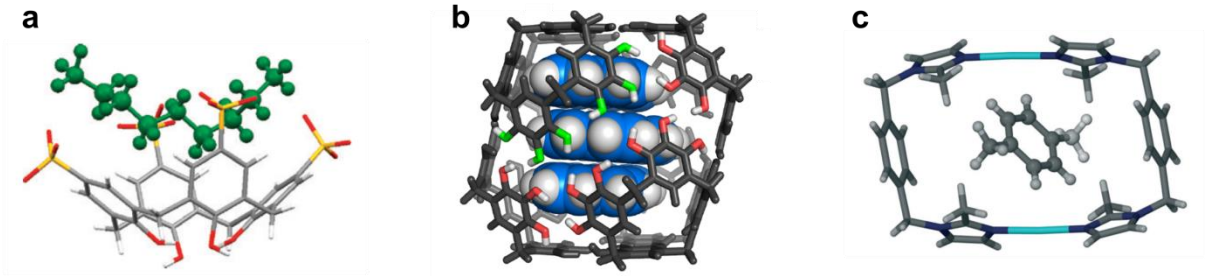

Figure 4. Typical inclusion compounds: (a) *para*-sulfonatocalix[4]arene with norspermidine (single-crystal X-ray structure), (b) pyrogallolarene hexameric capsule containing pyrene molecules (molecular model) and (c) Ag metallocycle with disordered toluene guest (single-crystal X-ray structure). Figures reproduced from Danylyuk *et al.*,[24] Chapin *et al.*[25] and Du Plessis *et al.*[26] respectively.

1.3.1 Similarities in crystal packing

Different inclusion compounds often have the same or similar crystal structures. It is worth distinguishing between often-conflated terms that are used in reference to similarities in crystal packing: isostuctural, isotypic, isoskeletal and isomorphous.

Isostructural crystals are those that have similar crystal structures but not necessarily identical chemical compositions, unit cell dimensions or symmetry (space groups). The definition includes but is not limited to inclusion compounds that fulfil these criteria. The IUCr

has restricted the interpretation of similarity when comparing two potentially isostructural crystals to “a 'comparable' variability in the atomic coordinates to that of the cell dimensions and chemical composition.”[27] The terms isotypic and isostructural are synonymous.

Isoskeletal refers to a series of inclusion compounds where the host framework remains unchanged. It can be considered a special case of isostructurality where the guest may be ignored.[28] This category incorporates cases where the host-guest ratios vary substantially and where the guest is greatly disordered in some members of the series.

The native cyclodextrins are a well-known class of compounds that commonly occur in isostructural series.[29] The term isoskeletal was first introduced by our group to describe a diol host for which a self-inclusion complex was isolated in addition to several solvates with identical host structures.[30]

Isormorphous crystals are essentially crystallographically identical except for their molecular compositions. The IUCr defines isomorphous crystals as follows: “(a) both have the same space group and unit cell dimensions and (b) the types and the positions of atoms in both are the same except for a replacement of one or more atoms in one structure with different types of atoms in the other (diadochy), such as heavy atoms, or the presence of one or more additional atoms in one of them (isomorphous addition). Isomorphous crystals can form solid solutions.”[31]

1.3.2 Crown ethers

Crown ethers or cyclic polyethers became prominent when Pederson developed a simple method of synthesis. The first crown ether, dibenzo-18-crown-6 is shown in Figure 5 along with the unsubstituted cyclic oligomers of ethylene oxide. The crown ethers were revolutionary for their capability of binding alkali metal cations and solubilising ionic species in hydrocarbon solvents. The common name was inspired by the shape of the first crown ether complexes obtained, wherein the host appears to ‘crown’ the cation.[2]

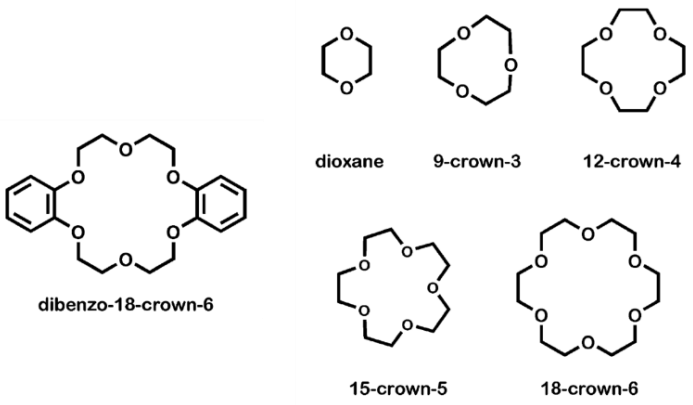

Figure 5. Dibenzo-18-crown-6 and a series of cyclic oligomers of ethylene oxide. Figure reproduced from Gokel *et al.*[32]

Arguably the most commonly used crown ether is 18-crown-6. It is a very hygroscopic solid under ambient conditions and has a low melting point (37-40 °C). In addition to its utility as a cation binder it has also been used for the inclusion of neutral molecules. The first known example is a complex with acetonitrile that was discovered as a means of purification of the host.[32] Other neutral 18-crown-6 complexes include those with urea,[33] formamide, *N*-methylthiourea and 3-nitrophenol as guests.[34]

1.3.3 Inorganic inclusion complexes

Polyoxometallates, including natural and synthetic zeolites, are a broad class of inorganic hosts.[35] Zeolites are hydrated alkaline or alkaline-earth aluminosilicates with the general formula $Mn^{n+}_{x/n}[(AlO_2)_x(SiO_2)_y]^{x-}\cdot wH_2O$.[36] Over several decades of research they have proven extremely versatile as microporous solids. Among the many capabilities of zeolites are catalysis, molecular separation and metal cation capture.[37,38] Day and co-workers reported the anionic inclusion complex $(V_{12}O_{32}^{4-})\cdot CH_3CN$ as the first molecular analogue of zeolites.[39] The vanadate host forms a basket-like cage within which the guest is suspended.

Bidentate methyl-imidazole-based ligands have been used to prepare relatively robust porous metallocycles forming one-dimensional channels.[40,41] Single crystals survived a variety of guest exchange experiments very well.

Among the most important classes of modern inorganic supramolecular hosts are coordination polymers and coordination networks. These are extended polymeric assemblies of metallic nodes or inorganic clusters connected by multidentate ligands.

The terms metal-organic framework (MOF), coordination network and coordination polymer are often used interchangeably but according to IUPAC recommendations[42] there are subtle differences. A coordination polymer is defined as “a coordination compound continuously extending in 1, 2 or 3 dimensions through coordination bonds”. A coordination network is “A coordination compound extending, through repeating coordination entities, in 1 dimension, but with cross-links between two or more individual chains, loops, or spiro-links, or a coordination compound extending through repeating coordination entities in 2 or 3 dimensions.” A metal-organic framework is “a coordination network with organic ligands containing potential voids.” MOFs and porous coordination polymers[43] are essentially the same.

1.4 Porosity

Porosity in supramolecular chemistry refers to the existence of pores (cavities, voids, channels) in a material that may or may not be occupied by guest species. Quantitatively it is defined as ε, the ratio of total pore volume to the total volume of the material (excluding

interparticle voids). Naturally the value of ε will depend on the size of the molecular probe, whether theoretical or experimental, that is used to determine pore volume. Materials with pores less than 2 nm in diameter are termed microporous, while mesoporous and macroporous materials are those with diameters of 2-50 nm and more than 50 nm, respectively.[44]

Molecular inclusion complexes containing solvent molecules are called solvates. Nassimbeni described the processes of complex formation and desolvation according to Figure 6.[45] The α-phase or apohost is the pure host compound. When dissolved in some solvent and allowing for crystallisation the host and guest form an inclusion compound – the β-phase – upon crystallisation. When the guest is released the outcome is a return to the α-phase, a new inclusion compound called the γ–phase or a β_0-phase where the host framework of the β-phase remains intact when guest molecules are lost. The β_0-phase is the highly desirable porous phase. Although it is rare for a hydrogen-bonded solvate host framework to remain intact after guest release, the template strategy illustrated here has been widely used in supramolecular chemistry for the preparation of both organic and inorganic porous materials, including extended networks.

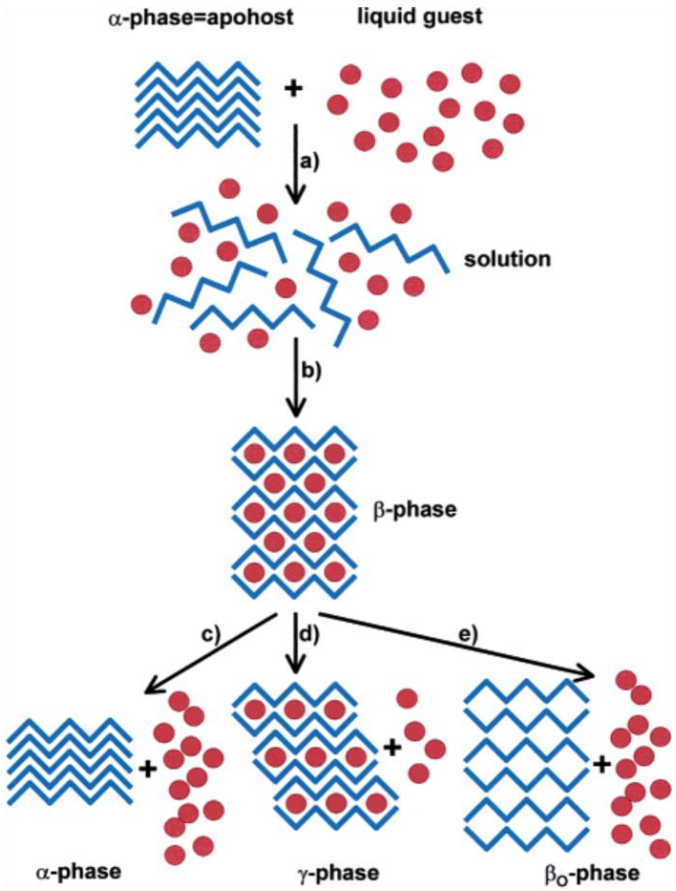

Figure 6. Schematic representation of the formation and decomposition of host-guest compounds. Figure reproduced from Nassimbeni.[45]

Porosity has been classified according to dimensionality by Kitagawa *et al.* as illustrated in Figure 7.[43] Zero-dimensional pores are isolated or walled-off voids. One-dimensional porosity refers to non-intersecting channels, while two-dimensional porosity exists in assemblies of separate layers. Three-dimensional porosity constitutes a system of intersecting channels.

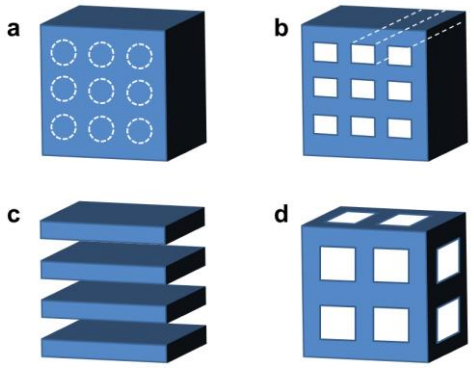

Figure 7. Dimensionality of porosity as defined with respect to porous coordination polymers. The four categories are: (a) zero-dimensional, (b) one-dimensional, (c) two-dimensional and (d) three-dimensional porosity. Figure adapted from Kitagawa *et al.*[43]

Barbour has offered guidelines for proving that a material is indeed porous:[46] "(1) Permeability should be demonstrated because the words ''permeable'' and ''porous'' are practically synonymous; (2) In order to be meaningful, the term ''porous'' should apply to a specific host phase and not simply to the host molecules as an amorphous or mutating collective. Therefore, in principle, the host framework should remain substantially unaffected by guest uptake and removal."

1.5 Metal-organic frameworks

The first reported coordination network, and a precursor to MOFs, was the Hoffman complex by Hoffman and Küspert.[47] It has the molecular formula $[Ni(CN)_2NH_3 \cdot C_6H_6]_n$ and its crystal structure was determined by Powell and Rayner who revealed the two-dimensional square polymer arrangement as well as the existence of benzene as guest molecules in channels formed by the host.[48,49]

Hoskins and Robson produced what is regarded as the first three-dimensional coordination network with extended organic ligands.[50] The compound had Cu(I) as a tetrahedral metallic node and 4,4',4",4"'-tetracyanotetraphenylmethane as a three-dimensional organic linker. The compound trapped nitrobenzene in channels during synthesis.

More recently the design and construction of MOFs has benefited from modular constructions such as secondary building units (SBUs)[51,52] and molecular tectons.[35,53] The

main strategy for rational synthesis of MOFs involves a system of inorganic nodes and organic spacers or connectors and linkers that can be interchanged.[43,54]

Inorganic SBUs are the metallic clusters in MOFs, including their organic coordinating parts. Organic SBUs are the organic ligands. The key to the SBU concept is that it simplifies MOF construction to the geometry of linking nodes. Examples of common Zn carboxylate and organic SBUs are given in Figure 8. Kitagawa and co-workers recently described a 'soft SBU' that rearranges reversibly (under dry conditions) upon guest removal and uptake.[55]

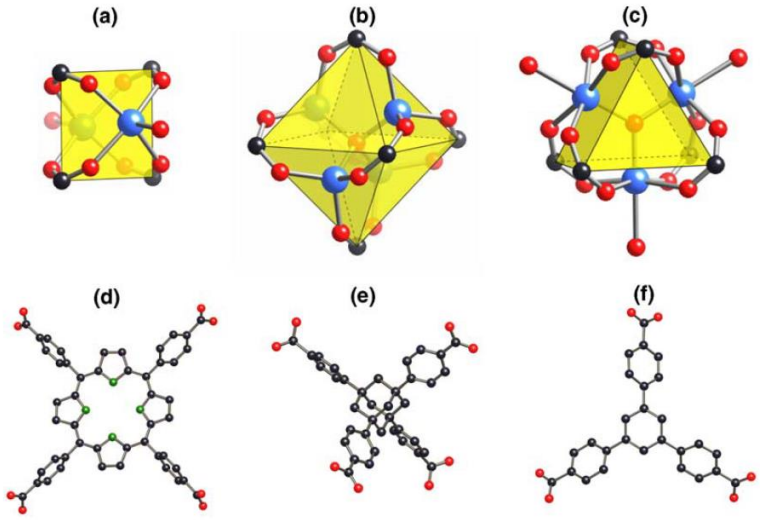

Figure 8. Common Zn-based inorganic SBUs include (a) the square paddle-wheel (b) basic acetate cluster (octahedral), and (c) the oxo-centered trimer with three terminal ligand sites (trigonal prismatic). Examples of organic SBUs include the conjugate bases of (d) square tetrakis(4-carboxyphenyl)porphyrin (square), (e) adamantane-1,3,5,7-tetracarboxylic acid (tetrahedral), and (f) 1,3,5-tris(4-carboxyphenyl)benzene (trigonal). Figure reproduced from Roswell *et al.*[56]

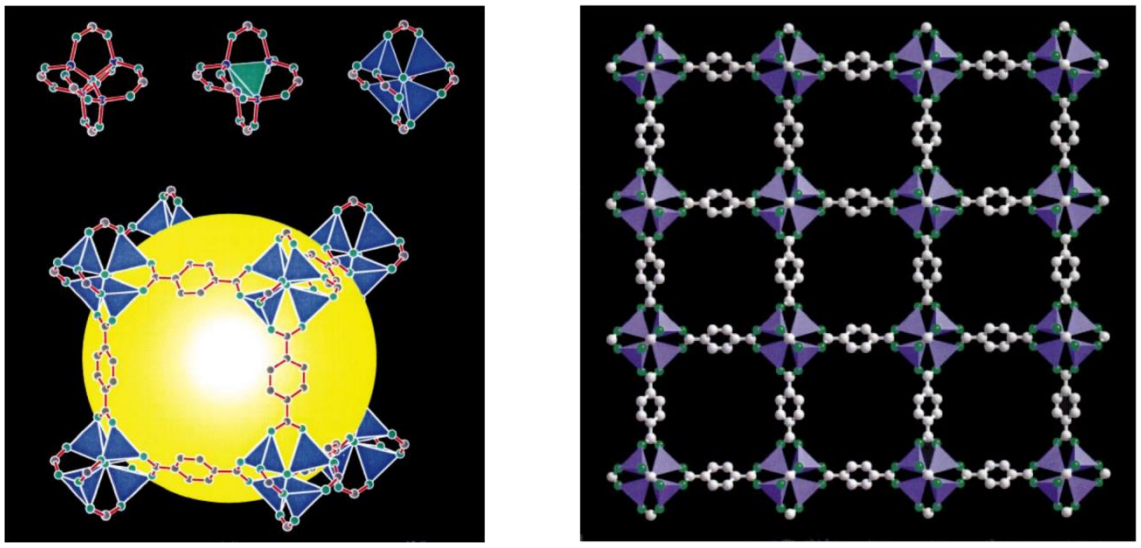

Figure 9. Images based on the crystal structure of MOF-5. Inorganic node or SBU represented as a cluster of tetrahedra (top left), the cubic cavity (bottom left) and packing diagram viewed along [100] (right). The C, O and Zn atoms are represented in grey, green and blue, respectively. The ZnO_4 tetrahedra are blue on the left and purple on the right. Figures reproduced from Yaghi *et al.*[57]

The first report of MOF-5 describing high thermal stability, permanent porosity, unprecedentedly large surface area and a calculated free volume of 55-61% is a great landmark in supramolecular chemistry.[57] Structural aspects of MOF-5 are highlighted in Figure 9. A series based on MOF-5 was systematically synthesised by varying the organic linker. The frameworks in the series are referred to as the isoreticular MOFs or IRMOFs.[58]

A mixed-ligand approach that is typically employed in MOF design and synthesis combines a dicarboxylic acid (e.g. 1,4-benzenedicarboxylic acid, naphthalene-2,6-dicarboxylic acid) with a bis-pyridyl (e.g. 4,4′-bipyridine, 1,2-bis(4-pyridyl)ethylene) to form a paddle-wheel type node (see Figure 8a) with the appropriate metal cation (commonly Zn, Co or Ni).[59]

1.5.1 Interpenetration

When two or more nets of a MOF are linked in such a way that they cannot be disentangled without breaking coordination or covalent bonds, the structure is said to be interpenetrated. Interpenetrated MOFs are three-dimensional analogues of catenanes and rotaxanes.

Various methods have been developed to control interpenetration. It has been shown that lowering the concentration of the reaction mixture can produce a non-interpentrated phase over a twofold interpenetrated phase.[60] In addition to concentration, Zhang and co-workers used temperature to modulate interpenetration, showing that both factors were influential but for concentrations of 0.025-0.1 M elevated temperature preferentially produced the twofold interpenetrated phase over the non-interpenetrated version.[61] Jiang and colleagues prepared three frameworks with identical SBUs and starting reagents.[62] They were: i) microporous and non-interpenetrated, ii) microporous and twofold interpenetrated and iii) mesoporous and non-interpenetrated. Their results were consistent with previous evidence that the occurrence of interpenetration is favoured by higher reaction temperatures and concentrations but also showed that porosity could be modulated.

Interpenetration can also be controlled by choice of the reaction solvent. Rankine and co-workers prepared a non-interpenetrated MOF from diethyl formamide and later a two-fold interpenetrated version using the same reaction conditions except for the substitution of dimethyl formamide as reaction solvent.[63]

Deshpande *et al.* used the method of post-synthetic modification to synthesise a non-interpenetrated MOF.[64] A ligand with a bulky labile substituent (NH-t*ert*-butoxycarbonyl; NHBOC) is used. The substituent inhibits interpenetration during framework synthesis. After the MOF has been synthesised, the amide is hydrolysed to release the substituent but maintain non-interpenetration (see Figure 10).

Our group recently discovered that MOFs are able to undergo switching of the degree of interpenetration. When MOFs are activated their experimentally-determined surface area is

frequently lower than predicted according to the as-synthesised crystal structure. It has now been determined that one of the causes for this is switching of the degree of interpenetration. MOFs have been shown to switch from non-interpenetrated to 2-fold interpenetrated[65] and from 2 to 3-fold[66,67] which compensates for the loss of guest by reducing the available free volume. The resultant structure is of lower energy than an open form would be.

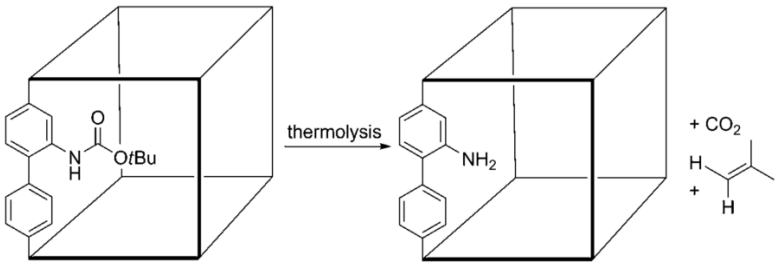

Figure 10 Thermolysis of NHBOC, the bulky substituent used to prevent interpenetration. Figure reproduced from Deshpande *et al.*[64]

1.5.2 Solvent exchange

MOFs are very often porous and capable of exchanging one solvent guest for another by simple immersion in the new solvent. Indeed guest replacement can also be achieved by activation followed by the introduction of a new guest by liquid diffusion or vapour/gas sorption but by 'solvent exchange' we refer to direct solvent guest replacement *without* proceeding via an empty or activated phase. MOF activation is the process of removing trapped guests. It can be achieved by various methods but the most common is heating under dynamic vacuum. In general, the as-synthesised material is immersed in the desired solvent, which diffuses into the pores of the material, dissolving or simply displacing the original guest solvent. The new solvent is usually replaced several times to ensure efficient exchange, so that there is effectively none of the original solvent guest remaining.

Rigid frameworks are easily able to undergo solvent exchange without appreciable loss of single-crystal character. Some of the earliest experiments with solvent exchange in MOFs are those carried out with $Ag(TEB)CF_3SO_3$ (TEB = tris(4-ethynylbenzonitrile)benzene) where various aromatic guests were exchanged without appreciable loss of framework integrity.[68,69] Solvent exchange in flexible frameworks also frequently proceeds via a single-crystal to single-crystal transformation.[70,71]

There has been some limited inquiry into the performance effects of solvent-mediated activation. However, detailed structural studies are limited. Yang and co-workers have shown that for the solvent-mediated activation of $Cu_3(BTC)_2$ (BTC = 1,3,5-

benzenetricarboxylate), the identity of the exchange solvent has a pronounced effect on sorption capacity, estimated pore size and estimated surface areas.[72]

1.5.3 Supercritical drying

Supercritical drying has been widely used in the preparation of aerogels[73,74,75] and has recently also found application in the activation of MOFs. Although in aerogel and other applications the supercritical fluid may vary, in MOF activation it is mainly CO_2 that is used. The method has been shown to improve MOF performance by preserving porosity.[76,77] Supercritical conditions for CO_2 are achieved at a temperature above 304 K when the pressure is higher than 73.8 bar (see Figure 11). In its supercritical fluid form CO_2 is able to dissolve and exchange with existing organic guest solvents in a MOF, and its gas-like properties allow it to be removed without the strong, destructive capillary forces that often lead to a loss of framework integrity.

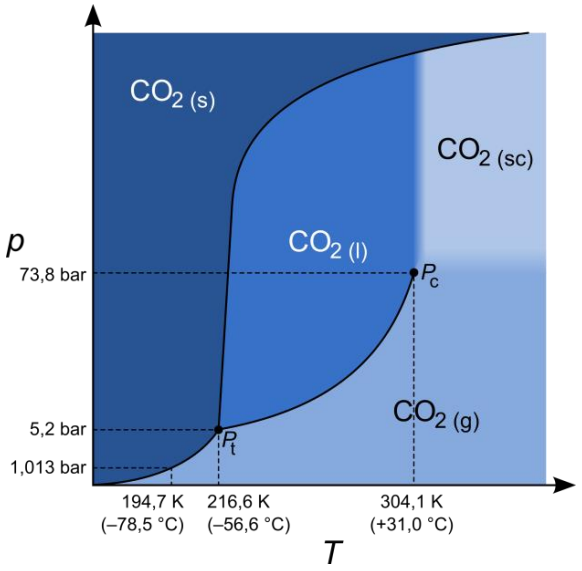

Figure 11. Schematic phase diagram for carbon dioxide. P_c and P_t are the critical point and triple point, respectively.[78]

1.5.4 Sorption

Adsorption either occurs via a chemical reaction and formation of covalent bonds between the sorbate and sorbent (chemisorption) or by some non-covalent interaction (physisorption). Idealised sorption-desorption isotherms Types I-VI are presented in Figure 12.[44] MOFs have a propensity for adsorption of various vapours and gases, and numerous examples of both chemisorption and physisorption have been reported for a wide variety of sorbates. Here we will deal with the capabilities of MOFs with respect to physisorption of gases. They have been identified as promising materials for gas storage and separation with such applications as hydrogen storage, CO_2 sequestration and the separation of flue gas emissions being investigated.[79,80]

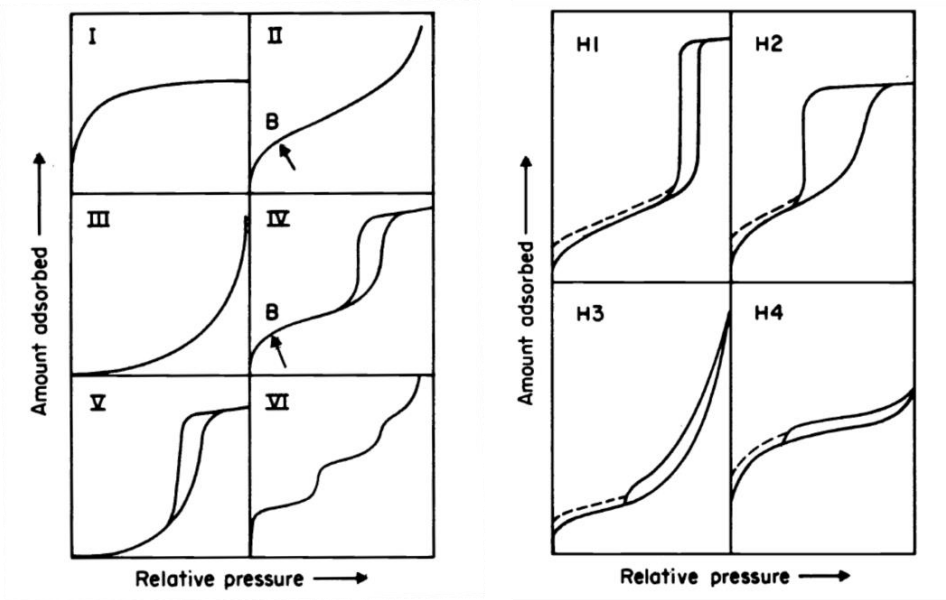

Figure 12. The set of curves on the left represent types of adsorption isotherms and those on the right represent idealised hysteresis loops. Figure reproduced from Sing *et. al.*[44]

The highest capacity sorption in MOFs has been recorded for rigid frameworks with very large voids. While MOF-5 showed high CO_2 sorption capacity of 21.7 mmol g^{-1} at high pressure, it was surpassed, in the same study, by MOF-177 which achieved 33.5 mmol g^{-1}.[81] Better still are the frameworks MOF-200 and MOF-210, which have tremendously large cavities. Both achieved CO_2 sorption of 2400 mg g^{-1} (54.5 mmol g^{-1}) at high pressure.[82]

Stepped or gated sorption in MOFs is usually associated with a host structural transformation.[55,83] At a critical pressure the gate-opening event occurs, where the rate of sorption increases rapidly as in the idealised curves for Types IV and VI.

The framework MOF-508 was first synthesised by Ma et *al.*[84] and separately by Chun et al.[85] Its sorption capabilities were demonstrated by Chen and co-workers who showed it adsorbed moderate amounts of gas at low temperature and pressure with an affinity for N_2 over CO_2 and H_2. Furthermore it was demonstrated that a GC column with MOF-508 stationary phase is able to resolve a mixture of linear and branched isomers of pentane and hexane.[86]

Remarkable selectivity has been achieved for several MOFs. Mg-MOF-74 demonstrated the potential utility of open metal sites for the separation of industrially relevant gas mixtures.[87] The preparation of MOFs with open metal sites had been demonstrated previously by others.[88,89] For Mg-MOF-74, selectivity for CO_2 over CH_4 was confirmed with breakthrough experiments. For a 20% mixture of CO_2 in CH_4 the material adsorbed virtually no CH_4 and 89 g of CO_2 per 100 g of sorbent under dynamic sorption conditions. CO_2 breakthrough occurred beyond 4 min of 25 ml min^{-1} flow.

For low pressure sorption at 298 K Wu and co-workers achieved remarkably high selectivity for CO_2 over several other gases (N_2 H_2, O_2, CO and CH_4) at 25 °C using a twofold interpenetrated mixed-ligand Zn MOF.[90]

Hysteresis is the phenomenon where a desorption isotherm does not retrace its corresponding adsorption isotherm. The graphs labelled H1-4 in Figure 12 represent the IUPAC categories of hysteresis loops.

Our group recently published an observation of extreme hysteresis for CO_2 trapped during attempted supercritical drying of a series of mixed ligand MOFs, each comprised of Cu(II), glutarate, and a bis-pyridyl linker.[91] The MOFs also adsorbed CO_2 gas with appreciable hysteresis (Figure 13, left). Other examples of exceptionally large hysteresis include MIL-53(Cr),[92] COMOC-2[93] and LaBTB[94] (Figure 13. Examples of experimental hysteretic CO2 sorption for a series of Cu glutarate MOFs (left) and LaBTB (right). Figures are reproduced from Bezuidenhout *et al.*[91] and, right).

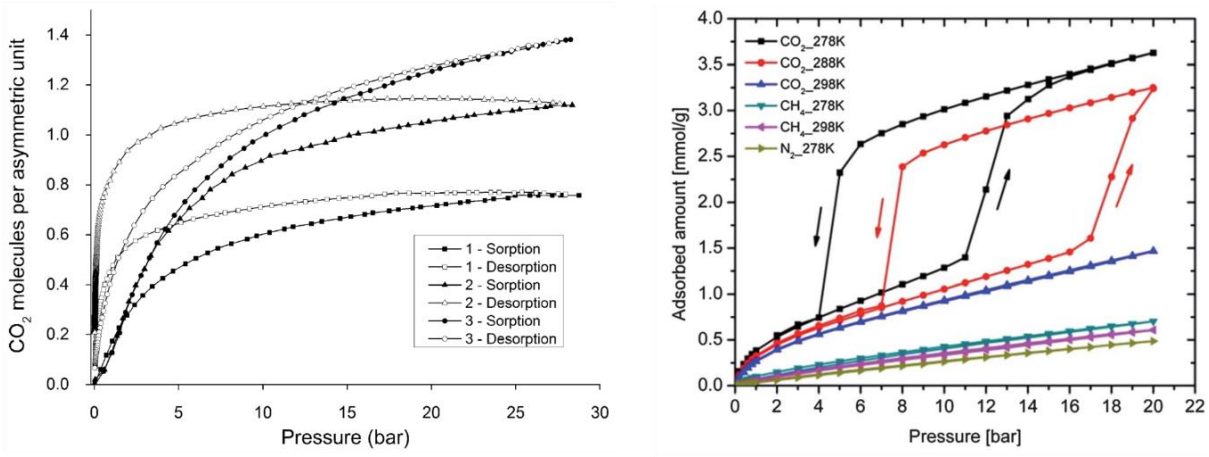

Figure 13. Examples of experimental hysteretic CO_2 sorption for a series of Cu glutarate MOFs (left) and LaBTB (right). Figures are reproduced from Bezuidenhout *et al.*[91] and Mu *et al.*[94]

1.5.5 Flexible MOFs

Recently there has been growing interest in 'soft porous crystals' or flexible MOFs, characterised by a propensity to respond dynamically to stimuli such as changes in temperature, pressure, electromagnetic radiation and atmospheric vapour or gas. In extreme cases metal-ligand coordination bonds break, form and rearrange.

Horike and co-workers described soft porous crystals in a seminal article.[95] In their introduction to the topic, the authors refer to an earlier classification of porous coordination polymers as either 1st, 2nd or 3rd generation based on the framework response to guest removal (see Figure 14).[96] The 1st generation compounds collapse and lose all structural integrity when the guest is removed. The 2nd generation materials are permanently porous

and usually rigid frameworks. The 3rd generation compounds are soft porous crystals that undergo some type of transformation where the host framework remains intact but changes form upon guest removal.

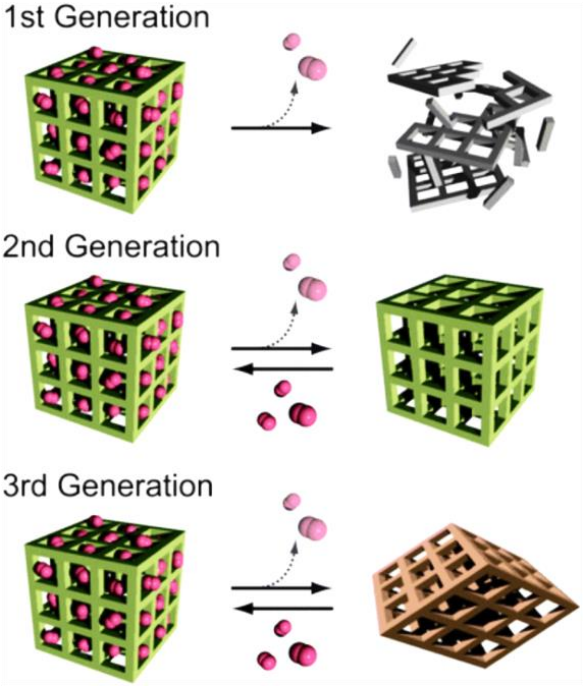

Figure 14. Classification of soft porous crystals as 1st, 2nd and 3rd generation. Figure reproduced from work by Shimomura and Kitagawa.[97]

Various flexible frameworks have been observed to adjust their pore size during guest uptake and removal. The cuprous triazolate framework MAF-2 expands and adjusts to accommodate hydrogen-bonded hexamers of methanol, ethanol and acetonitrile.[98] Similarly $[Cu_2(pzdc)_2(bpy)\cdot G]_n$ (pzdc = pyrazine-2,3-dicarboxylate, bpy = 4,4′-bipyridine, G = guest) displays 'shape-responsive fitting', defined as a combination of shrinkage and expansion of host pores to accommodate new guest molecules. The guest G could be introduced by exposing the apohost framework to vapours of H_2O or benzene. The adsorption of benzene triggered shape-responsive fitting.[99]

The phenomenon of breathing in MOFs is a special case of a reversible structural response to guest inclusion (see Figure 15). In 2004 Kitagawa *et al.* referred to breathing in MOFs in terms of "the slip and glide motion of independent networks".[43] More recently Schneemann *et al.* provided the following as a very suitable description: "As breathing we want to entitle (reversible) transitions of metal–organic frameworks, during which the (substantial) displacement of atoms of the framework is accompanied by a change in unit cell volume ($\Delta V \neq 0$). Characteristic distances and angles of the unit cell change and the crystallographic space groups of the two distinct phases (narrow pore and large pore) may be different."[100]

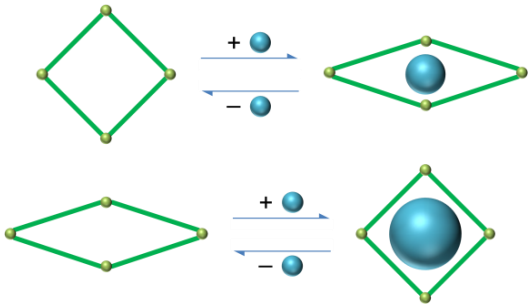

Figure 15. Two different types of framework breathing where guest uptake either causes shrinkage of the unit cell (top) or expansion of the unit cell (bottom). Figure adapted from Schneemann *et al.*[100]

The frameworks of the MIL-53 series have been studied extensively for their characteristic breathing behaviour. MIL-53(Cr)[101] is the first and best known member of the series and happens to also be the first reported three-dimensional MOF with a Cr(III)-carboxylate SBU. Analogues of the form MIL-53(M) are known for M = Al,[102] Ga,[102] In,[103] Fe[104] and Sc.[105] The pores of as-synthesised MIL-53(Cr) are large when the material is guest-free and they contract substantially when water is adsorbed into the pores. The hydrated form of MIL-53(Cr) has a high affinity for CO_2 over CH_4 while its dehydrated counterpart adsorbs CO_2 but also shows appreciable CH_4 sorption.[92] Sorption of CO_2 by the dehydrated version proceeds via two steps. At first the framework shrinks from a moderate to narrow pore size because of stabilising host-guest interactions. At approximately 5 bar of CO_2 pressure (304 K) a gate-opening step occurs and the framework expands to yield a very large pore size. Theoretical studies have probed the origins of the unique breathing behaviour of MIL-53(Cr).[106,107] The main contributors to the mechanism are guest-guest interactions and interactions between the guest molecules and hydroxyl groups of the host's inorganic nodes.

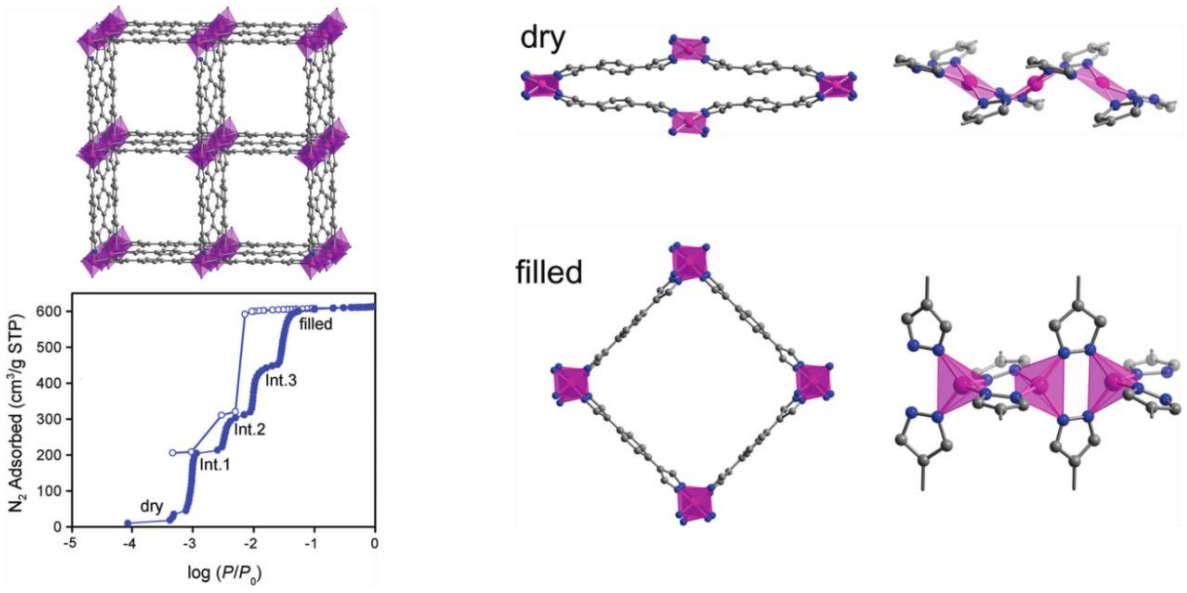

Figure 16. Multistep N_2 sorption in Co(1,4-benzenedipyrazolate) by a breathing mechanism. Figure reproduced from Salles *et al.*[108]

Salles and co-workers reported unprecedented four-step breathing for a MOF comprised of Co(II) metal centres and 1,4-benzenedipyrazolate as linker (see Figure 16).[108] The framework absorbs N_2 in four steps with incremental opening of the pore window. The first four phases involve weak interaction of N_2 with the open coordination sites of Co(II). The final sorption step involves a transformation of the Co(II) coordination geometry from square planar to tetrahedral.

1.6 Thermal expansion

Upon heating, most materials expand by relatively small and similar proportions in all three spatial dimensions. Some materials, however, expand anisotropically, and sometimes with large differences in the magnitudes of expansion along each dimension. In some cases thermal expansion is even negative, where the material contracts with increasing temperature. In recent years, materials exhibiting anomalous thermal expansion behaviour have emerged at an increasing rate. The number of publications mentioning “anomalous thermal expansion”, “anisotropic thermal expansion” and “negative thermal expansion” are shown as a histogram in Figure 17.

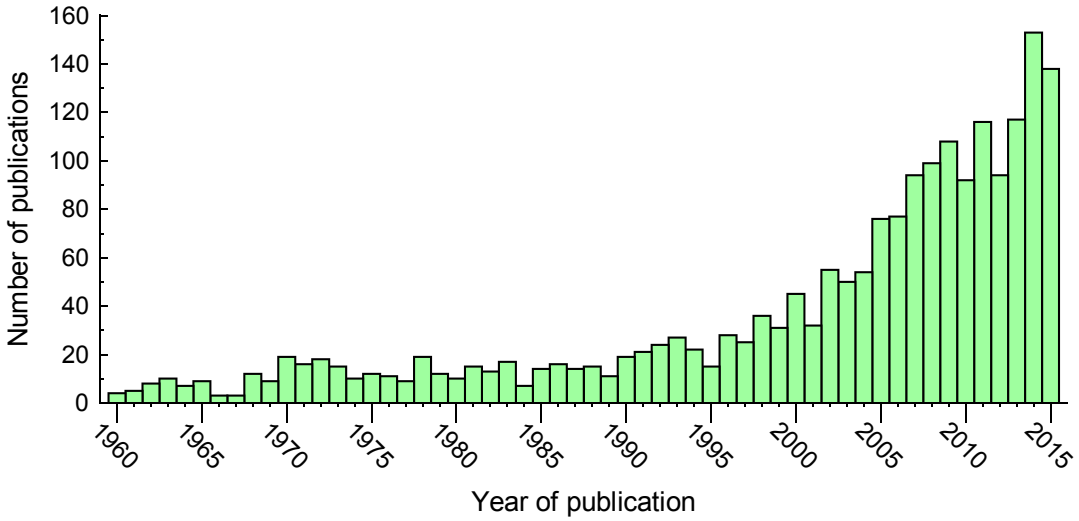

Figure 17. Number of publications per year mentioning “anomalous thermal expansion”, “anisotropic thermal expansion” or “negative thermal expansion”.

For crystals, linear coefficients of thermal expansion are usually based on linear regression analysis of changes in unit cell parameters with temperature. The linear coefficient of thermal expansion α_L is a measure of expansion along one of three orthogonal dimensions. L_T is the axis length at the final temperature T and L_0 the axis length at the initial temperature T_0. Similarly, α_V is the coefficient of volumetric thermal expansion:

$$\alpha_L = \frac{L_T - L_0}{L_0(T - T_0)} \qquad \alpha_V = \frac{V_T - V_0}{V_0(T - T_0)}$$

In crystals with orthogonal unit cells (orthorhombic and higher symmetry), the linear coefficients of thermal expansion are calculated along the crystallographic axes. Where the unit cell has non-orthogonal axes it is necessary to determine a set of orthogonal *principal axes*. Programmes such as PASCal[109] and Winstrain[110] are commonly used for this purpose.

Thermal expansion occurs gradually by definition and any sharp changes in unit cell dimensions are usually indicative of a phase transformation. It has generally held that thermal expansion occurs in the *absence* of phase transformations and should be reported accordingly, which is why thermal expansion studies are normally supported by DSC data.

Positive thermal expansion (PTE) of $\alpha_L < 20 \times 10^{-6}\,K^{-1}$ is considered unremarkable.[111] Large PTE, large negative thermal expansion (NTE) and large anisotropic thermal expansion occur more rarely and are considered anomalous. Goodwin *et al.* proposed 'colossal thermal expansion' to distinguish linear coefficients of $100 \times 10^{-6}K^{-1}$ or more but the term is not applied consistently.[112]

1.6.1 Inorganic crystals

Anomalous thermal expansion is widespread in inorganic materials and the first cases of volumetric NTE were reported for inorganic crystals. For many of these, the origin of NTE is rigid unit mode vibrations.[113,114]

The low temperature metastable form of ZrW_2O_8 is a well-known example that shows isotropic NTE of $\alpha_a = -9.1 \times 10^{-6}\,K^{-1}$.[115,116] At room temperature the cubic compound ScF_3 has $\alpha_a \approx -8 \times 10^{-6}\,K^{-1}$ but at lower temperature (60-110 K) α_a becomes $-14 \times 10^{-6}\,K^{-1}$.[117]

Volumetric NTE has been described for coordination complexes based on Prussian blue.[118] Analogues were prepared with formula $M^{II}Pt^{IV}(CN)_6$ where M^{II} = Mn, Fe, Co, Ni, Cu, Zn, Cd. The coefficient of thermal expansion could be tuned by replacement of M^{II} along a gradient from $-10.02 \times 10^{-6}\,K^{-1}$ for Ni to $-1.02 \times 10^{-6}\,K^{-1}$ for Cd.

Predictions of relatively large NTE in IRMOFs[119] were followed by experimental testing by others. MOF-5 was shown by Zhou and Wu to have linear components of $-16 \times 10^{-6}\,K^{-1}$ in the range 4-600 K, a value considered very large for isotropic NTE.[120] A more detailed structural study of MOF-5 was carried out by Lock and co-workers. They determined $\alpha_a = -13 \times 10^{-6}\,K^{-1}$ and confirmed a mechanism combining vibrations of the flexible linkers with rigidity of the inorganic nodes.[121]

The compound $Ag_3[Co(CN)_6]$, crystallising in the tetragonal crystal system, represented a remarkably unique discovery in thermal expansion with very large positive and negative area

thermal expansion in one crystal: $130 \times 10^{-6} K^{-1} < \alpha_a < 150 \times 10^{-6} K^{-1}$ and $-120 \times 10^{-6} K^{-1} > \alpha_c > -130 \times 10^{-6} K^{-1}$ over the temperature range.[112]

Our research group published an example of tunable anisotropic thermal expansion with a three-dimensional Zn MOF by variation of short-chain alcohol guest molecules. The mechanism involves stretching of a coordination helix of Zn–O(H)–Zn bonds.[122,123] Another result from our group identified a combined stretching and tilting mechanism as the driver of anomalous thermal expansion in a mixed-ligand Cd(II) MOF.[124]

The discrete complex $[FeL_3][BF_4]_2 \cdot xH_2O$ (L = 3-(pyrazinyl)-1*H*-pyrazole) exhibits NTE at low temperature and PTE at elevated temperatures. This switch is driven by a rearrangement of guest molecules upon cooling or heating beyond 240 K. Importantly, this example demonstrates that coordination bonds are not essential for driving NTE in inorganic materials.[125]

1.6.2 Organic crystals

Very large anisotropic thermal expansion, including biaxial NTE was recorded by our group for (*S,S*)-octa-3,5-diyn-2,7-diol (see Figure 18).[126] Over the temperature range 225-330 K the thermal expansion coefficients are in the range $156 \times 10^{-6} K^{-1} < \alpha_a < 515 \times 10^{-6} K^{-1}$; $-32 \times 10^{-6} K^{-1} < \alpha_b < -85 \times 10^{-6} K^{-1}$ and $-48 \times 10^{-6} K^{-1} < \alpha_c < -204 \times 10^{-6} K^{-1}$. The molecules form hydrogen bonded chains that give rise to negative thermal expansion via a mechanism that resembles a folding trellis, similar to the example of $Ag_3[Co(CN)_6]$ mentioned earlier.[112]

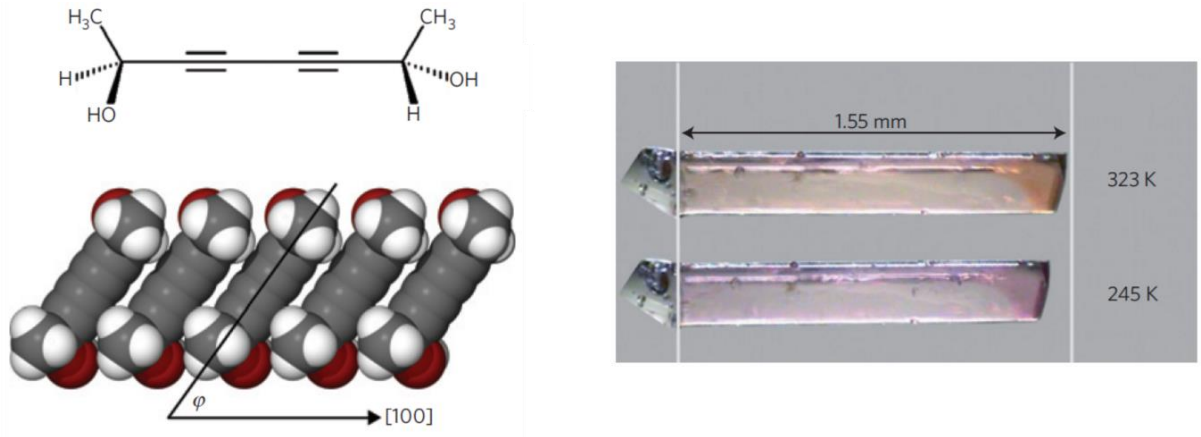

Figure 18. Structural formula and crystal packing of (*S,S*)-octa-3,5-diyn-2,7-diol (left) and remarkable contraction of a crystal of the compound upon cooling from 323 to 245 K (right). Figure reproduced from Das *et al.*[126]

Two of the first reported discoveries of NTE (both uniaxial NTE) in organic crystals were for suberic acid and tryptophylglycine monohydrate ($TrpGly \cdot H_2O$). Although the original paper describing suberic acid structures by neutron diffraction at three different temperatures was

focused on analysing the thermal vibrations of the molecule, the *b* axis, which for monoclinic systems such as this is always collinear with a principal axis, shrinks from 5.0885(7) to 5.0721(9) Å.[127] Temperature resolved unit cell data for TrpGly·H_2O were fitted to a higher order equation. For this tetragonal crystal the *c* axis shrinks while the *a* axis expands with increasing temperature.[128]

Bhattacharya and Saha described a multicomponent organic crystal where uniaxial NTE of $-27 \times 10^{-6} K^{-1}$ occurs by the sliding of hydrogen-bonded layers.[129] They suggest that in some cases the driving force is not easily identified and that it is difficult to determine whether it is "the directionality of some hydrogen bonds" or "the anisotropic vibration of the guest molecules in the channel".

McGillivray and co-workers recently published an important result where thermal expansion was tuned from colossal to zero in a two-component co-crystal with 4-phenylazopyridine where the other component, a dihalogenated benzene, was varied systematically.[130]

Although it is clear that particular patterns of hydrogen-bonded organic molecules can produce NTE, recent examples of NTE have been described where only weaker electrostatic interactions are present. For 4,4′-methylenebis(2,6-dimethylaniline) (MBDA) Bhattacharya and Saha studied triclinic and monoclinic forms where anomalous thermal expansion occurred in the absence of strong hydrogen bonds and was driven by the steric effects of methyl vibrations.[131] The monoclinic form showed large uniaxial NTE ($-174 \times 10^{-6} K^{-1}$) and large biaxial PTE ($174 \times 10^{-6} K^{-1}$ and $229 \times 10^{-6} K^{-1}$), while the triclinic form exhibited moderate PTE along all three axes.

Crystals of halogen-bonded complexes were studied by Jones *et al.*[132] The coefficients obtained for pyridine–IBr were: $\alpha_{X1} = 176$, $\alpha_{X2} = -38$, $\alpha_{X3} = 88$ and $\alpha_v = 226 \times 10^{-6} K^{-1}$. The researchers attributed these large thermal expansion values to the weakening of already weak CH···X interactions with increasing temperature.

1.7 Thermosalient effect

The thermosalient effect is the self-actuation of crystals upon heating or cooling. Typically a thermosalient crystal will undergo a sharp phase transition when heated or cooled beyond some critical temperature, appearing to jump or hop to a distance that is several times the length of the crystal.[133] This remarkable mechanical response sometimes manifests not as jumping but as an explosion, swift rotation or rapid expansion of the crystal.[134]

Crystallographically, the phase transition is usually accompanied by a large anisotropic change in unit cell dimensions. Thermal stage microscopy is the most appropriate technique for observing thermosalient behaviour directly but differential scanning calorimetry (DSC) is

also useful for detecting the phenomenon. Thermosalient phase transitions usually appear in DSC traces as jagged, sawtooth-like peaks (Figure 19).

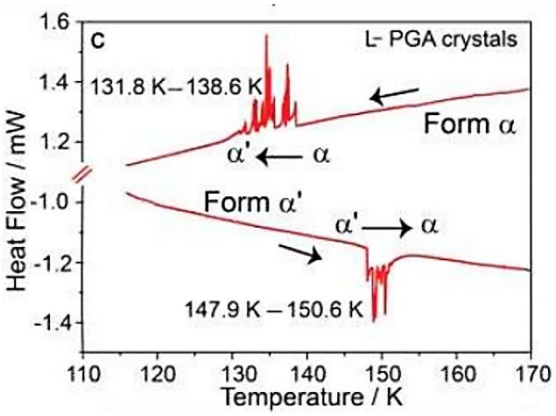

Figure 19. DSC trace for L-pyroglutamic acid showing typical sawtooth-like peaks that are indicative of thermosalient phase transitions. Figure reproduced from Panda *et al.*[135]

1.8 Aims

The overall aim of the present PhD project was to investigate the influence of guests on the dynamic solid-state properties of selected inclusion compounds. The specific areas of focus were anomalous thermal expansion in organic inclusion compounds and porosity – demonstrated by gas sorption – in a flexible MOF.

For the organic inclusion compounds we sought to understand the underlying mechanism of uniaxial negative thermal expansion in a complex where this phenomenon had been previously overlooked. The initial investigation was broadened to an isoskeletal series by incorporating two analogues of the original solvate. A general mechanism was pursued to explain the pattern of thermal expansion behaviour observed across the series.

For the MOF study, guest effects were investigated in two ways. Firstly, we experimented with activation by replacement of the original included guest with volatile solvents and supercritical CO_2. Secondly, different test gases were used as potential new guests to probe the porosity of a particular activated phase.

1.9 Thesis outline

The body of this thesis is divided according to publications in print or under review. Chapters 3 and 4 are related, focussing on anomalous thermal expansion in 18-crown-6 inclusion compounds, while Chapter 5 investigates activation-dependent structural changes and sorption behaviour of a novel flexible MOF.

Chapter 2 is an account of the experimental techniques that have been employed over the course of this research, including details of all instruments and computational tools.

Chapter 3 focuses on the thermal expansion of an 18-crown-6 solvate with nitromethane as guest. This example is notable because large uniaxial negative thermal expansion and exceptionally large volumetric thermal expansion are observed, unusually, in the absence of strong directional intermolecular interactions.

Chapter 4 extends the study described in Chapter 3 by expanding to a series of isoskeletal inclusion compounds based on the original solvate. Variation of the guest is shown to yield notable changes in anisotropic thermal expansion behaviour. A general mechanism for the series is proposed that accounts for the observed variations in thermal expansion. In addition, the first observation of thermosalient behaviour for an inclusion compound is reported.

Chapter 5 is a description of a novel non-interpenetrated, flexible, paddle-wheel type MOF. Activation by direct thermal evacuation, via supercritical CO_2 drying, and by evacuation via solvent exchange yielded different phases. The collapsed activated phase from solvent exchange exhibits gated breathing with extremely broad hysteresis and selectivity for CO_2 over N_2 and CH_4. The systematic loss of sorption capacity with repeated sorption/desorption cycling was analysed.

Chapter 6 provides a summary and concluding remarks.

1.10 References

1 Pederson, C. J. *J. Am. Chem. Soc.* **1967**, *89*, 7017.

2 Pedersen, C. J. *Angew. Chem. Int. Ed.* **1988**, *27*, 1021.

3 Dietrich, B.; Lehn, J.-M.; Sauvage, J.-P. *Tetrahedron Lett.* **1969**, *10*, 2885.

4 Dietrich, B.; Lehn, J.-M.; Sauvage, J.-P. *Tetrahedron Lett.* **1969**, *10*, 2889.

5 Trueblood, K. N.; Knobler, C. B.; Maverick, E.; Helgeson, R. C.; Brown, S. B.; Cram, D. J. *J. Am. Chem. Soc*. **1981**, *103*, 5594.

6 Cram, D. J. *Angew. Chem. Int. Ed.* **1988**, *27*, 1009.

7 Lehn, J. M. Cryptates: Inclusion Complexes of Macropolycyclic Receptor Molecules. *Pure Appl. Chem.* **1978**, *50*, 871.

8 Lehn, J.-M. *Angew. Chem. Int. Ed.* **1988**, *27*, 89.

9 Gavezzotti, A. *CrystEngComm* **2013**, *15*, 4027.

10 Pauling, L. J. Am. Chem. Soc. 1935, 57, 2680.

11 Pauling, L. *The Nature of the Chemical Bond*; Cornell University Press: Ithaca, NY, U.S.A. 1939.

12 Arunan, E.; Desiraju, G. R.; Klein, R. A.; Sadlej, J.; Scheiner, S.; Alkorta, I.; Clary, D. C.; Crabtree, R. H.; Dannenberg, J. J.; Hobza, P.; Kjaergaard, H. G.; Legon, A. C.; Mennucci, B.; Nesbitt, D. J. *Pure Appl. Chem.* **2011**, *83*, 1637.

13 Desiraju, G. R. *Angew. Chem. Int. Ed.* **1995**, *34*, 2311.

14 Desiraju, G. R. *J. Am. Chem. Soc.* **2013**, *135*, 9952.

15 Dunitz, J. D.; Gavezzotti, A. *Cryst. Growth Des.* **2012**, *12*, 5873.

16 Woinska, M.; Grabowsky, S.; Dominiak, P. M.; Wozniak, K.; Jayatilaka, D. *Sci. Adv.* **2016**, *2*, DOI: 10.1126/sciadv.1600192

17 Nimmermark, A.; Öhrström, L.; Reedijk, J. *Z. Kristallogr.* **2013**, *288*, 311.

18 Yaghi, O. M.; O'Keeffe, M.; Ockwig, N. W.; Chae, H. K.; Eddaoudi, M.; Kim, J. *Nature* **2003**, *423*, 705.

19 London, F. *Trans. Faraday Soc.*, **1937**, *33*, 8.

20 Stone, A. J. *The Theory of Intermolecular Forces*; Clarendon Press: Oxford, U.K., 1996.

21 Matthews, R. P.; Welton, T.; Hunt, P. A. *Phys. Chem. Chem. Phys.* **2014**, *16*, 3238.

22 Kyba, E. P.; Helgeson, R. C.; Madan, K.; Gokel, G. W.; Tarnowski, T. L.; Moore, S. S.; Cram, D. J. *J. Am. Chem. Soc.* **1977**, *99*, 2564.

23 IUPAC; *Compendium of Chemical Terminology*, 2nd ed.; McNaught, A. D., Wilkinson, A., Eds.; Blackwell Scientific Publications: Oxford, U.K., 1997.

24 Danylyuk, O.; Suwinska, K. *Chem. Commun.* **2009**, 5799.

25 Chapin, J. C.; Kvasnica, M.; Purse, B. W. *J. Am. Chem. Soc.* **2012**, *134*, 15000.

26 Du Plessis, M.; Smith, V. J.; Barbour, L. J. *CrystEngComm* **2014**, *16*, 4126.

27 IUCr. Online Dictionary of Crystallography. http://reference.iucr.org/dictionary/Isostructural_crystals (accessed August 15, 2016).

28 Barbour, L. J.; Das, D.; Jacobs, T.; Lloyd, G. O.; Smith, V. J. Concepts and Nomenclature in Chemical Crystallography. In *Supramolecular Chemistry: From Molecules to Nanomaterials*; Gale, P. A., Steed, J. W., Eds.;John Wiley & Sons: West Sussex, U.K, 2012.

29 Caira, M. R. *Rev. Roum. Chim.* **2001**, *46*, 371.

30 Lloyd, G. O.; Alen, J.; Bredenkamp, M. W.; de Vries, E. J. C.; Esterhuysen, C.; Barbour, L. J. *Angew. Chem. Int. Ed.* **2006**, *45*, 5354.

31 IUCr. Online Dictionary of Crystallography. http://reference.iucr.org/dictionary/Isomorphous_crystals (accessed August 15, 2016).

32 Gokel, G. W.; Cram, D. J.; Liotta, C. L.; Harris, H. P.; Cook, F.L. *J. Org. Chem.* **1974**, *39*, 2445.

33 Harkema, S.; Van Hummel, G. J.; Daasvatn, K.; Reinhoudt, D. N. *J. Chem. Soc., Chem. Commun.* **1981**, 368.

34 Watson, W.; Galloy, J.; Grossie, D.; Vögtle, F.; Müller, W. M. *J. Org. Chem.* **1984**, *49*, 347.

35 Müller, A.; Reuter, H.; Dillinger, S. *Angew. Chem. Int. Ed.* **1995**, *34*, 2328.

36 Breck, D. W. *Zeolite Molecular Sieves: Structure, Chemistry, and Use*; Wiley: New York, 1974.

37 *Zeolites in Industrial Separation and Catalysis*; Kulprathipanja, S., Ed.; Wiley-VCH: Weinheim, Germany, 2010.

38 Erdem, E.; Karapinar, N.; Donat, R. *J. Colloid Interface Sci.* **2004**, *280*, 309.

39 Day, V. W.; Klemperer, W. G.; Yaghi, O. M. *J. Am. Chem. Soc.* **1989**, *111*, 5959.

40 Jacobs, T.; Lloyd, G. O.; Gertenbach, J.-A.; Müller-Nedebock, K. K.; Esterhuysen, C.; Barbour, L. J. *Angew. Chem. Int. Ed.* **2012**, *124*, 4997.

41 Du Plessis, M.; Smith, V. J.; Barbour, L. J. *CrystEngComm* **2014**, *16*, 4126.

42 Batten, S. R.; Champness, N. R.; Chen, X.; Garcia-Martinez, J.; Kitagawa, S.; Öhrström, L.; Keeffe, M. O.; Suh, M. P.; Reedijk, J. *Pure Appl. Chem.* **2013**, *85*, 1715.

43 Kitagawa, S.; Kitaura, R.; Noro, S.-I. *Angew. Chem. Int. Ed.* **2004**, *43*, 2334.

44 Sing, K. S. W.; Everett, D. H.; Haul, R. A. W.; Moscou, L.; Pierotti, R. A.; Rouquérol, J.; Simieniewska, T. *Pure Appl. Chem.* **1985**, *57*, 603.

45 Nassimbeni, L. R. *Acc. Chem. Res.* **2003**, *36*, 631.

46 Barbour, L. J. *Chem. Commun.* **2006**, 1163.

47 Hofmann, K. A.; Küspert, F. A. *Z. Anorg. Chem.* **1897**, *15*, 204.

48 Rayner, J. H.; Powell, H. M. *J. Chem. Soc.* **1952**, 319.

49 Fujita, M. From Hofmann Complexes to Organic Coordination Networks. In *Metal-Organic Frameworks: Design and Application*; MacGillivray, L. R., Ed.; John Wiley & Sons: Hoboken, NJ, U.S.A., 2010.

50 Hoskins, B.; Robson, R. *J. Am. Chem. Soc.* **1989**, *111*, 5962.

51 Tranchemontagne, D. J.; Mendoza-Cortés, J. L.; O'Keeffe, M.; Yaghi, O. M. *Chem. Soc. Rev.* **2009**, *38*, 1257.

52 Eddaoudi, M.; Moler, D. B.; Li, H.; Chen, B.; Reineke, T. M.; O'Keeffe, M.; Yaghi, O. M. *Acc. Chem. Res.* **2001**, *34*, 319.

53 Hosseini, M. W. *Acc. Chem. Res.* **2005**, *38*, 313.

54 Moulton, B.; Zaworotko, M. J. *Chem. Rev.* **2001**, *101*, 1629.

55 Seo, J.; Bonneau, C.; Matsuda, R.; Takata, M.; Kitagawa, S. *J. Am. Chem. Soc.* **2011**, *133*, 9005.

56 Rowsell, J. L. C.; Yaghi, O. M. *Microporous Mesoporous Mater.* **2004**, *73*, 3.

57 Li, H.; Eddaoudi, M.; O'Keeffe, M.; Yaghi, O. M. *Nature* **1999**, *402*, 276.

58 Eddaoudi, M.; Kim, J.; Rosi, N.; Vodak, D.; Wachter, J.; O'Keeffe, M.; Yaghi, O. M. *Science* **2002**, *295*, 469.

59 Ma, B. Q.; Mulfort, K. L.; Hupp, J. T. *Inorg. Chem.* **2005**, *44*, 4912.

60 Eddaoudi, M.; Kim, J.; Rosi, N.; Vodak, D.; Wachter, J.; O'Keeffe, M.; Yaghi, O. M. *Science* **2002**, *295*, 469.

61 Zhang, J.; Wojtas, L.; Larsen, R. W.; Eddaoudi, M.; Zaworotko, M. J. *J. Am. Chem. Soc.* **2009**, *131*, 17040.

62 Jiang, H. L.; Tatsu, Y.; Lu, Z. H.; Xu, Q. *J. Am. Chem. Soc.* **2010**, *132*, 5586.

63 Rankine, D.; Avellaneda, A.; Hill, M. R.; Doonan, C. J.; Sumby, C. J. *Chem. Commun.* **2012**, *48*, 10328.

64 Deshpande, R. K.; Minnaar, J. L.; Telfer, S. G. *Angew. Chem. Int. Ed.* **2010**, *49*, 4598.

65 Aggarwal, H.; Lama, P.; Barbour, L. J. *Chem. Commun.* **2014**, *50*, 14543.

66 Aggarwal, H.; Bhatt, P. M.; Bezuidenhout, C. X.; Barbour, L. J. *J. Am. Chem. Soc.* **2014**, 17.

67 Aggarwal, H.; Das, R. K.; Bhatt, P. M.; Barbour, L. J. *Chem. Sci.*, **2015**, *6*, 4986.

68 Gardner, G.B.; Venkataraman, D.; Moore, J.S.; Lee, S. *Nature* **1995**, *374*, 792.

69 Gardner, G.B.; Kiang, Y.-H.; Lee, S.; Asgaonkar, A.; Venkataraman, D. *J. Am. Chem. Soc.* **1996**, 118, 6946.

70 Zeng, M.-H.; Tan, Y.-X.; He, Y.-P.; Yin, Z.; Chen, Q.; Kurmoo, M. A. *Inorg. Chem.* **2013**, *52*, 2353.

71 Medishetty, R.; Jung, D.; Song, X.; Kim, D.; Lee, S. S.; Lah, M. S.; Vittal, J. J. *Inorg. Chem.* **2013**, *52*, 2951.

72 Yang, Y.; Shukla, P.; Wang, S.; Rudolph, V.; Chen, X.-M.; Zhu, Z. *RSC Adv.* **2013**, *3*, 17065.

73 Tewari, P. H.; Hunt, A. J.; Lofftus, K. D. *Mater. Lett.* **1985**, *3*, 363.

74 Bedilo, A.F.; Klabunde, K.J.; *Nanostruct. Mater.***1997**, *8*, 119.

75 Suh, D. J.; Park, T.-J.; Han, H.-Y.; Lim, J.-C. *Chem. Mater.*, **2002**, *14*, 1452.

76 Nelson, A. P.; Farha, O. K.; Mulfort, K. L.; Hupp, J. T. *J. Am. Chem. Soc.* **2009**, *131*, 458.

77 Kim, T. K.; Suh, M. P. *Chem. Commun.* **2011**, *47*, 4258.

78 Wikimedia Commons. https://commons.wikimedia.org/wiki/File:Carbon_dioxide_p-T_phase_diagram.svg (accessed August 15, 2016).

79 Lee, J. Y.; Pan, L.; Kelly, S. P.; Jagiello, J.; Emge, T. J.; Li, J. *Adv. Mater.* **2005**, *17*, 2703.

80 Zhang, Z.; Zhao, Y.; Gong, Q.; Li, Z.; Li, J. *Chem. Commun.* **2013**, *49*, 653.

81 Millward A. R.; Yaghi, O. M. *J. Am. Chem. Soc.* **2005**, *127*, 17998

82 Furukawa, H.; Ko, N.; Go, Y. B.; Aratani, N.; Choi, S. B.; Choi, E.; Yazaydin, A. O.; Snurr, R. Q.; O'Keeffe, M.; Kim, J.; Yaghi, O. M. *Science* **2010**, *329*, 424.

83 Cheng, Y.; Kajiro, H.; Noguchi, H.; Kondo, A.; Ohba, T.; Hattori, Y.; Kaneko, K.; Kanoh, H. *Langmuir* **2011**, 27, 6905.

84 Ma, B. Q.; Mulfort, K. L.; Hupp, J. T. *Inorg. Chem.* **2005**, *44*, 4912.

85 Chun, H.; Dybtsev, D. N.; Kim, H.; Kim, K. *Chem. Eur. J.* **2005**, *11*, 3521.

86 Chen, B.; Liang, C.; Yang, J.; Contreras, D. S.; Clancy, Y. L.; Lobkovsky, E. B.; Yaghi, O. M.; Dai, S. *Angew. Chem. Int. Ed.* **2006**, *45*, 1390.

87 Britt, D.; Furukawa, H.; Wang, B.; Glover, T. G.; Yaghi, O. M. *Proc. Natl. Acad. Sci. U.S.A.* **2009**, *106*, 20637.

88 Chuy, S. S.-Y.; Lo, S. M.-F.; Charmant, J. P. H.; Orpen, A. G.; Williams, I. D. *Science* **1999**, *283*:1148.

89 Chen, B.; Eddaoudi, M.; Reineke, T. M.; Kampf, J. W.; O'Keeffe, M.; Yaghi, O. M. *J. Am. Chem. Soc.* **2000**, *122*, 11559.

90 Wu, H.; Reali, R. S.; Smith, D. A; Trachtenberg, M. C.; Li, J. *Chem. Eur. J.* **2010**, *16*, 13951.

91 Bezuidenhout, C. X.; Smith, V. J.; Bhatt, P. M.; Esterhuysen, C.; Barbour, L. J. *Angew. Chem. Int. Ed.* **2015**, *54*, 2079.

92 Llewellyn, P. L.; Bourrelly, S.; Serre, C.; Filinchuk, Y.; Férey, G. *Angew. Chem. Int. Ed.* **2006**, *45*, 7751.

93 Liu, Y.; Couck, S.; Vandichel, M.; Grzywa, M.; Leus, K.; Biswas, S.; Volkmer, D.; Gascon, J.; Kapteijn, F.; Denayer, J. F. M.; Waroquier, M.; Van Speybroeck, V.; Van Der Voort, P. *Inorg. Chem.* **2013**, *52*, 113.

94 Mu, B.; Li, F.; Huang, Y.; Walton, K. S. *J. Mater. Chem.* **2012**, *22*, 10172.

95 Horike, S.; Shimomura, S.; Kitagawa, S. *Nat. Chem.* **2009**, *1*, 695.

96 Kitagawa, S.; Kondo, M. *Bull. Chem. Soc. Jpn.* **1998**, *71*, 1739.

97 Shimomura, S.; Kitagawa, S. *J. Mater. Chem.* **2011**, *21*, 5537.

98 Zhang, J. P.; Chen, X. M. *J. Am. Chem. Soc.* **2008**, *130*, 6010.

99 Matsuda, R.; Kitaura, R.; Kitagawa, S.; Kubota, Y.; Kobayashi, T. C.; Horike, S.; Takata, M. *J. Am. Chem. Soc.* **2004**, *126*, 14063.

100 Schneemann, A.; Bon, V.; Schwedler, I.; Senkovska, I.; Kaskel, S.; Fischer, R. A. *Chem. Soc. Rev.* **2014**, *43*, 6062.

101 Serre, C.; Millange, F.; Thouvenot, C.; Noguès, M.; Marsolier, G.; Louër, D.; Férey, G. *J. Am. Chem. Soc.* **2002**, *124*, 13519.

102 Volkringer, C.; Loiseau, T.; Guillou, N.; Ferey, G.; Elkaim, E.; Vimont, A. *Dalton Trans.* **2009**, 2241.

103 Anokhina, E. V.; Vougo-Zanda, M.; Wang, X.; Jacobson, A. J. *J. Am. Chem. Soc.* **2005**, 127, 15000.

104 F. Millange, N. Guillou, R. I. Walton, J.-M. Greneche, I. Margiolaki and G. Ferey, *Chem. Commun.*, **2008**, 4732.

105 Mowat, J. P. S.; Seymour, V. R.; Griffin, J. M.; Thompson, S.P.; Slawin, A. M. Z.; Fairen-Jimenez, D. Dueren, T.; Ashbrook, S. E.; Wright, P. A. *Dalton Trans.*, **2012**, *41*, 3937.

106 Salles, F.; Ghoufi, A.; Maurin, G.; Bell, R. G.; Mellot-Draznieks, C.; Férey, G. *Angew. Chem. Int. Ed.* **2008**, *47*, 8487.

107 Serre, C.; Bourrelly, S.; Vimont, A.; Ramsahye, N. A.; Maurin, G.; Llewellyn, P. L.; Daturi, M.; Filinchuk, Y.; Leynaud, O.; Barnes, P.; Férey, G. *Adv. Mater.* **2007**, *19*, 2246.

108 Salles, F.; Maurin, G.; Serre, C.; Llewellyn, P. L.; Knöfel, C.; Choi, H. J.; Filinchuk, Y.; Oliviero, L.; Vimont, A.; Long, J. R.; Férey, G. *J. Am. Chem. Soc.* **2010**, *132*, 13782.

109 Cliffe, M. J.; Goodwin, A. L. *J. Appl. Crystallogr.* **2012**, *45*, 1321.

110 Angel, R. J. *Win_Strain*, 2011, www.rossangel.com (accessed August 15, 2016).

111 Krishnan, R. S.; Srinivasan, R.; Devanarayanan, S. *Thermal Expansion of Crystals*; Pergamon Press: Oxford, England, 1979.

112 Goodwin, A. L.; Calleja, M.; Conterio, M. J.; Dove, M. T.; Evans, J. S. O.; Keen, D. A.; Peters, L.; Tucker, M. G. Colossal Positive and Negative Thermal Expansion in the Framework Material Ag3[Co(CN)6]. *Science* **2008**, *319* (5864), 794–797.

113 Barrera, G. D.; Bruno, J. A. O.; Barron, T. H. K.; Allan, N. L. *J. Phys. Condens. Matter* **2005**, *17*, R217.

114 Miller, W.; Smith, C. W.; Mackenzie, D. S.; Evans, K. E. Negative Thermal Expansion: A Review. *J. Mater. Sci.* **2009**, *44* (20), 5441–5451.

115 Mary, T. A.; Evans, J. S. O.; Vogt, T.; Sleight, A. W. *Science* **1994**, *272*, 90.

116 Evans, J. S. O.; David, W. I. F.; Sleight, A. W. *Acta Crystallogr.* **1999**, B*55*, 333.

117 Greve, B. K.; Martin, K. L.; Lee, P. L.; Chupas, P. J.; Chapman, K. W.; Wilkinson, A. P. *J. Am. Chem. Soc.* **2010**, *132*, 15496.

118 Chapman, K. W.; Chupas, P. J.; Kepert, C. J. *J. Am. Chem. Soc.* **2006**, *128*, 7009.

119 Dubbeldam, D.; Walton, K. S.; Ellis, D. E.; Snurr, R. Q. *Angew. Chem. Int. Ed.* **2007**, *46*, 4496.

120 Zhou, W.; Wu, H.; Yildirim, T.; Simpson, J.; Walker, A. *Phys. Rev. B* **2008**, *78*, 054114.

121 Lock, N.; Wu, Y.; Christensen, M.; Cameron, L. J.; Peterson, V. K.; Bridgeman, A. J.; Kepert, C. J.; Iversen, B. B. *J. Phys. Chem. C* **2010**, *114*, 16181.

122 Grobler, I.; Smith, V. J.; Bhatt, P. M.; Herbert, S. A; Barbour, L. J. *J. Am. Chem. Soc.* **2013**, *135*, 6411.

123 Van Heerden, D. P.; Esterhuysen, C.; Barbour, L. J. *Dalton Trans.* **2015**, 45, 4141.

124 Lama, P.; Das, R. K.; Smith, V. J.; Barbour, L. J. *Chem. Commun.* **2014**, *50*, 6464.

125 Loughrey, J. J.; Comyn, T. P.; Apperley, D. C.; Little, M. A.; Halcrow, M. A. *Chem. Commun.* **2014**, *50*, 7601.

126 Das, D.; Jacobs, T.; Barbour, L. J. *Nat. Mater.* **2010**, *9*, 36.

127 Gao, Q.; Weber, H.-P.; Craven, B. M.; McMullan, R. K. *Acta Crystallogr.* **1994**, B*50*, 703.

128 Birkedal, H.; Schwarzenbach, D.; Pattison, P. *Angew. Chem. Int. Ed.* **2002**, *41*, 754.

129 Bhattacharya, S.; Saha, B. K. *Cryst. Growth Des.* **2012**, *12*, 4716.

130 Hutchins, K. M.; Groeneman, R. H.; Reinheimer, E. W.; Swenson, D. C.; MacGillivray, L. R. *Chem. Sci.* **2015**, *6*, 4717.

131 Bhattacharya, S.; Saha, B. K. *CrystEngComm.* **2014**, *16*, 2340.

132 Jones, R. H.; Knight, K. S.; Marshall, W. G.; Clews, J.; Darton, R. J.; Pyatt, D.; Coles, S. J.; Horton, P. N. *CrystEngComm.* **2014**, *16*, 237.

133 Skoko, Ž.; Zamir, S.; Naumov, P.; Bernstein, *J. Am. Chem. Soc.* **2010**, *132*, 14191.

134 Sahoo, S. C.; Panda, M. K.; Nath, N. K. Naumov, P. *J. Am. Chem. Soc.* **2013**, *135*, 12241.

135 Panda, M. K.; Runcevski, T.; Husain, A.; Dinnebier, R. E.; Naumov, P. *J. Am. Chem. Soc.* **2015**, *137*, 1895.

Chapter 2
Experimental Techniques

2.1 Ligand synthesis

2,5-diphenylbenzene-1,4-dicarboxylic acid (see Chapter 5) was synthesised according to a literature procedure.[1] All other chemical reagents were obtained from commercial sources.

2.2 Solvothermal synthesis

The metal-organic framework (MOF) synthesis was carried out by solvothermal methods (see Chapter 5). MOF experiments that were conducted over the course of this research typically involved combining a metal salt with a dicarboxylic acid ligand and a dipyridyl ligand in a given stoichiometric ratio in pure solvent or a mixture of solvents. The reaction mixture is loaded into a scintillation vial or a steel autoclave. The vial or autoclave is then subjected to a controlled temperature programme in an oven.

2.3 Crystallisation by slow evaporation

Slow evaporation is a very common crystallisation technique. It is used to prepare molecular as well as multi-component crystals (see Chapters 3 and 4). Typically a concentrated solution of the desired compound or mixture of components is prepared. The solution is then filtered and allowed to evaporate slowly at room temperature. The rate of crystallisation can be controlled by modifying the concentration of the solution and well as the temperature at which the solution is stored.

2.4 Single-crystal X-ray diffraction

Intensity data were collected using two different diffractometers: a Bruker APEX-II DUO and a Bruker D8 Venture. The APEX-II DUO employs a multilayer monochromator with MoKα radiation (λ = 0.71073 Å) from an Incoatec IμS microfocus source and CCD area-detector. The diffractomer is equipped with an Oxford Cryosystems 700Plus cryostat supplied with liquid N_2. The D8 Venture with Photon II CPAD detector also employs a multilayer monochromator with MoKα radiation (λ = 0.71073 Å) from an Incoatec IμS microfocus source. It is equipped with an Oxford Cryostreams 800Plus cryostat supplied with liquid N_2.

Data reduction was carried out by means of the standard procedure using the Bruker software package SAINT[2] and the absorption corrections and the correction of other

systematic errors were performed using SADABS.[3] The structures were solved by direct methods using SHELXS-97 and refined using SHELXL-97.[4] X-Seed[5] was used as the graphical interface for the SHELX program suite. Hydrogen atoms were placed in calculated positions using riding models. PLATON SQUEEZE[6] was used to account for highly disordered molecules that could not be modelled and to calculate values of total residual electron density.

2.5 Powder X-ray diffraction

Routine powder X-ray diffraction (PXRD) data were collected using a Bruker D2 PHASER equipped with a Lynxeye 1D detector and Ni-filtered Cu K_α radiation (λ = 1.5418 Å; 30 kV, 10 mA generator parameters; restricted by a 1.0 mm divergence slit and a 2.5 Soller collimator).

Temperature-resolved and pressure-resolved PXRD experiments were carried out using Cu Kα radiation (λ = 1.5418 Å, 40 kV and 30 mA) on a PANalytical X'pert PRO instrument operating in Bragg-Brentano geometry. Samples were placed in sealed glass capillaries. Temperature control was enabled by a short-nozzle Oxford Cryostream 700Plus cryostat. For pressure-resolved experiments an environmental gas cell was used.

2.6 Environmental gas cell

An environmental gas cell system was developed by the research group of Prof L. J. Barbour for recording single-crystal and powder X-ray diffraction data for samples under controlled atmospheres. The technique is suitable for high vacuum experiments and uniquely capable of containing gas at pressures as high as 80 bar.

The gas cell system consists of two parts. The upper part is a stainless steel nut into which a glass capillary can be fitted and attached with epoxy resin. The base is a nickel-coated brass cell with a valve stem that allows for evacuation and gas loading. The cell is easily mounted on an X-ray diffractometer using a commercial goniometer head. A 0.3 mm capillary was used for single-crystal as well as PXRD experiments.

2.7 Thermogravimetric analysis

Thermogravimetric analysis (TGA) was carried out using a TA Instruments Q500 analyser. The instrument records weight loss as a function of temperature. It was used to determine onset temperatures and temperature ranges of guest loss and sample degradation. Typically a sample of 0.5-4 mg was heated from ambient temperature to 773 K in a standard TA Instruments aluminium pan at a ramp rate of 10 K min^{-1}. Samples were analysed under constant purge of dry nitrogen gas at a flow rate of 50 ml min^{-1}. TGA traces were analysed

and figures generated using Universal Analysis 2000 v 4.5A (TA Instruments). Additional figures were generated using Microsoft Excel 2010.

2.8 Differential scanning calorimetry

The two instruments used for differential scanning calorimetry (DSC) were a TA Instruments Q100 with Liquid Nitrogen Cooling Accessory (LNCS) and a TA Instruments Q20 with Refrigerated Cooling System (RCS90). The former has a minimum operating temperature of 93 K while the latter is limited to a minimum of 183 K. Both instruments measure heat flow to and from a sample pan, relative to a reference pan, as a function of temperature. DSC traces will display thermal events as endothermic and exothermic peaks. The pans are standard aluminium pans supplied by TA Instruments. Typically a sample of 0.5-4 mg was subjected to a temperature ramp rate of 10 K min^{-1}. Experiments were conducted under constant purge of dry nitrogen gas at a flow rate of 50 ml min^{-1}.

2.9 Supercritical drying

A Tousimis SAMDRI-PVT-3D advanced manual critical point drier was used for MOF activation by supercritical CO_2 exchange. A sample is usually loaded into a glass vial and placed in the sample chamber of the instrument. The chamber is then cooled by rapid expansion of the online liquid CO_2. Once the chamber temperature reaches ~263 K it is filled with liquid CO_2. The chamber is then sealed and heated to 306-312 K to bring it to supercritical conditions. The sample is stored under supercritical fluid CO_2 for several hours or days before slowly depressurising the chamber and removing the sample.

2.10 Gas sorption

A Setaram PCTPro-E&E gas analyser with MicroDoser attachment was employed for gas sorption experiments with test gases N_2, CH_4 and CO_2. The instrument is based on a volumetric method known as the Sievert's method. A sample at known pressure and volume is connected to a reservoir of known volume and pressure through an isolation valve. The valve is opened and the system allowed to equilibrate. The difference between the measured pressure and calculated pressure (assuming zero sorption) is used to determine the amount of gas adsorbed. The PCTPro-E&E has a broad operating pressure range of vacuum to 200 bar. Sample sizes of 40-80 mg were used and blank runs for each gas were used to correct for unavoidable systematic errors.

2.11 Pressure-resolved DSC

Pressure-resolved differential scanning calorimetry (pressure-DSC) was conducted using an instrumental setup designed in our laboratory. We combined a Setaram μDSC7 Evo module with a high pressure sample holder. For constant gradient pressure measurements the DSC is coupled to a Teledyne ISCO 260D syringe pump, controlled by software developed by L. J. Barbour. Where stepwise pressure increases are necessary, the DSC is coupled with the PCTPro-E&E gas analyser, which supplies the required pressure doses in a stepwise manner. Data were collected and analysed using the programme Calisto (Setaram).

2.12 NMR

^{1}H and ^{13}C nuclear magnetic resonance spectra were obtained at 25 °C using a 400 MHz Varian Unity Inova (100 MHz for ^{13}C) using DMSO-d_6 as solvent.

2.13 FTIR

A Thermo Nicolet iS10 spectrometer with ATR attachment was employed. A background scan was collected immediately before the sample scan.

2.14 SEM

SEM images were collected on a Zeiss Merlin Field Emission Scanning Electron Microscope, equipped with GEMINI II column, using the In-Lens detector. Samples were doubly gold-coated and the instrument was operated at 5.0 kV.

2.15 PASCal

The programme PASCal[7] (Principal Axis Strain Calculator) was accessed at http://pascal.chem.ox.ac.uk. It is used to determine a set of principal axes and calculate linear and volumetric coefficients of thermal expansion.

2.16 Materials Studio

Refined single-crystal X-ray structures were used along with the CASTEP and DMol3 modules of Materials Studio[8] to investigate electrostatic interactions between sets of molecules. An electrostatic potential field would be calculated for one set of molecules and mapped onto the electron density isosurface of another, adjacent set of molecules.

2.17 References

1 Nakagawa, T.; Kumaki, D.; Nishida, J.; Tokito, S.; Yamashita, Y. *Chem. Mater.* **2008**, *20*, 2615.

2 *SAINT Data Reduction Software*, Version 6.45; Bruker AXS Inc.: Madison, WI, 2003.

3 *SADABS*, Version 2.05; Bruker AXS Inc.: Madison, WI, 2002.

4 Sheldrick, G. M. A Short History of SHELX. *Acta Crystallogr.* **2008**, A*64*, 112.

5 Barbour, L. J. *Supramol. Chem.* **2001**, *1*,189.

6 Spek, A. L. .*Acta Crystallogr.* **2009**, D*65*, 148.

7 Cliffe, M. J.; Goodwin, A. L. *J. Appl. Crystallogr.* **2012**, *45*, 1321.

8 *Materials Studio Modelling Environment*, Version 6.0.0; Accelrys Software Inc.: San Diego, 2011.

Chapter 3

Uniaxial negative thermal expansion facilitated by weak host-guest interactions

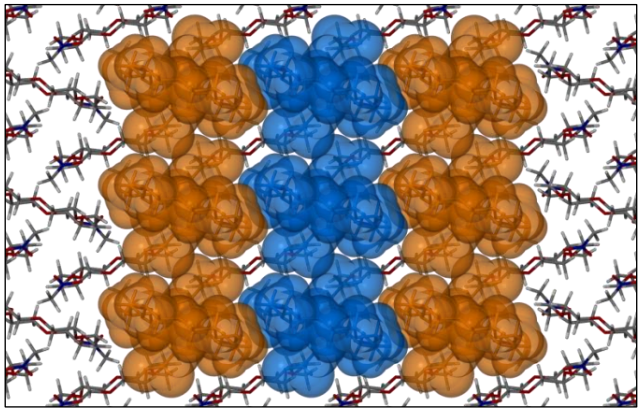

3.1 Communication in *Chemical Communications*

Contributions of the author:

- Design of project with Dr Vincent J. Smith
- Preparation of the solvate
- Collection of temperature-resolved single-crystal X-ray data
- Solution and refinement of single-crystal X-ray structures
- Determination of principal axes and thermal expansion coefficients
- Recording of PXRD patterns
- Recording of TGA and DSC thermograms
- Determination of a plausible mechanism with Charl X. Bezuidenhout
- Interpretation of results with Dr Vincent J. Smith and Charl X. Bezuidenhout
- Writing the first draft of the article

ChemComm

COMMUNICATION

View Article Online
View Journal | View Issue

Uniaxial negative thermal expansion facilitated by weak host–guest interactions†

Cite this: *Chem. Commun.*, 2014, 50, 4238

Received 31st January 2014,
Accepted 4th March 2014

DOI: 10.1039/c4cc00849a

www.rsc.org/chemcomm

Emile R. Engel, Vincent J. Smith, Charl X. Bezuidenhout and Leonard J. Barbour*

A nitromethane solvate of 18-crown-6 was investigated by means of variable-temperature single-crystal X-ray diffraction in response to a report of abnormal unit cell contraction. Exceptionally large positive thermal expansion in two axial directions and negative thermal expansion along the third was confirmed. The underlying mechanism relies exclusively on weak electrostatic interactions to yield a linear thermal expansion coefficient of -129×10^{-6} K^{-1}, the largest negative value yet observed for an organic inclusion compound.

A computational tool developed by van de Streek and Motherwell was used to search the Cambridge Structural Database for previously unidentified polymorphs. Two structures of the nitromethane solvate of 18-crown-6 (**18C6N**) were flagged (both in the space group $P2_1/n$ with a host–guest ratio of 1 : 2). The authors described the pair not as polymorphs but as an example of "extremely anisotropic unit cell contraction".[1]

Unit cell dimensions for **18C6N** were first reported by McLachlan[2] and the single-crystal X-ray structure determined by De Boer and co-workers.[3] The structure was later redetermined at 22 °C to greater precision by Rogers *et al.*, who also investigated the crystal structure at −150 °C and concluded that at low and high temperature, the crystal has "essentially the same structure except for the obvious exception of weak CH···O bonds".[4] Indeed, the two structures reported by Rogers were those identified in the van de Streek and Motherwell polymorph search.

For the present study, crystals of **18C6N** were prepared by dissolving 18-crown-6 in hot nitromethane, followed by filtering and allowing for slow evaporation of the solvent. A crystal was selected while under mother liquor, removed and its surface immediately coated with epoxy to prevent desolvation. The crystal was then glued to the end of a glass fibre and mounted on a goniometer under a liquid nitrogen stream at 90 K. Full intensity datasets were collected and the single-crystal X-ray structures were determined at regular temperature intervals in the range 90–273 K; unit cell dimensions were determined to high precision with e.s.d. values in the range 0.0010–0.0023 Å for axis lengths. The *b* and *c* unit cell lengths increased steadily and dramatically with temperature while the *a* axis contracted from 9.31 to 9.12 Å. No abrupt changes were observed that might indicate a phase transformation (Fig. S1, ESI†).

Reports of anomalous thermal expansion have become more frequent in recent years but are dominated by inorganic negative linear and volumetric thermal expansion. Typical examples include silicates and zirconium tungstenates that incorporate strong covalent bonds as well as MOF-5 and related IRMOFs constructed with metal–ligand coordination bonds.[5,6] In comparison, organic compounds displaying these properties are still relatively rare, though remarkable examples exist.[7]

The degree of linear thermal expansion has been quantified using a coefficient defined as $\alpha_l = (l_T - l_0)/(l_0(T - T_0))$ where l_T is the axis length at the final temperature T and l_0 the axis length at the initial temperature T_0. Similarly, the coefficient of volumetric thermal expansion is $\alpha_v = (V_T - V_0)/(V_0(T - T_0))$ where V_T is the unit cell volume at temperature T and V_0 the volume at T_0. An important adjustment is needed for crystal systems where the unit cell axes are not mutually orthogonal.[6] It is necessary to determine an orthogonal set of axes and to calculate coefficients of linear thermal expansion along *these principal axes* instead of the crystallographic axes (*i.e.* a strain calculation). The principal axes are labelled *X*1, *X*2 and *X*3 and are assigned in order of increasing magnitude.

For **18C6N** in the 90–273 K temperature range, principal axes and linear expansion coefficients were calculated using the programme *PASCal*.[8] The *X*1, *X*2 and *X*3 axes are approximately along [−60−1], [−101] and [0−10], respectively. Fig. 1 shows how the principal axis lengths change with increasing temperature. The contraction of *X*1 is overwhelmingly influenced by changes along the crystallographic *a* axis and, similarly, the expansion of *X*2 is dominated by changes in the *c* direction. Fig. S2 (ESI†) illustrates the orientation of *X*1 and *X*2 with respect to the crystallographic

Department of Chemistry and Polymer Science, University of Stellenbosch, Private Bag X1, Matieland, 7602, South Africa. E-mail: ljb@sun.ac.za

† Electronic supplementary information (ESI) available: Synthesis, experimental methods, summaries of crystallographic data, PXRD diffractograms, computational parameters and thermal analysis. CCDC 984223–984232. For ESI and crystallographic data in CIF or other electronic format see DOI: 10.1039/c4cc00849a

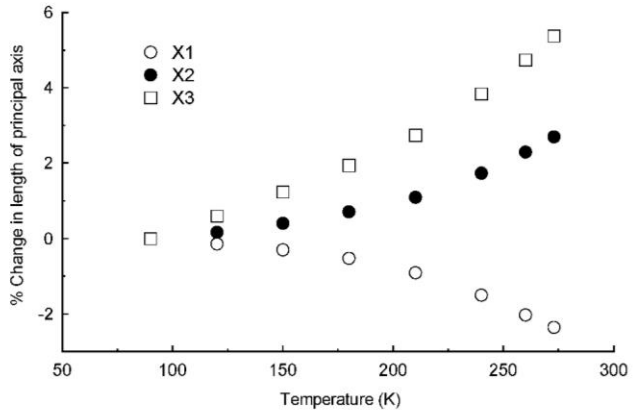

Fig. 1 Percentage changes in principal axis lengths as a function of temperature.

unit cell. The coefficients of linear thermal expansion are −129(15), 144(14) and 282(16) × 10^{-6} K^{-1} for *X*1, *X*2 and *X*3, respectively. The coefficient of volumetric thermal expansion is 311(17) × 10^{-6} K^{-1}. The negative component of thermal expansion is at least four times greater than that reported recently for another multi-component organic crystal (a complex containing 1,3,5-benzenetricarboxylic acid, 2,6-dimethylaniline and water) and calculated over a similar temperature range (120–300 K).[9]

A temperature-resolved powder X-ray diffraction experiment (Fig. S3, ESI†) was carried out by cooling a sample of **18C6N** from 293 K to 123 K and then heating to 273 K while collecting data at 30 K intervals. The results show a gradual, smooth transition between the high and low temperature PXRD patterns as is typical of thermal expansion phenomena that do not involve phase transitions. The absence of **18C6N** phase transformations was confirmed by a DSC experiment (Fig. S4, ESI†). Only minor thermal events were identified where residual nitromethane freezes and melts.

Two analogues of **18C6N** were examined for similar behaviour given that they crystallise with similar structures. The acetonitrile solvate of 18-crown-6 had already been reported with structures determined at 123 K and room temperature; the room temperature structure crystallises in the space group $P2_1/n$ (*i.e.* as does **18C6N**) but the low temperature structure is triclinic, suggesting that a temperature-induced phase transformation may occur.[10] We prepared the iodomethane solvate for the first time and structural data in the temperature range 90–273 K indicate different degrees of positive thermal expansion along all axes, with the largest coefficient of linear thermal expansion being 129(5) × 10^{-6} K^{-1} for *X*3. However, neither analogue appears to emulate the large negative linear thermal expansion observed over a broad temperature range for **18C6N**. It is therefore clear that the thermal expansion properties of this organic inclusion compound system may be dramatically influenced by changing the guest even if the overall packing arrangement is preserved. Indeed, the expansion along one axis switches from negative to positive by replacing nitromethane with iodomethane. This phenomenon has been alluded to but not previously observed.[11]

Several mechanisms resulting in negative thermal expansion have been described. Arguably the most important of these have involved bridging atoms and rigid unit vibrational modes; magnetostriction; and electronic effects.[6,12] Das *et al.* reported extremely large positive and negative thermal expansion for a dumbbell-shaped organic molecule. The mechanism was shown to depend on a helical pattern of strong O–H···O hydrogen bonds.[13] The 1,3,5-benzenetricarboxylic acid-based compound mentioned earlier is a salt hydrate with an extensive network of ionic and hydrogen bonds. In contrast, an organic polymorph with no ionic interactions or hydrogen bonds was reported recently as undergoing remarkable anisotropic thermal expansion. The mechanism in that case is said to depend on steric effects.[14] In **18C6N** there is a similar absence of strong directional intermolecular interactions.

A variety of interactions were investigated computationally for **18C6N** (details provided in the ESI†). The most dominant of these appears to be the host–guest interaction where the guest methyl group is inserted into the crown cavity (−7.16 kcal mol^{-1}) (Fig. S5a, ESI†). These interactions facilitate the formation of 1 : 2 host–guest adducts that can be considered as supramolecular building blocks (Fig. S5c, ESI†). Although their cumulative effect is strongly stabilising, it is mainly weak C–H···O hydrogen bonds that contribute to this interaction. Generally, C–H···O bonds are in the range 3–4 Å for the donor–acceptor atom distance and 110° is accepted as a lower limit for the hydrogen bond angle.[15] The most linear of the hydrogen bonds in **18C6N** is C7–H···O1 with an angle of 175.4° and a C–O distance of 3.305(1) Å while the shortest C–O contact is 3.132(1) Å in length with a C–H···O angle of 106° (close to the accepted lower limit).

The next strongest interaction occurs between two guest molecules (of adjacent hosts) which have their dipoles orientated in opposite directions along the *b* axis (Fig. S5b, ESI†). The stabilisation energy of this interaction is −2.22 kcal mol^{-1}. These interactions link adjacent host–guest adducts together in columns parallel to the *b* axis. Thus a combination of weak host–guest C–H···O hydrogen bonds and long-range dipole–dipole stabilisation promotes the formation of columns that dominate the crystal packing (Fig. 2).

Several features contribute to the complex mechanism of negative linear thermal expansion and it is useful to separate these components by considering molecular movement in each of the crystallographic axial planes. First consider the *ab* plane shown in Fig. 3 (top). The distance between adjacent guest molecules along the *b* axis increases as expected with increasing temperature.

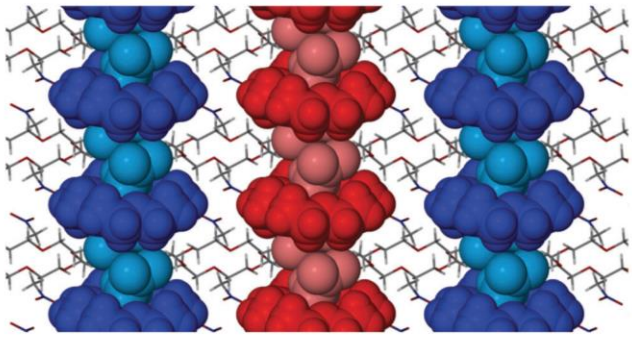

Fig. 2 Packing diagram of **18C6N** viewed along [100]. Host–guest columns that extend along the crystallographic *b* axis are shown in blue and red.

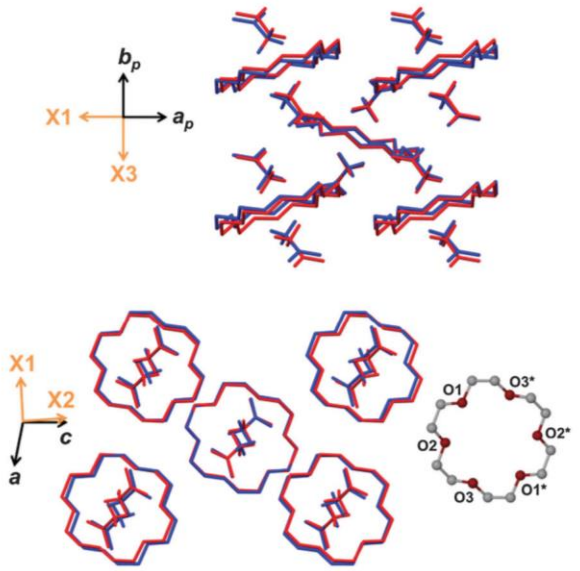

Fig. 3 Projections of the *ab* (top) and *ac* (bottom) planes with overlaid structures at 90 K (blue) and 273 K (red). Hydrogen atoms have been omitted for clarity.

Similarly the distance between the host and guest centroids increases steadily. In general intermolecular interactions lengthen with increasing temperature because atomic vibrations become larger and because the vibrations are anharmonic.[6] While the adjacent guests move apart with increasing temperature the host–guest adducts tilt (*i.e.* the plane of the non-hydrogen atoms of the host crown ether becomes less perpendicular to the *b* axis). The combined effect of increasing intermolecular distances and tilting of the host–guest adducts accounts for the large expansion of *X*3.

In the *ac* plane (Fig. 3, bottom) conformational adjustment of the crown ether molecule is concomitant with the host–guest columns shifting apart along [001] and closer together along [100]. The molecular electrostatic potential maps in Fig. 4 shed light on why the three unique pairs of adjacent columns shift as they do relative to one another. The three maps provide an indication of the relative strength of electrostatic attraction between the columns of each pair. The map of B onto C shows the greatest negative electrostatic potential and the only region of high positive potential, indicating that the B–C interaction is

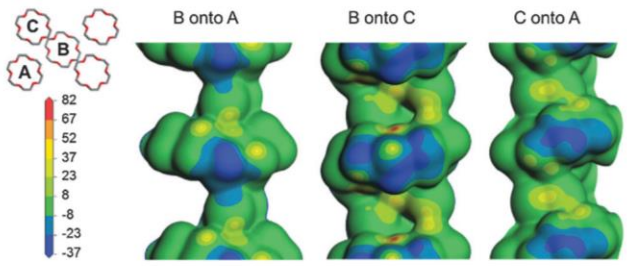

Fig. 4 The molecular electrostatic potential of each column is mapped onto the electron density contour of an adjacent column. The scale bar values are given in kcal mol^{-1}.

the strongest of the three. Since the B–A and C–A interactions are weaker they are more easily overcome when the crystal is heated. While the B–C spacing is preserved, the B–A and C–A distances shrink in response to an increase in temperature and this manifests as a contraction of *X*1.

Across the centre of the crown ether molecule the O1–O1* and O3–O3* (* denotes a relationship about a site of −1 symmetry) distances shrink by 0.038 Å and 0.060 Å, respectively. These contractions are consistent with the contraction of *X*1. The O2–O2* distance increases by 0.093 Å and contributes to the expansion of *X*2. Interestingly, two C–H···O contact distances become shorter as the temperature increases. One of these is the convincing hydrogen bond C7–H···O1 with a high degree of linearity that is mostly preserved with increasing temperature.

In the *bc* plane it is clear that the guest methyl rotates as the temperature changes (Fig. S5, ESI†). The potential for rotation about the N1–C7 bond is the reason the C7–H···O1 hydrogen bond remains intact and indeed shortens despite an increase in temperature and changes in the host conformation.

Variable temperature structure determination has confirmed that **18C6N** undergoes large anisotropic thermal expansion in the temperature range 90–273 K without any phase transformation. Weak C–H···O hydrogen bonds facilitate the formation of 1:2 host–guest adducts and dipole–dipole stabilisation allows these adducts to stack as columns. The mechanism giving rise to the negative component of thermal expansion involves anisotropic shifting of host–guest columns relative to one another with simultaneous adjustments in molecular conformation. Negative uniaxial thermal expansion in the absence of strong directional interactions is extremely rare and the case presented here confirms that weak interactions may give rise to this phenomenon. Furthermore, this study raises the exciting prospect that extreme thermal expansion anisotropy in isoskeletal organic inclusion compounds might be controlled by simple variation of the guest, even to the extent of complete reversal.[16]

We are grateful to the SARChI Programme of the Department of Science and Technology and the National Research Foundation (South Africa) for financial support.

Notes and references

1 J. van de Streek and S. Motherwell, *Acta Crystallogr., Sect. B: Struct. Sci.*, 2005, **61**, 504.
2 R. D. McLachlan, *Spectrochim. Acta, Part A*, 1974, **30**, 2153.
3 J. de Boer, D. Reinhoudt, S. Harkema, G. J. van Hummel and F. de Jong, *J. Am. Chem. Soc.*, 1982, **104**, 4073.
4 (*a*) R. D. Rogers and L. M. Green, *J. Inclusion Phenom.*, 1986, **4**, 77; (*b*) R. D. Rogers and P. D. Richards, *J. Inclusion Phenom.*, 1987, **5**, 631.
5 T. A. Mary, J. S. O. Evans, T. Vog and A. W. Sleight, *Science*, 1996, **272**, 90.
6 G. D. Barrera, J. A. O. Bruno, T. H. K. Barron and N. L. Allan, *J. Phys.: Condens. Matter*, 2005, **17**, R217.
7 (*a*) M. Zakrzewski and M. A White, *J. Phys. Chem.*, 1990, **94**, 2203; (*b*) H. Birkedal, D. Schwarzenbach and P. Pattison, *Angew. Chem., Int. Ed.*, 2002, **41**, 754; (*c*) R. H. Jones, K. S. Knight, W. G. Marshall, J. Clews, R. J. Darton, D. Pyatt, S. J. Coles and P. N. Horton, *CrystEngComm*, 2014, **16**, 237.
8 J. Cliffe and A. L. Goodwin, *J. Appl. Crystallogr.*, 2012, **45**, 1321.
9 S. Bhattacharya and B. K. Saha, *Cryst. Growth Des.*, 2012, **12**, 4716.
10 (*a*) R. D. Rogers, P. D. Richards and E. J. Voss, *J. Inclusion Phenom. Mol. Recognit. Chem.*, 1988, **6**, 65; (*b*) R. L. Garrell, J. C. Smyth,

F. R. Fronczek and R. D. Gandour, *J. Inclusion Phenom. Mol. Recognit. Chem.*, 1988, **6**, 73.
11 I. E. Collings, M. G. Tucker, D. A. Keen and A. L. Goodwin, *CrystEngComm*, 2014, DOI: 10.1039/C3CE42165A.
12 W. Zhou, H. Wu, T. Yildirim, J. R. Simpson and A. R. Hight Walker, *Phys. Rev. B: Condens. Matter Mater. Phys.*, 2008, **78**, 054114.
13 D. Das, T. Jacobs and L. Barbour, *Nat. Mater.*, 2010, **9**, 36.
14 S. Bhattacharya and B. K. Saha, *CrystEngComm*, 2014, **16**, 2340.
15 G. Desiraju, *Acc. Chem. Res.*, 1996, **29**, 441.
16 (*a*) G. O. Lloyd, J. Alen, M. W. Bredenkamp, E. J. C. de Vries, C. Esterhuysen and L. J. Barbour, *Angew. Chem., Int. Ed.*, 2006, **45**, 5354; (*b*) L. J. Barbour, D. Das, T. Jacobs, G. O. Lloyd and V. J. Smith, *Supramolecular Chemistry: From Molecules to Nanomaterials*, John Wiley & Sons, 2012.

3.2 Supporting information

Uniaxial negative thermal expansion facilitated by weak host-guest interactions

Emile R. Engel, Vincent J. Smith, Charl X. Bezuidenhout and Leonard J. Barbour*

Materials

The 18-crown-6 and nitromethane were purchased from Sigma-Aldrich. Methyl iodide was obtained from Merck. All chemical were used as received.

Synthesis

The methyl iodide solvate ($C_{12}H_{24}O_6.2CH_3I$) was prepared from a concentrated solution of 18-crown-6 in neat methyl iodide. The solution was stirred for 2 hours at room temperature after which it was stored at ca. 5 °C for slow evaporation. Crystals were obtained after 5 days.

Single crystal X-ray diffraction

Single crystal X-ray diffraction data were collected using a Bruker APEX-II DUO equipped with a CCD area-detector diffractometer and an Oxford Cryosystems 700Plus cryostat. A multilayer monochromator with MoKα radiation (λ = 0.71073 Å) from an Incoatec IμS microsource was used.

Data reduction was carried out by means of the standard procedure using the Bruker software package SAINT[1] and the absorption corrections and the correction of other systematic errors were performed using SADABS.[2] The structures were solved by direct methods using SHELXS-97 and refined using SHELXL-97.[3] X-Seed[4] was used as the graphical interface for the SHELX program suite. Hydrogen atoms were placed in calculated positions using riding models.

Table S1: *Crystallographic details for **18C6N***

Empirical formula	$C_{12}H_{24}O_6.2CH_3NO_2$	$C_{12}H_{24}O_6.2CH_3NO_2$	$C_{12}H_{24}O_6.2CH_3NO_2$	$C_{12}H_{24}O_6.2CH_3NO_2$
Formula weight	386.40	386.40	386.40	386.40
Temperature (K)	**90(2)**	**120(2)**	**150(2)**	**180(2)**
Wavelength (Å)	0.71073	0.71073	0.71073	0.71073
Crystal system	Monoclinic	Monoclinic	Monoclinic	Monoclinic
Space group	*P* $2_1/n$	*P* $2_1/n$	*P* $2_1/n$	*P* $2_1/n$
Unit cell dimensions (Å, °)	*a* = 9.3091(14)	*a* = 9.2976(13)	*a* = 9.2849(12)	*a* = 9.2668(13)
	b = 7.8112(12)	*b* = 7.8579(11)	*b* = 7.9079(10)	*b* = 7.9623(11)
	c = 13.619(2)	*c* = 13.6419(19)	*c* = 13.6739(18)	*c* = 13.7151(19)
	α = 90	α = 90	α = 90	α = 90
	β = 100.710(2)	β = 100.755(2)	β = 100.818(2)	β = 100.907(2)
	γ = 90	γ = 90	γ = 90	γ = 90
Volume ($Å^3$)	973.1(3)	979.2(2)	986.2(2)	993.7(2)
Z	2	2	2	2
Calculated density (g cm^{-3})	1.319	1.311	1.301	1.291
Absorption coefficient (mm^{-1})	0.112	0.111	0.110	0.109
F_{000}	416	416	416	416
Approx. crystal size (mm^3)	0.27 x 0.36 x 0.40	0.27 x 0.36 x 0.40	0.27 x 0.36 x 0.40	0.27 x 0.36 x 0.40
θ range for data collection (°)	2.5 to 28.4	2.5 to 28.4	2.5 to 29.8	2.5 to 28.3
Miller index ranges	$-12 \le h \le 12$; $-10 \le k \le 10$; $-18 \le l \le 18$	$-12 \le h \le 12$; $-10 \le k \le 10$; $-18 \le l \le 18$	$-12 \le h \le 12$; $-10 \le k \le 10$; $-18 \le l \le 18$	$-12 \le h \le 12$; $-10 \le k \le 10$; $-18 \le l \le 18$
Reflections collected	14088	14239	14663	14545
Independent reflections	2429 [R_{int} = 0.023]	2433 [R_{int} = 0.025]	2626 [R_{int} = 0.024]	2464 [R_{int} = 0.024]
Completeness to θ_{max} (%)	99.8	99.5	93.8	99.7
Data / restraints / parameters	2429 / 0 / 119	2433 / 0 / 119	2626 / 0 / 119	2464/ 0 / 119
Goodness-of-fit on F^2	1.10	1.08	1.09	1.09
Final R indices [I > 2σ(I)]	R1 = 0.0316; wR2 = 0.0845	R1 = 0.0333; wR2 = 0.0872	R1 = 0.0377; wR2 = 0.0965	R1 = 0.0406; wR2 = 0.1031
R indices (all data)	R1 = 0.0356; wR2 = 0.0872	R1 = 0.0382;wR2 = 0.0907	R1 = 0.0465; wR2 = 0.1017	R1 = 0.0492; wR2 = 0.1087
Largest diff. peak and hole (e $Å^{-3}$)	-0.27, 0.35	-0.22, 0.31	-0.23, 0.28	-0.23, 0.30

Table S1 continued: *Crystallographic details for **18C6N***

Empirical formula	$C_{12}H_{24}O_6.2CH_3NO_2$	$C_{12}H_{24}O_6.2CH_3NO_2$	$C_{12}H_{24}O_6.2CH_3NO_2$	$C_{12}H_{24}O_6.2CH_3NO_2$
Formula weight	386.40	386.40	386.40	386.40
Temperature (K)	**210K**	**240K**	**260K**	**273K**
Wavelength (Å)	0.71073	0.71073	0.71073	0.71073
Crystal system	Monoclinic	Monoclinic	Monoclinic	Monoclinic
Space group	*P* $2_1/n$	*P* $2_1/n$	*P* $2_1/n$	*P* $2_1/n$
Unit cell dimensions (Å, °)	*a* = 9.2363(13)	*a* = 9.1902(15)	*a* = 9.1488(15)	*a* = 9.1231(14)
	b = 8.0254(11)	*b* = 8.1108(13)	*b* = 8.1812(13)	*b* = 8.2311(13)
	c = 13.7678(19)	*c* = 13.853(2)	*c* = 13.928(2)	*c* = 13.982(2)
	α = 90	α = 90	α = 90	α = 90.00
	β = 101.054(2)	β = 101.313(2)	β = 101.529(2)	β = 101.676(2)
	γ = 90	γ = 90	γ = 90	γ = 90.00
Volume ($Å^3$)	1001.6(2)	1012.5(3)	1021.5(3)	1028.2(3)
Z	2	2	2	2
Calculated density (g cm^{-3})	1.281	1.267	1.256	1.248
Absorption coefficient (mm^{-1})	0.109	0.107	0.107	0.106
F_{000}	416	416	416	416
Approx. Crystal size (mm^3)	0.27 x 0.36 x 0.40	0.27 x 0.36 x 0.40	0.27 x 0.36 x 0.40	0.27 x 0.36 x 0.40
θ range for data collection (°)	2.5 to 28.3	2.5 to 28.3	2.5 to 28.3	2.5 to 28.3
Miller index ranges	$-12 \le h \le 12$; $-10 \le k \le 10$; $-18 \le l \le 18$	$-12 \le h \le 12$; $-10 \le k \le 10$; $-18 \le l \le 18$	$-12 \le h \le 12$; $-10 \le k \le 10$; $-18 \le l \le 18$	$-11 \le h \le 11$; $-10 \le k \le 10$; $-18 \le l \le 18$
Reflections collected	14646	14825	14870	15176
Independent reflections	2477 [R_{int} = 0.025]	2509 [R_{int} = 0.026]	2530, [R_{int} = 0.028]	2542, [R_{int} = 0.028]
Completeness to θ_{max} (%)	99.4	99.5	99.5	99.3
Data / restraints / parameters	2477 / 0 / 119	2509 / 0 / 119	2530 / 0 / 119	2542 / 0 / 119
Goodness-of-fit on F^2	1.067	1.113	1.084	1.047
Final R indices [I > 2σ(I)]	R1 = 0.0472; wR2 = 0.1224	R1 = 0.0604; wR2 = 0.1757	R1 = 0.0737; wR2 = 0.2245	R1 = 0.0823; wR2 = 0.2599
R indices (all data)	R1 = 0.0602; wR2 = 0.1311	R1 = 0.0821; wR2 = 0.1930	R1 = 0.1035; wR2 = 0.2492	R1 = 0.1167; wR2 = 0.2926
Largest diff. peak and hole (e $Å^{-3}$)	-0.28, 0.37	-0.33, 0.39	-0.36, 0.42	-0.34, 0.47

Table S2: *Crystallographic details for $C_{12}H_{24}O_6.2CH_3I$*

Empirical formula	$C_{12}H_{24}O_6.2CH_3I$	$C_{12}H_{24}O_6.2CH_3I$
Formula weight	548.18	548.18
Temperature (K)	**90K**	**273K**
Wavelength (Å)	0.71073	0.71073
Crystal system	Monoclinic	Monoclinic
Space group	$P2_1/n$	$P2_1/n$
Unit cell dimensions (Å, °)	*a* = 8.9459(4)	*a* = 9.0683(3)
	b = 8.4921(3)	*b* = 8.6955(2)
	c = 14.2485(5)	*c* = 14.2945(5)
	α = 90	α = 90
	β = 107.082(2)	β = 106.751(2)
	γ = 90	γ = 90
Volume ($Å^3$)	1034.70(7)	1079.34(6)
Z	2	2
Calculated density (g cm^{-3})	1.760	1.687
Absorption coefficient (mm^{-1})	3.061	2.934
F_{000}	536	536
Approx. Crystal size (mm^3)	0.05 x 0.15 x 0.15	0.05 x 0.15 x 0.15
θ range for data collection (°)	2.4 to 28.3	2.4 to 28.3
Miller index ranges	$-7 \le h \le 11$; $-11 \le k \le 8$; $-18 \le l \le 18$	$-7 \le h \le 12$; $-11 \le k \le 8$; $-19 \le l \le 19$
Reflections collected	8100	8606
Independent reflections	2568 [R_{int} = 0.018]	2677 [R_{int} = 0.019]
Completeness to θ_{max} (%)	99.9	99.6
Data / restraints / parameters	2568 / 0 / 101	2677 / 0 / 101
Goodness-of-fit on F^2	1.052	1.026
Final R indices [I > 2σ(I)]	R1= 0.0154 wR2 = 0.0386	R1= 0.0353; wR2 = 0.0797
R indices (all data)	R1= 0.0165; wR2 = 0.0391	R1= 0.0512; wR2 = 0.0878
Largest diff. peak and hole (e $Å^{-3}$)	-0.48, 0.75	-0.80, 1.02

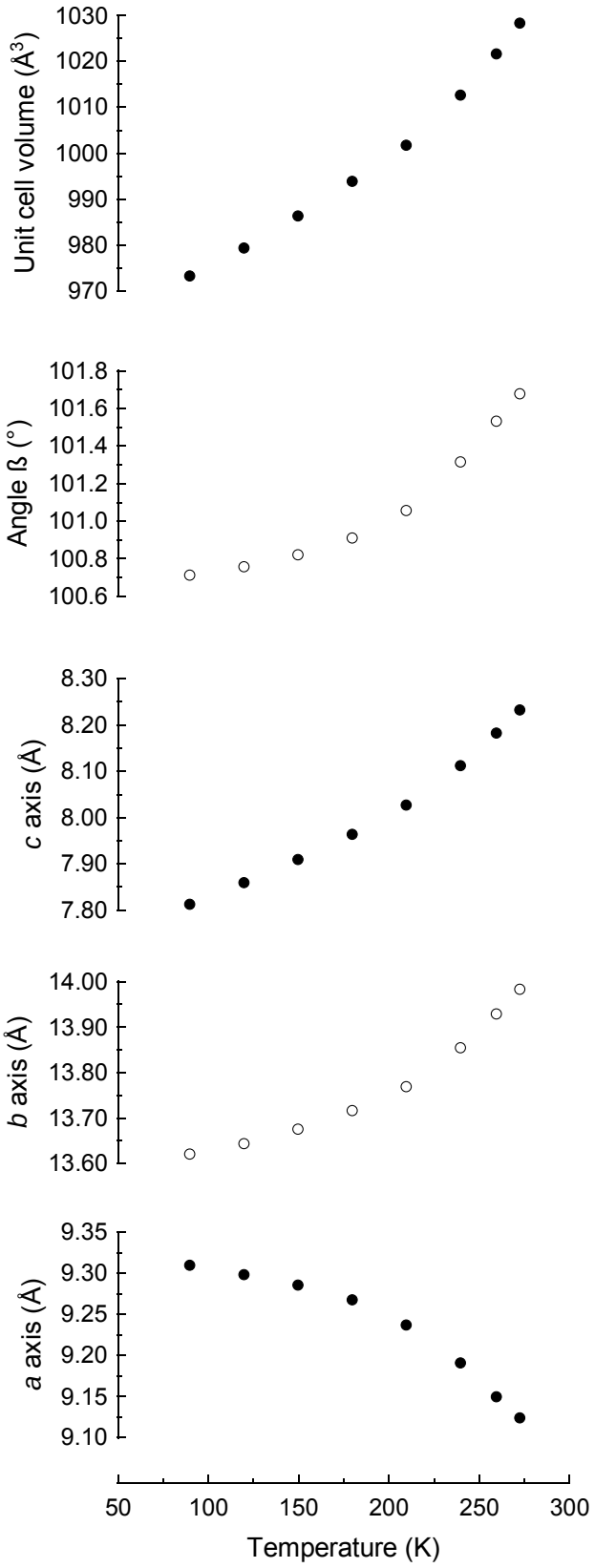

Figure S1: *Unit cell dimensions and volume plotted against temperature in the range 90-273 K over which the same crystal was studied.*

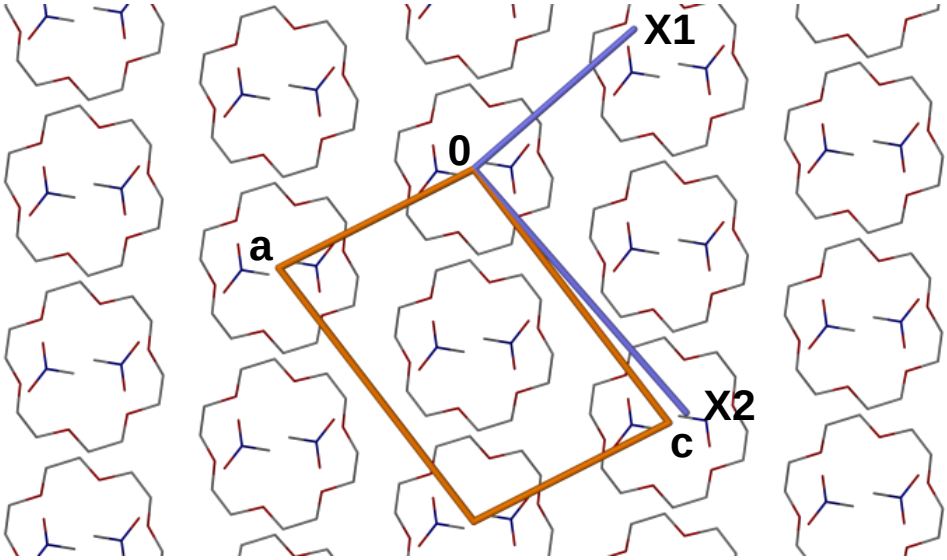

Figure S2: *Orientation of X1 and X2 with respect to the crystallographic unit cell as viewed along [0 1 0] (which is collinear with X3).*

Cryogenic Powder X-ray Diffraction Powdered

Cryogenic powder X-ray diffraction samples were placed in a sealed glass capillary. X-ray powder diffractograms were measured using Cu Kα radiation (λ= 1.5418 Å, 40 kV and 30 mA) on a PANalytical instrument operating in Bragg-Brentano geometry. The first diffractogram (2θ range of 5º to 40º) was measured at 273 K, after which successive patterns were measured at 20 K intervals. The sample was cooled at a rate of 0.7 K min^{-1} between measurements.

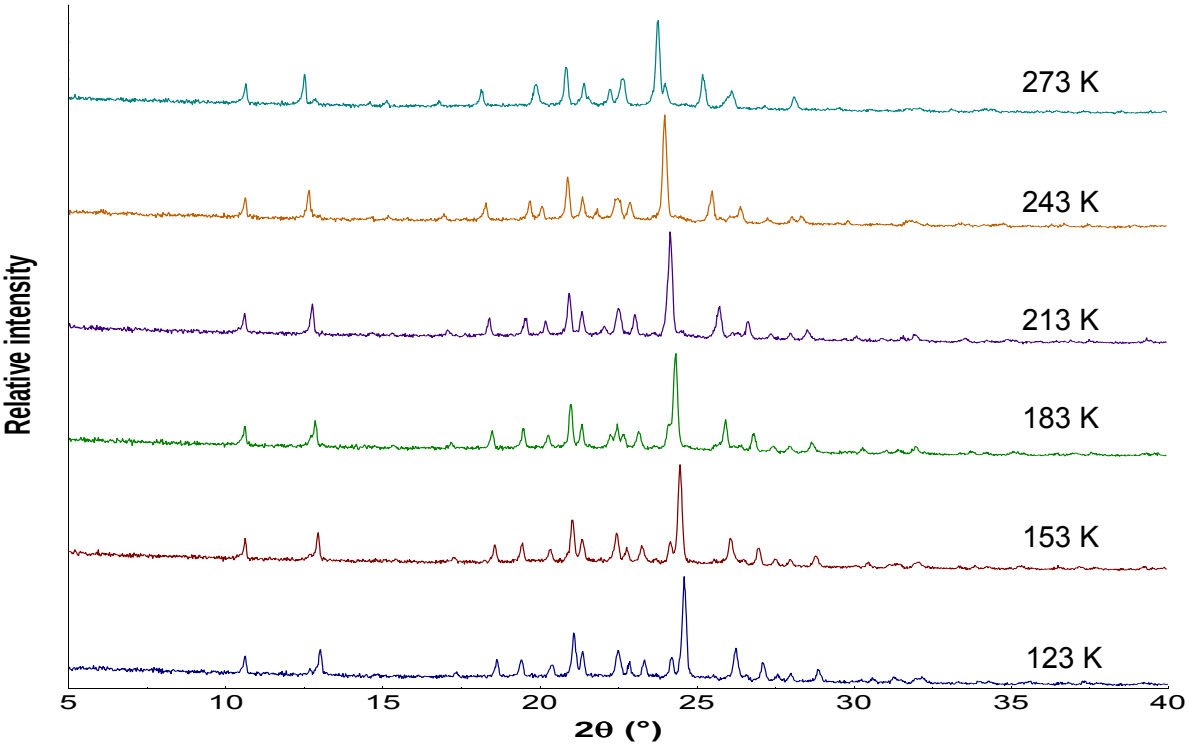

Figure S3: *Temperature-resolved powder diffraction patterns for the same sample of 18C6N over the range 123K-273K.*

Differential Scanning Calorimetry (DSC)

DSC experiments were carried out on a TA Instruments Q100 with Liquid Nitrogen Cooling Accessory (LNCS) and a Q20 with Refrigerated Cooling System (RCS90). The **18C6N** sample was cooled from 0 °C to -150 °C and subsequently heated to 0 °C at a rate of 5 °C/min. The nitromethane sample was cooled from 0 °C to -85 °C and subsequently heated to 0 °C at a rate of 5 °C/min.

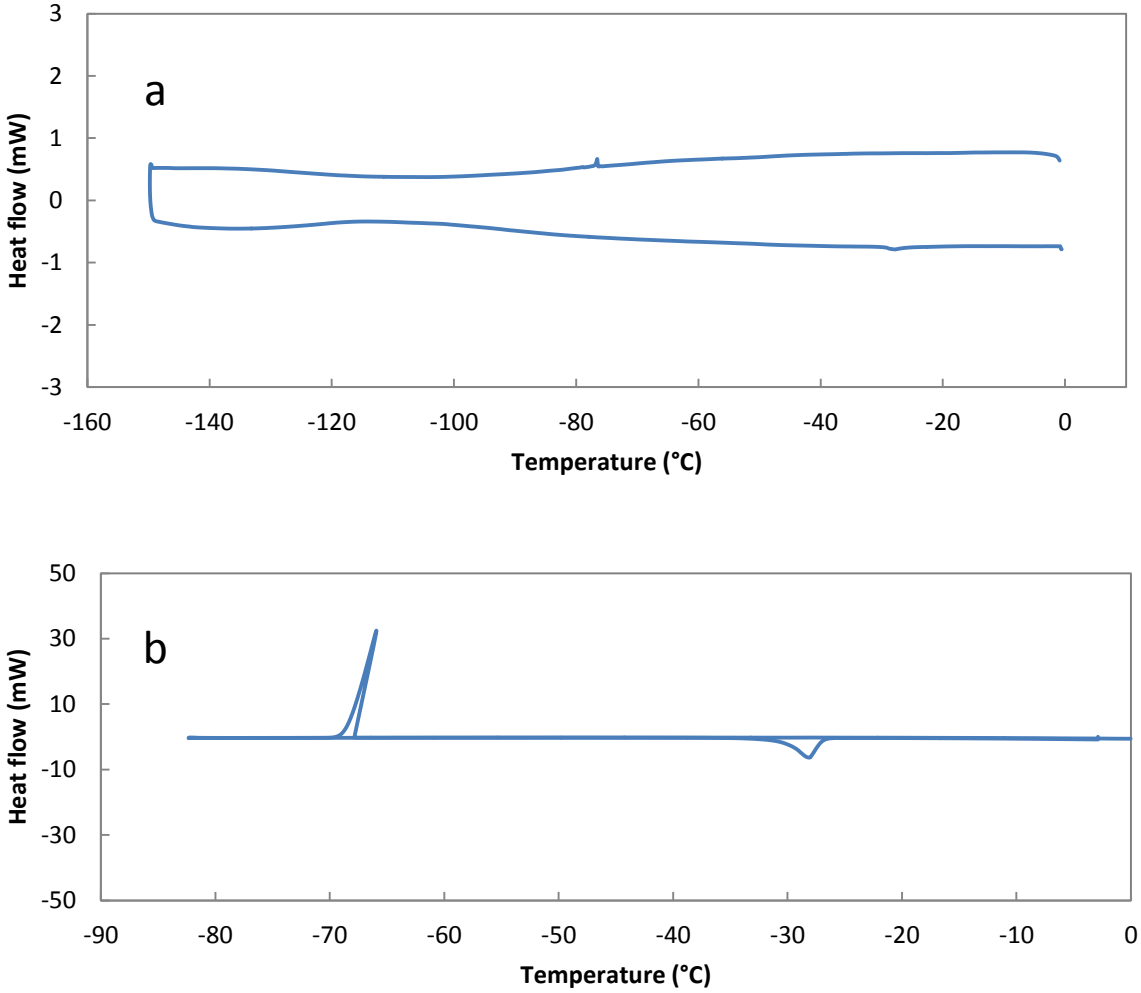

Figure S4: *DSC curves for **18C6N** and neat nitromethane.*

Computational

Atomic coordinates were imported from the refined crystal structures. Only the hydrogen atoms in the framework were optimized as part of a periodic system using the CASTEP module of the *Materials Studio* software suite.[5] The optimizations were performed using the GGA PBE functional with Grimme's DFT-D dispersion correction and thresholds for geometry optimization and SCF convergence were chosen as 1×10^{-5} and 1×10^{-6} eV respectively. The hydrogen optimized crystal structures were then used to determine H-bond angles (Table S2). Single point energies calculations using the DMol3 module of the Materials Studio Software suite were performed using the GGA PBE functional with Grimme's DFT-D dispersion correction and threshold for SCF convergence were chosen as 1×10^{-6} eV. The electron density data obtained from the DMol3 calculations were used to construct the three dimensional 0.01 $e^{-}/Å^{3}$ electron density contour used for the molecular electrostatic potential map (obtained from the same calculation). The 18C6-guests and guest-guest interaction energies were calculated using DFT (Guassian09).[6] The hydrogen atoms which were fully optimized at the mPW1PW91/QZVP level of theory as well as the C-N and C-I bonds in nitromethane

and iodomethane respectively. Although the change in bond length was small, it was required to achieve a geometry convergence. Subsequent single point energies were performed at MP4/QZVP level of theory in order to determine the interaction energies.

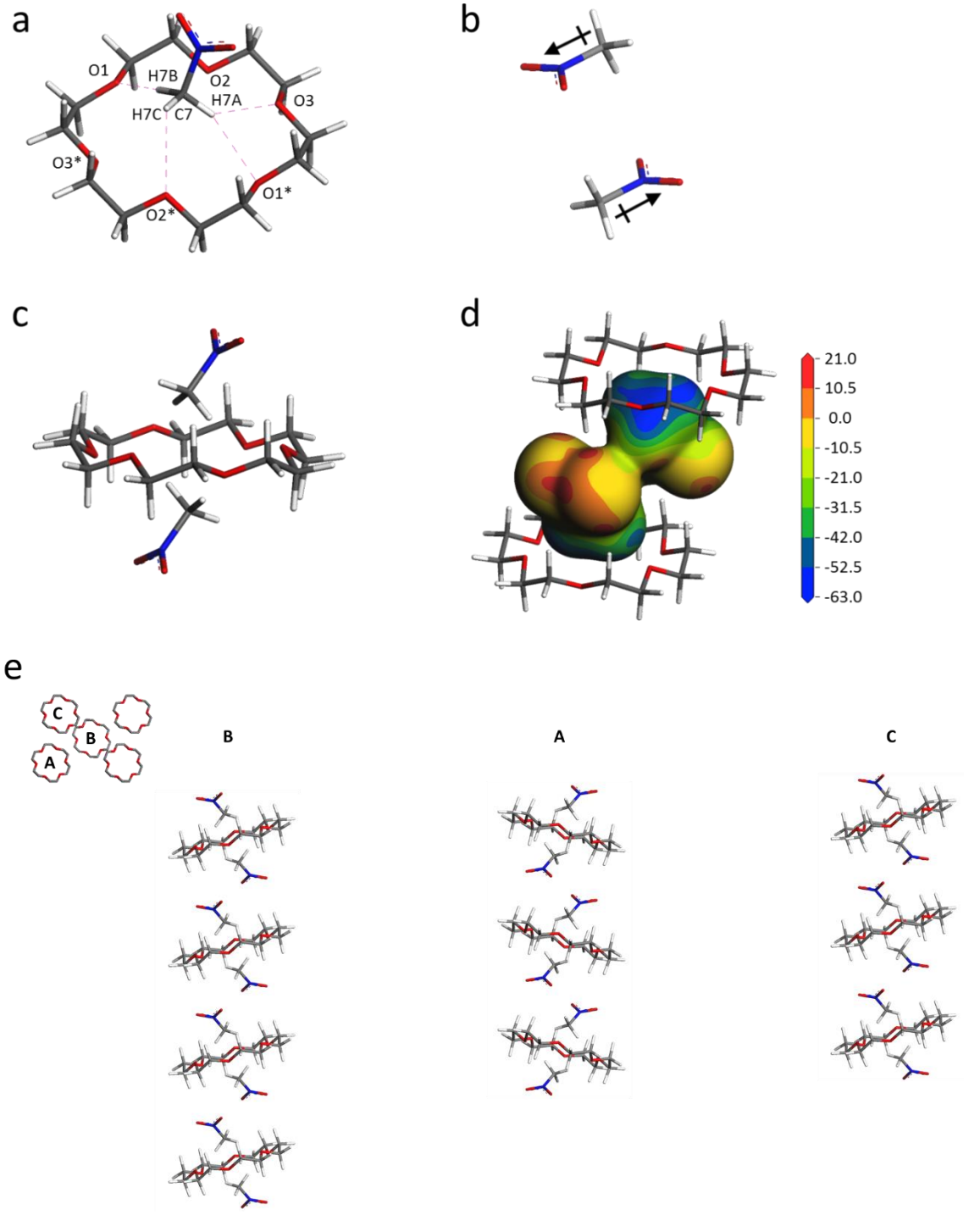

Figure S5: *(a) The computational model used to determine the host-guest interaction energy. The dotted lines indicate the shortest C–H···O contacts. (b) The computational model used to determine the guest-guest interaction energy. (c) 1:2 host-guest adduct (d) The molecular electrostatic potential (MEP) of the host cavity is mapped onto a 0.01 $e^{-}/Å^{3}$ electron density contour of the two guest molecules. The gradation on the scale bar is in kcal/mol with positive values in red and negative values in blue. (e) The computational models used for the MEP calculations of the host-guest columns with the column designations indicated.*

Table S3: *List of host-guest C–H···O contacts for the 90K crystal structure of **18C6N** as determined after optimisation of hydrogen atom positions.*

Contact	D···A distance (Å)	D–H···A angle (°)	273 K distance	273 K angle
C7–H7B···O1	3.305(1)	175.4	3.274	168.1
C7–H7A···O3	3.316(1)	135.8	3.325	152.5
C7–H7A···O1*	3.505(1)	153.6	3.550	137.7
C7–H7B···O2*	3.132(1)	106.8	3.231	122.3

Table S4: *Distances and angles measured for the 90K and 273K crystal structures of **18C6N** after optimisation of hydrogen atom positions.*

Parameter	90K	273K	Parameter change
O1-O1* distance (Å)	5.742	5.704	-0.038
O2-O2* distance (Å)	5.540	5.633	0.093
O3-O3* distance (Å)	5.778	5.718	-0.060
Host-guest distance (Å)	3.040	3.133	0.093
Host-host distance (adjacent along [0 1 0]) (Å)	7.811	8.231	0.420
Guest-guest distance (adjacent along [0 1 0]) (Å)	3.981	4.203	0.222
Torsion angle O4-N1-C7-H7 (°)	165.1	171.8	6.7

PASCal

PASCal calculations were carried out online at http://pascal.chem.ox.ac.uk using the Eulerian finite strain setting.

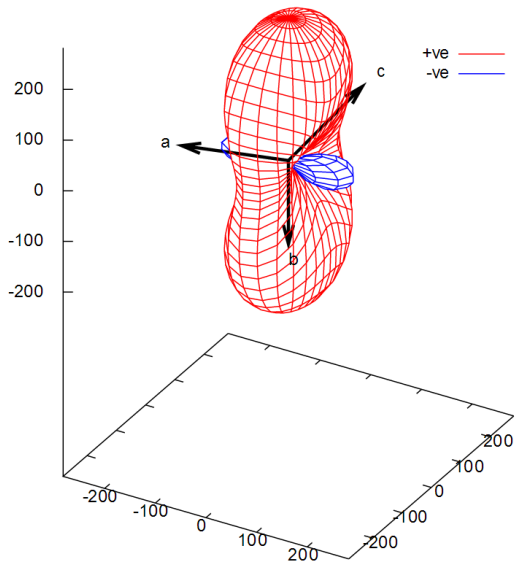

Figure S6: *Expansivity indicatrix generated in PASCal.*

Thermogravimetric analysis (TGA)

Thermogravimetric analysis was carried out using a TA Instruments Q500. The sample was heated at 10 °C/min from room temperature to decomposition. The experimental 32.5 % is in agreement with the expected 31.6 %.based on single-crystal X-ray analysis.

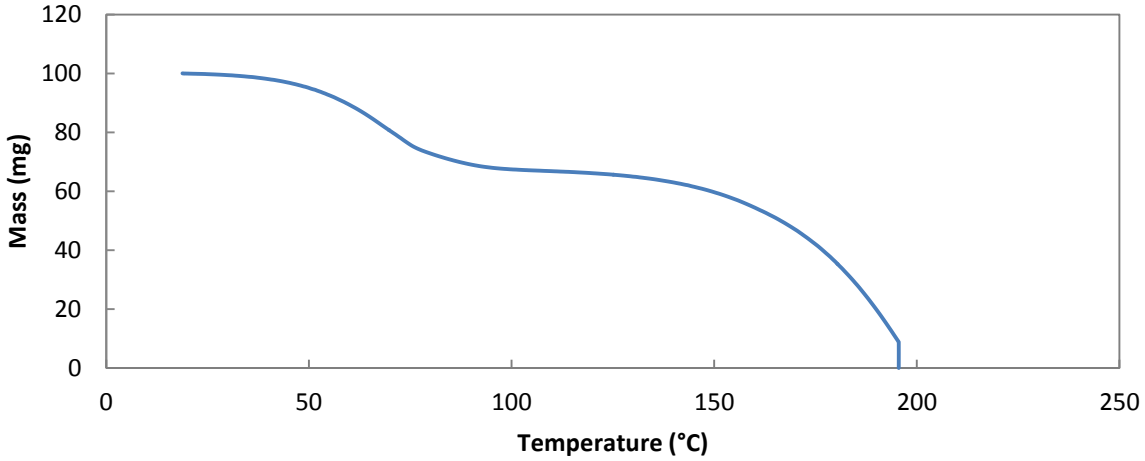

Figure S7: *TGA curve for **18C6N**.*

References

1 *SAINT Data Reduction Software*, Version 6.45; Bruker AXS Inc., Madison, WI, 2003.

2 (a) *SADABS*, Version 2.05; Bruker AXS Inc., Madison, WI, 2002. (b) Blessing, R. H. *Acta Crystallogr.* **1995**, *A51*, 33.

3 Sheldrick, G. M. *Acta Crystallogr.* **2008**, *A64*, 112.

4 Barbour, L. J. *Supramol. Chem.* **2001**, *1*, 189.

5 *Materials Studio Modeling Environment*, Version 6.0.0, Accelrys Software Inc., San Diego, 2011.

6 M. J. Frisch, G. W. Trucks, H. B. Schlegel, G. E. Scuseria, M. A. Robb, J. R. Cheeseman, G. Scalmani, V. Barone, B. Mennucci, G. A. Petersson, H. Nakatsuji, M. Caricato, X. Li, H. P. Hratchian, A. F. Izmaylov, J. Bloino, G. Zheng, J. L. Sonnenberg, M. Hada, M. Ehara, K. Toyota, R. Fukuda, J. Hasegawa, M. Ishida, T. Nakajima, Y. Honda, O. Kitao, H. Nakai, T. Vreven, J. A. Montgomery, Jr., J. E. Peralta, F. Ogliaro, M. Bearpark, J. J. Heyd, E. Brothers, K. N. Kudin, V. N. Staroverov, R. Kobayashi, J. Normand, K. Raghavachari, A. Rendell, J. C. Burant, S. S. Iyengar, J. Tomasi, M. Cossi, N. Rega, J. M. Millam, M. Klene, J. E. Knox, J. B. Cross, V. Bakken, C. Adamo, J. Jaramillo, R. Gomperts, R. E. Stratmann, O. Yazyev, A. J. Austin, R. Cammi, C. Pomelli, J. W. Ochterski, R. L. Martin, K. Morokuma, V. G. Zakrzewski, G. A. Voth, P. Salvador, J. J. Dannenberg, S. Dapprich, A. D. Daniels, Ö. Farkas, J. B. Foresman, J. V. Ortiz, J. Cioslowski, and D. J. Fox, *Gaussian 09*, Revision B.01, Gaussian, Inc., Wallingford CT, 2009.

Chapter 4

Thermoresponsive organic inclusion compounds: modification of thermal expansion behavior by simple guest replacement

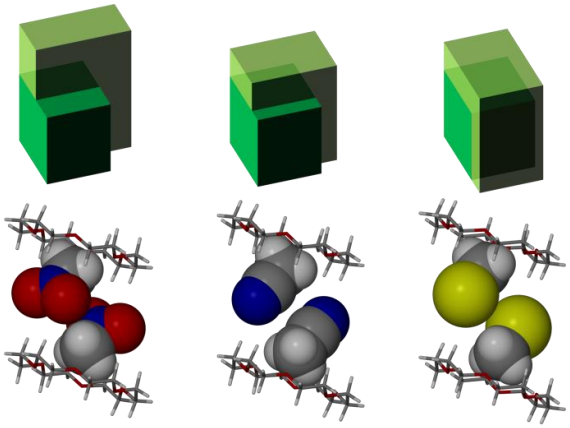

4.1 Article in *Chemistry of Materials*

Contributions of the author:

- Design of the project
- Preparation of solvates
- Collection of temperature-resolved single-crystal X-ray data
- Solution and refinement of single-crystal X-ray structures
- Determination of principal axes and thermal expansion coefficients
- Recording of standard and temperature-resolved PXRD patterns
- Recording of TGA and DSC thermograms
- Computational calculations with Charl X. Bezuidenhout
- Determination of a plausible general mechanism with Charl X. Bezuidenhout
- Interpretation of results with Dr Vincent J. Smith and Charl X. Bezuidenhout
- Writing the first draft of the article

CHEMISTRY OF MATERIALS

Article

pubs.acs.org/cm

Thermoresponsive Organic Inclusion Compounds: Modification of Thermal Expansion Behavior by Simple Guest Replacement

Emile R. Engel, Vincent J. Smith, Charl X. Bezuidenhout, and Leonard J. Barbour*

Department of Chemistry and Polymer Science, University of Stellenbosch, Private Bag X1, Matieland, 7602, South Africa

Supporting Information

ABSTRACT: It is demonstrated that guest replacement in a series of isoskeletal organic inclusion compounds can produce drastic changes in thermal expansion behavior. The compounds **1**, **2**, and **3** have 18-crown-6 as host molecule and nitromethane, acetonitrile, and iodomethane, respectively, as guests. Along the principal axis X1 the linear component of thermal expansion is negative for **1** and **2** but positive for **3**. All three compounds have varying degrees of large volumetric thermal expansion, with coefficients of 378(22), 226(3), and 256(8) × 10^{-6} K^{-1} for **1**, **2**, and **3**, respectively. Crystal structure analysis and computational methods were used to elucidate general features of the underlying mechanism of thermal expansion for the series. The contributions of several factors are described, including host−guest compatibility, electrostatic effects, and steric effects. A tilting mechanism gives rise to the negative components of thermal expansion in **1** and **2** but is inhibited by the large molecular volume of the guest in **3**. In addition, the thermosalient effect was observed for **2**. To our knowledge this is the first example of thermosalience reported for an inclusion compound.

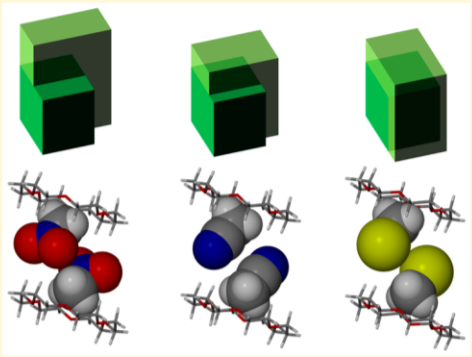

INTRODUCTION

When solids are heated, the thermal vibrations of their constituent atoms increase in magnitude and frequency. Macroscopically this is generally observed as moderate positive thermal expansion (PTE); i.e., unit cell axes (or principal axes in the case of nonorthogonal crystal systems) increase in length by relatively small and similar proportions in all three spatial dimensions. However, for some solids thermal expansion occurs anisotropically, that is, with highly disparate linear expansion coefficients along the three directions. Exceptionally large anisotropic PTE as well as negative thermal expansion (NTE) in organic compounds has been reported, but it is still considered rare.[1−4]

We recently reported on the thermal behavior of the nitromethane solvate of 18-crown-6, which undergoes large uniaxial NTE along one principal axis, with large PTE along the other two directions.[5] The result was of particular interest as the first observation of an organic inclusion compound where NTE occurs in the absence of appreciable directional interactions such as strong hydrogen bonds or coordination linkages. Other similar instances serve as evidence that large uniaxial NTE can occur in crystals composed of weakly bound constituents, driven by steric interactions and the sliding of layers.[6−8] However, elucidating the reasons why contraction occurs in some directions and not others requires a detailed investigation. We are also aware of evidence that fewer and weaker intermolecular interactions may give rise to greater coefficients of linear PTE.[9,10] However, a recent study concluded that, in a noncovalent network, hydrogen bonding dimensionality alone was not a reliable predictor of thermal expansion behavior.[11]

For quantitative comparison, the coefficient of linear thermal expansion for a solid is calculated as α_L in eq 1, where L_T is the axis length at a final temperature T and L_0 the axis length at an initial temperature T_0. Similarly, the coefficient of volumetric thermal expansion is given as α_v in eq 2.

$$\alpha_L = \frac{L_T - L_0}{L_0(T - T_0)} \quad (1)$$

$$\alpha_V = \frac{V_T - V_0}{V_0(T - T_0)} \quad (2)$$

Multiple studies have shown that guest replacement is a potential means of manipulating thermal expansion behavior in inorganic host−guest systems where the host is a coordination polymer.[12−16] Recently our group identified a Zn(II) metal−organic framework that was able to include short-chain alcohols.[17] Guest replacement was used to tune the α_L values along all three crystallographic axes and even change α_L from positive to negative in one instance. To the best of our knowledge a systematic study of the effect of guest replacement on thermal expansion has never been reported for a series of organic inclusion compounds or a host−guest system of any

Received: May 12, 2016
Revised: June 15, 2016
Published: June 24, 2016

DOI: 10.1021/acs.chemmater.6b01916
Chem. Mater. 2016, 28, 5073−5079

kind where only weak hydrogen bonds and van der Waals interactions exist.

The compounds described in the present study crystallize in the nonorthogonal monoclinic crystal system. The program PASCal was therefore used to determine an orthogonal set of principal axes and to calculate thermal expansion coefficients.[18]

Our previous investigation of the nitromethane solvate of 18-crown-6 revealed some of the underlying structural reasons why this particular compound exhibits large uniaxial negative thermal expansion.[5] We have now extended that study by exploring isoskeletal[19] analogues of the compound with different guest molecules—the present report describes a systematic and comparative study involving the nitromethane solvate ($C_{12}H_{24}O_6{\cdot}2CH_3NO_2$, **1**) as well as the solvates of acetonitrile ($C_{12}H_{24}O_6{\cdot}2CH_3CN$, **2**) and iodomethane ($C_{12}H_{24}O_6{\cdot}2CH_3I$, **3**). Bromomethane and chloromethane were considered as potential guests, but crystallization was not attempted because both are extremely hazardous gases at room temperature.

EXPERIMENTAL METHODS

Materials. 18-crown-6, nitromethane, and acetonitrile were purchased from Sigma-Aldrich. Iodomethane was obtained from Merck. All chemicals were used as received.

Synthesis. Compounds **1** and **2** were prepared by dissolving 18-crown-6 in a minimum amount of solvent (nitromethane and acetonitrile, respectively) and allowing slow evaporation at room temperature. In both cases colorless hexagonal plates were obtained. In the case of **3**, a concentrated solution of 18-crown-6 in iodomethane was kept at ~278 K, and slow evaporation yielded striated yellow plates.

X-ray Diffraction. In order to prevent guest loss during the collection of diffraction data, crystals of **1** and **2** were first coated with a thin layer of epoxy before being glued to a glass fiber. In the case of **3**, guest loss was very rapid, and this crystal was therefore attached to the mount using Paratone oil and then rapidly placed under the cold stream of the diffractometer.

Crystals of **1** and **3** were mounted on the diffractometer at 90 K. The crystal of **2** was mounted at 180 K because a phase transformation is known to occur below this temperature. The data for crystal **1** were collected as part of a previous study[5] at the following temperatures in the range 180−273 K: 180, 210, 240, 260, and 273 K. The data for **2** and **3** were collected in the range 180−273 K at 180, 200, 220, 240, 260, and 273 K. The data are considered sufficient for comparison by the linear regression method employed by PASCal (see Figure S10).

Single crystal X-ray diffraction data were collected using a Bruker APEX-II Quasar CCD area-detector diffractometer equipped with an Oxford Cryosystems 700Plus cryostat. A multilayer monochromator with Mo Kα radiation (λ = 0.71073 Å) from an Incoatec IμS microsource was used.

Data reduction was carried out by means of a standard procedure using the Bruker software package SAINT,[20] and absorption corrections and correction of other systematic errors were performed using SADABS.[21,22] The structures were solved by direct methods using SHELXS-97 and refined using SHELXL-97.[23] X-Seed[24] was used as the graphical interface for the SHELX program suite. Hydrogen atoms were placed in calculated positions using riding models.

Powder X-ray diffraction data were collected using a Bruker D2 PHASER equipped with Lynxeye 1D detector and Ni-filtered Cu Kα radiation (λ = 1.5418 Å; 30 kV, 10 mA generator parameters; restricted by a 1.0 mm divergence slit and a 2.5 Soller collimator). Compounds **1** and **2** were gently ground into powders using a mortar and pestle and loaded onto zero background holders. It was not possible to collect an experimental PXRD pattern for **3** because the compound is very unstable under ambient conditions.

Thermal Analysis. Thermogravimetric analysis (TGA) was carried out using a TA Instruments Q500 analyzer. Samples were loaded into aluminum sample pans and heated at 10 K min^{-1} from room temperature to decomposition.

Differential scanning calorimetry (DSC) experiments were carried out on a TA Instruments Q100 equipped with a Liquid Nitrogen Cooling Accessory (LNCS). All samples were cooled and heated at a rate of 10 K min^{-1}. A sample of compound **2** was cooled from 293 to 100 K and immediately thereafter heated to 293 K (Figure 1). Similarly, **1** was cooled from 273 to 123 K and heated back to 273 K (Figure S8). Compound **3** was cooled from 278 to 123 K and heated back to 278 K (Figure S9).

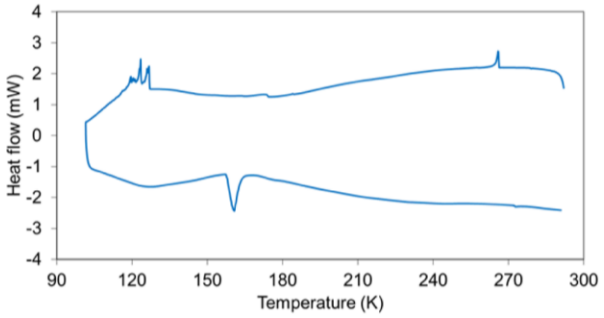

Figure 1. DSC trace for **2** where the temperature was ramped from 293 to 100 K and then back to 293 K.

A Linkam DSC600 temperature-controlled stage equipped with a digital video camera and LNP95 liquid nitrogen cooling pump was used to record temperature-dependent changes in the appearance of crystals of **2**. The stage was operated via a T95-System Controller. The temperature was ramped from 278 to 93 K and back to 278 K at a ramp rate of 20 K min^{-1}.

Computational Analysis. Atomic coordinates were imported from the refined crystal structures. Only the hydrogen atoms in the framework were optimized as part of a periodic system using the CASTEP module of the *Materials Studio* software suite.[25] The optimizations were performed using the GGA PBE functional with Grimme's DFT-D dispersion correction, and thresholds for geometry optimization and SCF convergence were chosen as 1×10^{-5} and 1×10^{-6} eV, respectively. Single point energy calculations using the DMol3 module of the Materials Studio software suite were performed using the GGA PBE functional with Grimme's DFT-D dispersion correction, and threshold for SCF convergence were chosen as 1×10^{-6} eV. The electron density data obtained from the DMol3 calculations were used to construct the three-dimensional 0.01 e$^-$ Å^{-3} electron density contour used for the molecular electrostatic potential map (obtained from the same calculation).

RESULTS AND DISCUSSION

We studied the thermal expansion behavior of **1**−**3** in temperature ranges devoid of polymorphic or guest-loss transformations. DSC of compounds **1** and **3** (see Figures S8 and S9) showed no indications of polymorphic transformations for these compounds in the temperature range of our thermal expansion study. The thermal events in Figure S8 correspond to melting and freezing of residual nitromethane. Since two polymorphs of **2** are known[26,27] we focused on the high temperature form $\mathbf{2_I}$ rather than the low temperature form $\mathbf{2_{II}}$. The DSC in Figure 1 reveals that upon cooling at 10 K min^{-1} the conversion from $\mathbf{2_I}$ to $\mathbf{2_{II}}$ occurs with an onset temperature of 127 K. Upon subsequent heating the transition back to form $\mathbf{2_I}$ occurs at 157 K, and the two forms are therefore a pair of enantiotropic polymorphs.

The cooling exotherm has a sawtooth profile, which is characteristic of the thermosalient effect.[28] To investigate this phenomenon further, a crystal of form $\mathbf{2_I}$ was cooled using a

DOI: 10.1021/acs.chemmater.6b01916
Chem. Mater. 2016, 28, 5073−5079

temperature-controlled stage equipped with a digital video camera. Preliminary experiments confirmed the existence of a thermosalient phase transformation and also revealed that the thermosalient event is more pronounced at higher rates of cooling. When cooled at 20 K min^{-1} extensive cracking of the crystal occurred at the phase transition onset temperature, and soon thereafter, in the range 115−100 K, the crystal exploded (see images in Figure 2 and video in the Supporting Information). This experiment was also carried out with a powdered sample of form $\mathbf{2}_\mathrm{I}$, and a similar effect was observed where the particles jumped and shifted in the sample pan when cooled below 110 K. We note that thermosalience of **2** is consistent with the following statement by Naumov and co-workers: "... the thermosalient effect can be expected for first-order phase transitions in soft crystals devoid of an extended 3-D hydrogen-bonding network that undergo strongly anisotropic thermal expansion around the phase transition."[28] To the best of our knowledge, this is the first report of an inclusion compound exhibiting the thermosalient effect.

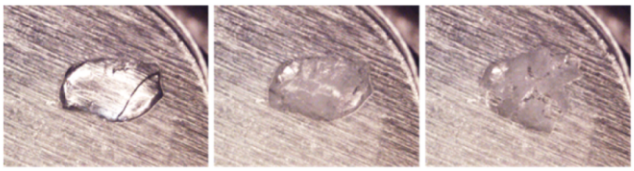

Figure 2. Thermal stage microscopy still images of a crystal of **2** at three stages of cooling from 278 to 93 K.

Single-crystal X-ray diffraction data were recorded at regular intervals for **1**−**3** in the temperature range 180−273 K. In all cases the sample was mounted at low temperature and heated at 240 K min^{-1} between data collections. Tables of crystallographic data are available in the ESI. The three compounds are isoskeletal,[19] crystallizing with similar host packing arrangements in the space group $P2_1/n$. The guest molecules form dimers, located between successive host molecules, stacked along the b axis. In **2** the guest molecule is disordered over two positions with an occupancy of ∼60% for its major component.

The coefficients of linear thermal expansion for the three compounds, determined using PASCal, are provided in Table 1.

Table 1. Coefficients of thermal expansion for 1-3 over the range 180-273 K. The values are given in ppm per Kelvin ($\times 10^{-6}$ K^{-1})

	α_{X1}	α_{X2}	α_{X3}	α_V
1	−198(12)	215(16)	369(20)	378(22)
2	−42(3)	103(4)	162.8(6)	226(3)
3	104(4)	−1(1)	153(5)	256(8)

Although PASCal uses a linear regression approach over the temperature range supplied, the axial response for compounds **1**−**3** with temperature is not strictly linear. However, the linear approximation is adequate for an in-depth rationalization of the mechanism of thermal expansion.

For both **1** and **2** thermal expansion is negative along one axis and positive along the other two axes, although the magnitudes are much lower for **2**. Compound **3**, on the other hand, experiences relatively large PTE along two principal axes and effectively zero thermal expansion along the third axis. Compounds **2** and **3** have similar coefficients of PTE along X3.

The volumetric thermal expansion coefficients for all three materials are exceptionally large for organic inclusion compounds. Compound **1** has the largest linear and volumetric thermal expansion coefficients of the three solvates studied. The linear coefficients along X1 follow the trend **1** < **2** < 0 < **3**. Taking the difference in minimum and maximum expansion coefficients as a measure of anisotropy,[11] the anisotropy also decreases in the order **1** > **2** > **3**.

Although solvates **1**−**3** are isoskeletal, their β angles vary (at 180 K β_1 = 100.907(2)°, β_2 = 105.108(1)°, and β_3 = 107.142(3)°), and the directions of the principal axes with respect to the unit cell axes are quite different in each case (see Figure 3). The precise directions of the principal orthogonal axes for **1** are X1 [0.9830 0 0.1835], X2 [0.1347 0 0.9909], and X3 [0 1 0]; for **2** are X1 [0.9970 0 0.0770], X2 [0.4736 0 0.8807], and X3 [0 1 0]; and for **3** are X1 [0.9529 0 0.3031], X2 [0.3639 0 0.9314], and X3 [0 1 0]. These directions are arbitrarily assigned positive indices. There is no distinction between the positive and the negative directions of principal axes.

In **1**, X1 and X2 have large components along [100] and [001], respectively. For **2**, X1 is mostly along [100] and X2 is approximately along [102]. The approximate directions of X1 and X2 are [301] and [103], respectively, in **3**. Again these directions are arbitrarily assigned positive indices.

For each compound visual inspection of the thermal ellipsoids (Figure 4) of the host atoms at high temperature indicates that the host vibrates mostly in the X1/X2 plane. Thermal ellipsoids of the host atoms are greatly elongated in the X1/X2 plane with smaller components along X3. Thus, it appears that it is mainly the increase in guest thermal motion that gives rise to large expansion along X3. Visual comparison of thermal displacement ellipsoids of the three different guest molecules shows a trend in degree of elongation (NO_2 > CN > I) in the direction of X3 that is somewhat consistent with the trend of **1** ≫ **2** ≈ **3** for PTE along X3. In particular, it seems that heating amplifies the vibration of the nitro group about the C−N bond.

Furthermore, it appears that the host ellipsoids of **2** are more anisotropic at low temperature as compared to those of **1** and **3**, and we attribute this to poor host−guest and host−host fitting. We hypothesize that there is a lower degree of packing efficiency in **2** as compared with **1** and **3**. The acetonitrile guest occupies less space within the host cavity than do the nitromethane and iodomethane guests, which allows for greater freedom of movement and larger amplitudes of thermal displacement. The nitrile group of acetonitrile is much smaller than the nitro group of nitromethane, and guest vibrations thus cause less PTE along X3 in **2** than they do in **1**.

The ellipsoid of the iodine atom of **3** is relatively undistorted, presumably because of better host−guest fitting in **3** relative to **1** and **2**. Although its thermal vibrations are small, iodine is relatively large and heavy (mean van der Waals radii: r_I = 1.98 Å, r_C = 1.70 Å, r_N = 1.55 Å, r_O = 1.52 Å).[29] Therefore, even the small vibrations apparent here are sufficient to give rise to PTE along X3 that is almost equal to that of **2**. We believe that the same size effect prevents negative thermal expansion in the X1/X2 plane and our rationalization follows later in this report.

In our previous study of **1** it was noted that its anisotropic thermal expansion is facilitated by relatively weak electrostatic interactions.[5] Dipole−dipole stabilization occurs between adjacent guest nitromethane molecules while host−guest CH···O hydrogen bonds connect the molecules in columns

DOI: 10.1021/acs.chemmater.6b01916
Chem. Mater. 2016, 28, 5073−5079

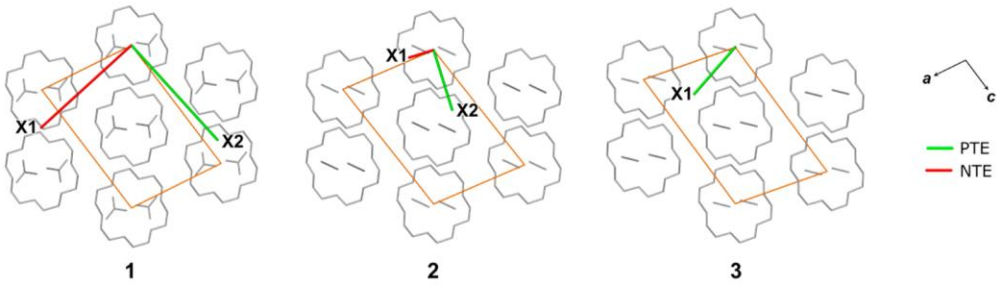

Figure 3. Orthogonal principal axes of thermal expansion in the *ac* plane, indicating positive (green) and negative (red) linear coefficients of thermal expansion. The lengths of the principal axes are proportional to the corresponding magnitudes of thermal expansion. The projected unit cell axes are shown as orange lines.

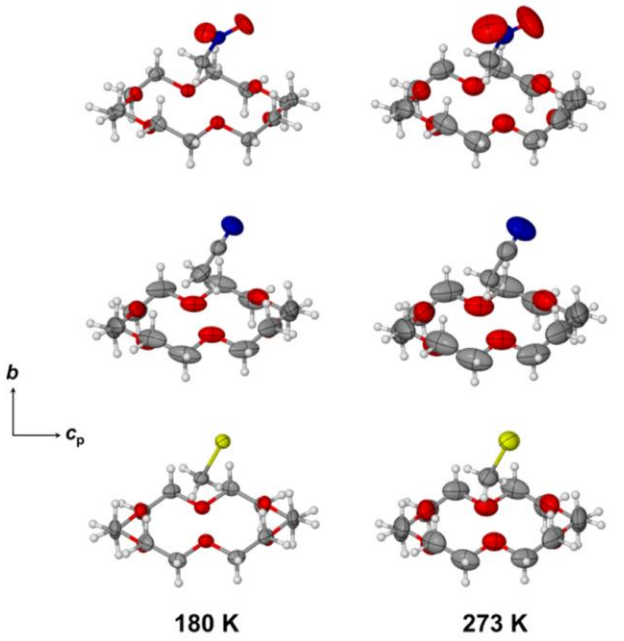

Figure 4. Thermal ellipsoid plots of **1**–**3** at 180 and 273 K, all viewed along [100]. For **2** only the major component of the disordered guest is shown.

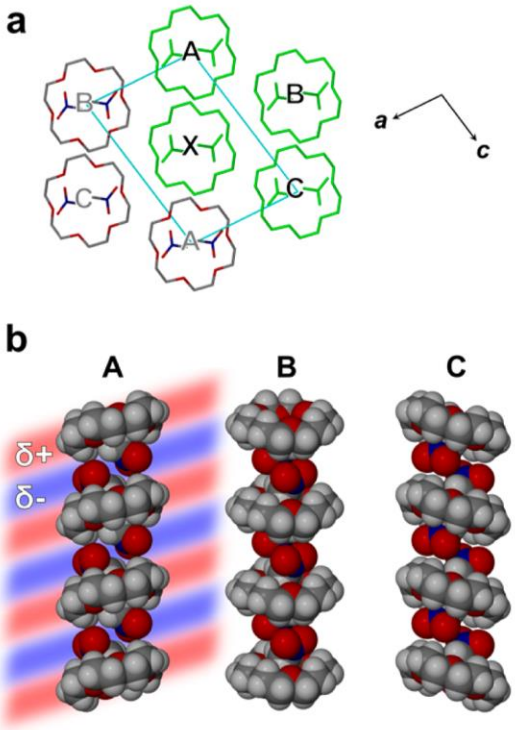

Figure 5. (a) Projection of **1** along [010]. The molecules displayed in green represent the computational model used for VAMP electrostatics calculations. The model extends along [010] by four unit cells. Similar computational models were used for **2** and **3**. (b) Columns A, B, and C of the computational model used for **1**, viewed along the directions [$\bar{1}0\bar{1}$], [$\bar{1}00$], and [$\bar{1}01$], respectively. Red and blue bands represent $\delta+$ and $\delta-$ regions of the column, respectively.

parallel to the crystallographic *b* axis. Electrostatic interactions between these columns give rise to uniaxial contraction as the crystal is heated.

Similar column constructions were applied to **2** and **3** with a view to deducing the underlying mechanisms giving rise to the observed patterns of anisotropic thermal expansion for the three structures. We used VAMP electrostatics calculations to probe all unique column–column interactions. The columns used for the computational model, for which a representative example is shown in Figure 5a, are labeled A, B, C, and X. This model allows for investigation of the three unique column–column interactions in the system: A···X, B···X, and C···X. Figure 5b shows the columns A, B, and C as viewed along [$\bar{1}0\bar{1}$], [$\bar{1}00$], and [$\bar{1}01$], respectively, and represented as space-filled models. The red bands indicate regions of partial positive charge, while blue bands denote regions of partial negative charge.

Figure 6 shows the column–column interactions of the three structures where the electrostatic potential of column X was mapped onto electron density isosurfaces of columns A, B, and C.[5,30] Red and blue indicate regions of positive and negative electrostatic potential, respectively.

Note that for **1**, the regions of strongest positive potentials for the interaction A···X (Figure 6) correspond with areas of partial negative charge on column A (Figure 5b), while the strongest negative potentials exist near areas of partial positive charge. The dominant interactions are clearly stabilizing. Similarly, for all electrostatic potential maps represented in Figure 6, the regions of highest positive and negative potential are associated with stabilizing interactions.

Adjacent columns are interdigitated, allowing for host–guest side-on interactions. There is potential for these side-on interactions to be enhanced by the shortening of intermolecular distances, particularly between columns B and X. In **1**, the perpendicular distances between columns are d_{A-X} = 7.51, d_{B-X} = 9.27, and d_{C-X} = 8.97 Å. Sufficient space and concerted motion (see video in Supporting Information) allows for the

DOI: 10.1021/acs.chemmater.6b01916
Chem. Mater. 2016, 28, 5073–5079

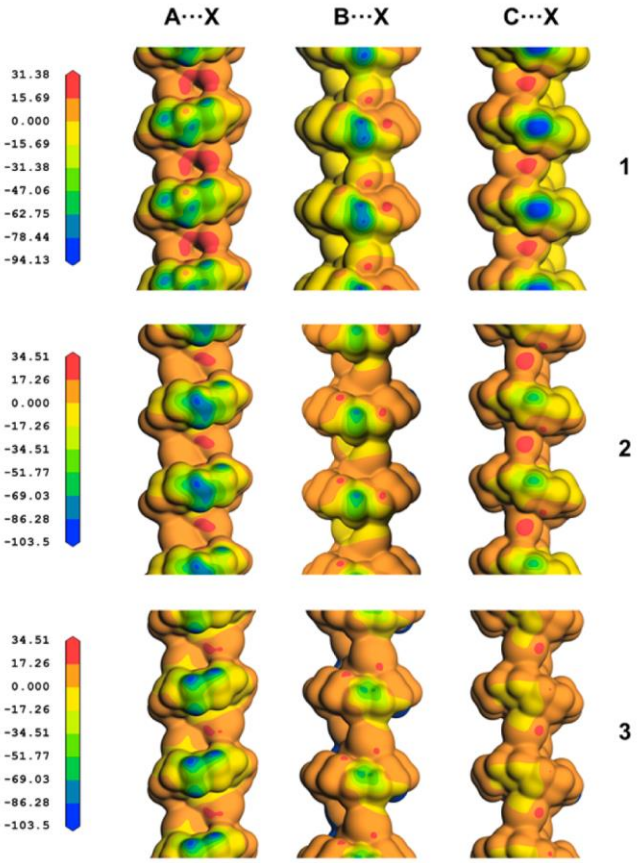

Figure 6. Electrostratic potential of column X was mapped onto electron density isosurfaces of A, B, and C to characterize the three unique interactions A···X, B···X, and C···X. Electrostatic potential values are given in kcal mol^{-1}. Areas of strong positive and negative potential are indicated in red and blue, respectively.

adjacent host atoms of B and X to move closer together, increasing the degree of interdigitation and thus enhancing the B···X interaction and contributing to large NTE along X1.

In the case of **2** there is similar shortening of the B–X distance, contributing to NTE along X1. A···X experiences the strongest of the three column–column interactions in **2** and, accordingly, the A–X distance is relatively short. Increasing thermal vibrations induce expansion of the A–X distance, which in turn contributes to the PTE along X2.

For **3** the A···X interactions between columns are dominant. With increasing temperature the relative positions of columns A and X are largely preserved but the B···X and C···X interactions are easily overcome. The iodine atoms of X are directed toward columns B and C, and increasing the thermal vibrational displacement of these atoms forces columns B and C outward, thus enlarging the distances B–X and C–X to produce large PTE along X1.

Figure 7 shows an exaggerated scheme of how tilting facilitates contraction of the principal axis X1 while X2 might either become larger or remain unchanged. In **1** the host atoms tilt readily, contributing substantially to the large uniaxial NTE observed. In **2** this tilting is less pronounced, resulting in lower NTE.

For NTE to occur in the X1/X2 plane in the absence of tilting, the columns need to shift closer together. Owing to its size, the iodomethane guest limits host tilting to an angle of 1.09° and prevents adjacent columns in **3** from moving closer

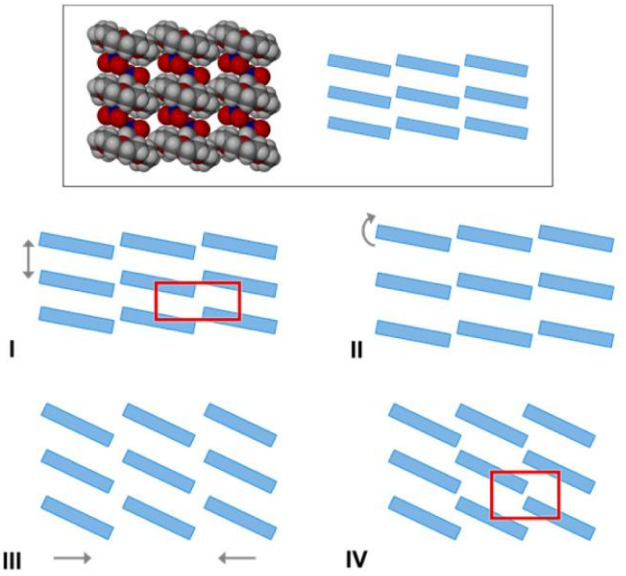

Figure 7. Schematic representation, projected in the X1/X3 plane, of the mechanism of thermal expansion. The rectangles represent host molecules viewed edge-on. Tilting of the hosts and expansion in the vertical direction (corresponding to X3) allows contraction in the horizontal direction (corresponding to X1).

together with increasing temperature. Consequently, **3** is the only structure that displays no uniaxial NTE.

In **2** the large thermal vibrations and disorder of the guest over two positions are evidence of poor host–guest fitting. This very poor fit, along with the relatively small size of acetonitrile as compared with nitromethane, means that an increase in kinetic volume of the guest in **2** results in PTE along X3 that is much smaller than in **1**. In turn, the reduction in PTE along X3 results in less NTE along X1.

■ CONCLUSIONS

We have described a systematic approach to the investigation of anisotropic thermal expansion by studying an isoskeletal series of inclusion compounds. This follows from our previous report[17] that guest replacement is a potential strategy for modifying the thermal expansion behavior of a metal–organic framework, which we have now extended to include organic inclusion compounds. Factors such as host–guest compatibility, electrostatics, and sterics must be considered as an ensemble in order to explain the pattern observed for **1**–**3**. In this particular series the existence of side-on host–host and host–guest interactions makes the underlying mechanism of anisotropic expansion very complex. It appears that for a similar organic series where weak interactions dominate and where side-on interactions are prevalent, it would be difficult to predict the influence of guest replacement on thermal expansion behavior. A useful approach for future studies would be to focus on systems where host–guest interactions are isolated within a cavity or channel, i.e., where the guest is included in a way that precludes side-on host–host and host–guest interactions. In this regard it would be worthwhile to investigate typical clathrate compounds that show anisotropic thermal expansion and form isoskeletal series with different guests.

DOI: 10.1021/acs.chemmater.6b01916
Chem. Mater. 2016, 28, 5073–5079

■ ASSOCIATED CONTENT

Supporting Information

The Supporting Information is available free of charge on the ACS Publications website at DOI: 10.1021/acs.chemmater.6b01916.

Crystallographic tables, PXRD patterns, TGA and DSC traces, and PASCal calculation details (PDF)

Crystallographic Information files in CIF format (ZIP)

Video showing thermosalient behavior of **2** as a single-crystal (MPG)

Video showing thermosalient behavior of **2** as a powder (MPG)

Video showing concerted motion of columns in **1** (MPG)

■ AUTHOR INFORMATION

Corresponding Author

*(L.J.B.) E-mail: ljb@sun.ac.za.

Author Contributions

The manuscript was written through contributions of all authors.

Funding

We are grateful to the SARChI Programme of the Department of Science and Technology and the National Research Foundation (South Africa) for financial support.

Notes

The authors declare no competing financial interest.

CCDC depository numbers 984226−984230, 984232, 1450339−1450344, and 1450438−1450444 contain the supplementary crystallographic data for this paper. These data can be obtained free of charge from the Cambridge Crystallographic Data Centre via www.ccdc.cam.ac.uk/data_request/cif.

■ ACKNOWLEDGMENTS

We thank the Centre for High Performance Computing (CHPC) in Cape Town for the use of their resources.

■ REFERENCES

(1) Zakrzewski, M.; White, M. A.; Abriel, W. Influence of Guest Molecular Species on the Thermal Expansion of Clathrates of Dianin's Compound and Concomitant Anharmonic Interactions. *J. Phys. Chem.* **1990**, *94*, 2203−2206.

(2) Birkedal, H.; Schwarzenbach, D.; Pattison, P. Observation of Uniaxial Negative Thermal Expansion in an Organic Crystal. *Angew. Chem., Int. Ed.* **2002**, *41*, 754−7546.

(3) Jones, R. H.; Knight, K. S.; Marshall, W. G.; Clews, J.; Darton, R. J.; Pyatt, D.; Coles, S. J.; Horton, P. N. Colossal Thermal Expansion and Negative Thermal Expansion in Simple Halogen Bonded Complexes. *CrystEngComm* **2014**, *16*, 237−243.

(4) Das, D.; Jacobs, T.; Barbour, L. J. Exceptionally Large Positive and Negative Anisotropic Thermal Expansion of an Organic Crystalline Material. *Nat. Mater.* **2010**, *9*, 36−39.

(5) Engel, E. R.; Smith, V. J.; Bezuidenhout, C. X.; Barbour, L. J. Uniaxial Negative Thermal Expansion Facilitated by Weak Host−guest Interactions. *Chem. Commun.* **2014**, *50*, 4238−4241.

(6) Loughrey, J. J.; Comyn, T. P.; Apperley, D. C.; Little, M. A.; Halcrow, M. A. Complex Thermal Expansion Properties in a Molecular Honeycomb Lattice. *Chem. Commun.* **2014**, *50*, 7601−7603.

(7) Bhattacharya, S.; Saha, B. K. Uniaxial Negative Thermal Expansion in an Organic Complex Caused by Sliding of Layers. *Cryst. Growth Des.* **2012**, *12*, 4716−4719.

(8) Bhattacharya, S.; Saha, B. K. Steric Guided Anomalous Thermal Expansion in a Dimorphic Organic System. *CrystEngComm* **2014**, *16*, 2340−2343.

(9) Kitaigorodsky, A. I. Molecular Crystals and Molecules. In *Physical Chemistry Series No. 29*; Loebl, E. M., Ed.; Academic Press: New York, 1973.

(10) Saraswatula, V. G.; Bhattacharya, S.; Saha, B. K. Can the Thermal Expansion Be Controlled by Varying the Hydrogen Bond Dimensionality in Polymorphs? *New J. Chem.* **2015**, *39*, 3345−3348.

(11) Bhattacharya, S.; Saraswatula, V. G.; Saha, B. K. Does Higher-Dimensional Hydrogen Bonding Guarantee a Smaller Thermal Expansion? A Thermal Expansion Study of an Interdigitated 1D and Interpenetrated 3D Hydrogen-Bonded Colored Dimorphic System. *Cryst. Growth Des.* **2016**, *16*, 277−284.

(12) Phillips, A. E.; Goodwin, A. L.; Halder, G. J.; Southon, P. D.; Kepert, C. J. Nanoporosity and Exceptional Negative Thermal Expansion in Single-Network Cadmium Cyanide. *Angew. Chem., Int. Ed.* **2008**, *47*, 1396−1399.

(13) Wei, Y.-S.; Chen, K.-J.; Liao, P.-Q.; Zhu, B.-Y.; Lin, R.-B.; Zhou, H.-L.; Wang, B.-Y.; Xue, W.; Zhang, J.-P.; Chen, X.-M. Turning on the Flexibility of Isoreticular Porous Coordination Frameworks for Drastically Tunable Framework Breathing and Thermal Expansion. *Chem. Sci.* **2013**, *4*, 1539−1546.

(14) Chapman, K. W.; Chupas, P. J.; Kepert, C. J. Compositional Dependence of Negative Thermal Expansion in the Prussian Blue Analogues $M^{II}Pt^{IV}(CN)_6$ (M = Mn, Fe, Co, Ni, Cu, Zn, Cd). *J. Am. Chem. Soc.* **2006**, *128*, 7009−7014.

(15) Zhou, H.-L.; Lin, R.-B.; He, C.-T.; Zhang, Y.-B.; Feng, N.; Wang, Q.; Deng, F.; Zhang, J.-P.; Chen, X.-M. Direct Visualization of a Guest-Triggered Crystal Deformation Based on a Flexible Ultramicroporous Framework. *Nat. Commun.* **2013**, *4*, 2534.

(16) Zhou, H.-L.; Zhang, Y.-B.; Zhang, J.-P.; Chen, X.-M. Supramolecular-Jack-like Guest in Ultramicroporous Crystal for Exceptional Thermal Expansion Behaviour. *Nat. Commun.* **2015**, *6*, 6917.

(17) Grobler, I.; Smith, V. J.; Bhatt, P. M.; Herbert, S. A.; Barbour, L. J. Tunable Anisotropic Thermal Expansion of a Porous Zinc(II) Metal-Organic Framework. *J. Am. Chem. Soc.* **2013**, *135*, 6411−6414.

(18) Cliffe, M. J.; Goodwin, A. L. PASCal: A Principal-Axis Strain Calculator for Thermal Expansion and Compressibility Determination. *J. Appl. Crystallogr.* **2012**, *45*, 1321−1329.

(19) Lloyd, G. O.; Alen, J.; Bredenkamp, M. W.; de Vries, E. J. C.; Esterhuysen, C.; Barbour, L. J. Solid-State Self-Inclusion: The Missing Link. *Angew. Chem., Int. Ed.* **2006**, *45*, 5354−5358.

(20) *SAINT Data Reduction Software*, Version 6.45; Bruker AXS Inc.: Madison, WI, 2003.

(21) *SADABS*, Version 2.05; Bruker AXS Inc.: Madison, WI, 2002.

(22) Blessing, R. H. An Empirical Correction for Absorption Anisotropy. *Acta Crystallogr., Sect. A: Found. Crystallogr.* **1995**, *51*, 33−38.

(23) Sheldrick, G. M. A Short History of SHELX. *Acta Crystallogr., Sect. A: Found. Crystallogr.* **2008**, *64*, 112−122.

(24) Barbour, L. X-Seed − A Software Tool for Supramolecular Crystallography. *J. Supramol. Chem.* **2001**, *1*, 189−191.

(25) *Materials Studio Modeling Environment*, Version 6.0.0; Accelrys Software Inc.: San Diego, 2011.

(26) Rogers, R. D.; Richards, P. D.; Voss, E. J. Neutral Solvent/Crown Ether Interactions, 4. Crystallization and Low Temperature (−150°C) Structural Characterization of 18-crown-6·2(CH3CN). *J. Inclusion Phenom.* **1988**, *6*, 65−71.

(27) Garrell, R. L.; Smyth, J. C.; Fronczek, F. R.; Gandour, R. D. Crystal Structure of the 2:1 Acetonitrile Complex of 18-Crown-6. *J. Inclusion Phenom.* **1988**, *6*, 73−78.

(28) Panda, M. K.; Runcevski, T.; Husain, A.; Dinnebier, R. E.; Naumov, P. Perpetually Self-Propelling Chiral Single Crystals. *J. Am. Chem. Soc.* **2015**, *137*, 1895−1902.

(29) Bondi, A. van der Waals Volumes and Radii. *J. Phys. Chem.* **1964**, *68*, 441−451.

(30) Bezuidenhout, C. X.; Smith, V. J.; Bhatt, P. M.; Esterhuysen, C.; Barbour, L. J. Extreme Carbon Dioxide Sorption Hysteresis in Open-Channel Rigid Metal-Organic Frameworks. *Angew. Chem., Int. Ed.* **2015**, *54*, 2079−2083.

DOI: 10.1021/acs.chemmater.6b01916
Chem. Mater. 2016, 28, 5073−5079

4.2 Supporting information

Thermoresponsive organic inclusion compounds: modification of thermal expansion behavior by simple guest replacement

Emile R. Engel, Vincent J. Smith, Charl X. Bezuidenhout and Leonard J. Barbour*

Crystallographic details

Identification code	**1** (180K)	**1** (210K)	**1** (240K)	**1** (260K)
Empirical formula	$C_{14}H_{30}N_2O_{10}$	$C_{14}H_{30}N_2O_{10}$	$C_{14}H_{30}N_2O_{10}$	$C_{14}H_{30}N_2O_{10}$
Formula weight	386.40	386.40	386.40	386.40
Temperature / K	180(2)	210(2)	240(2)	260(2)
Crystal system	monoclinic	monoclinic	monoclinic	monoclinic
Space group	$P2_1/n$	$P2_1/n$	$P2_1/n$	$P2_1/n$
a / Å	9.2668(13)	9.2363(13)	9.1902(15)	9.1488(15)
b / Å	7.9623(11)	8.0254(11)	8.1108(13)	8.1812(13)
c / Å	13.7151(19)	13.7678(19)	13.853(2)	13.928(2)
α / °	90.00	90.00	90.00	90.00
β / °	100.907(2)	101.054(2)	101.313(2)	101.529(2)
γ / °	90.00	90.00	90.00	90.00
Volume / $Å^3$	993.7(2)	1001.6(2)	1012.6(3)	1021.4(3)
Z	2	2	2	2
ρ_{calc} / g cm^3	1.291	1.281	1.267	1.256
μ/mm^{-1}	0.109	0.109	0.107	0.107
F(000)	416.0	416.0	416.0	416.0
Crystal size/mm^3	0.4 × 0.36 × 0.27	0.4 × 0.36 × 0.27	0.4 × 0.36 × 0.27	0.4 × 0.36 × 0.27
Radiation	MoKα (λ = 0.71073)	MoKα (λ = 0.71073)	MoKα (λ = 0.71073)	MoKα (λ = 0.71073)
2Θ range for data collection/°	4.9 to 56.58	4.9 to 56.58	4.9 to 56.58	4.92 to 56.64
Index ranges	-12 ≤ h ≤ 12, -10 ≤ k ≤ 10, -18	-12 ≤ h ≤ 12, -10 ≤ k ≤ 10, -18	-12 ≤ h ≤ 12, -10 ≤ k ≤ 10, -18	-12 ≤ h ≤ 12, -10 ≤ k ≤ 10, -18
Reflections collected	14545	14646	14825	14870
Independent reflections	2464 [R_{int} = 0.0241, R_{sigma} = 0.0159]	2477 [R_{int} = 0.0246, R_{sigma} = 0.0162]	2509 [R_{int} = 0.0265, R_{sigma} = 0.0176]	2530 [R_{int} = 0.0281, R_{sigma} = 0.0194]
Data/restraints/parameters	2464/0/119	2477/0/119	2509/0/119	2530/0/119
Goodness-of-fit on F^2	1.085	1.067	1.113	1.084
Final R indexes [I>=2σ (I)]	R1 = 0.0406, wR2 = 0.1031	R1 = 0.0472, wR2 = 0.1224	R1 = 0.0604, wR2 = 0.1757	R1 = 0.0737, wR2 = 0.2245
Final R indexes [all data]	R1 = 0.0492, wR2 = 0.1087	R1 = 0.0602, wR2 = 0.1311	R1 = 0.0821, wR2 = 0.1930	R1 = 0.1167, wR2 = 0.2926
Largest diff. peak/hole / e $Å^{-3}$	0.30/-0.23	0.37/-0.28	0.39/-0.33	0.47/-0.34

Crystallographic details

Identification code	**1** (273K)	**2** (180K)	**2** (200K)	**2** (220K)
Empirical formula	$C_{14}H_{30}N_2O_{10}$	$C_{16}H_{30}N_2O_6$	$C_{16}H_{30}N_2O_6$	$C_{16}H_{30}N_2O_6$
Formula weight	386.40	346.42	346.42	346.42
Temperature/K	273(2)	180(2)	200(2)	220(2)
Crystal system	monoclinic	monoclinic	monoclinic	monoclinic
Space group	$P2_1/n$	$P2_1/n$	$P2_1/n$	$P2_1/n$
a/Å	9.1231(14)	9.1653(2)	9.16200(10)	9.15390(10)
b/Å	8.2311(13)	8.3545(2)	8.38190(10)	8.40910(10)
c/Å	13.982(2)	13.5416(3)	13.5583(2)	13.5804(2)
α/°	90.00	90.00	90.00	90.00
β/°	101.676(2)	105.1080(10)	105.0530(10)	104.9870(10)
γ/°	90.00	90.00	90.00	90.00
Volume/Å^3	1028.2(3)	1001.06(4)	1005.48(2)	1009.81(2)
Z	2	2	2	2
ρ_{calc}g/cm^3	1.248	1.149	1.144	1.139
μ/mm^{-1}	0.106	0.087	0.087	0.087
F(000)	416.0	376.0	376.0	376.0
Crystal size/mm^3	0.4 × 0.36 × 0.27	0.3 × 0.2 × 0.2	0.3 × 0.2 × 0.2	0.3 × 0.2 × 0.2
Radiation	MoKα (λ = 0.71073)	MoKα (λ = 0.71073)	MoKα (λ = 0.71073)	MoKα (λ = 0.71073)
2Θ range for data collection/°	4.92 to 56.68	4.84 to 56.62	4.84 to 56.68	4.84 to 56.66
Index ranges	-11 ≤ h ≤ 11, -10 ≤ k ≤ 10, -18	-12 ≤ h ≤ 12, -11 ≤ k ≤ 11, -18	-12 ≤ h ≤ 12, -11 ≤ k ≤ 11, -18	-12 ≤ h ≤ 12, -11 ≤ k ≤ 11, -18
Reflections collected	15176	26618	26929	27076
Independent reflections	2542 [R_{int} = 0.0282, R_{sigma} = 0.0196]	2489 [R_{int} = 0.0263, R_{sigma} = 0.0124]	2511 [R_{int} = 0.0239, R_{sigma} = 0.0111]	2517 [R_{int} = 0.0248, R_{sigma} = 0.0115]
Data/restraints/parameters	2542/0/120	2489/0/139	2511/0/139	2517/0/139
Goodness-of-fit on F^2	1.047	1.095	1.092	1.086
Final R indexes [I>=2σ (I)]	R1 = 0.0823, wR2 = 0.2599	R1 = 0.0639, wR2 = 0.1752	R1 = 0.0559, wR2 = 0.1615	R1 = 0.0557, wR2 = 0.1644
Final R indexes [all data]	R1 = 0.1167, wR2 = 0.2926	R1 = 0.0778, wR2 = 0.1847	R1 = 0.0703, wR2 = 0.1727	R1 = 0.0749, wR2 = 0.1783
Largest diff. peak/hole / e Å^{-3}	0.47/-0.34	0.16/-0.23	0.14/-0.18	0.14/-0.17

Crystallographic details

Identification code	**2** (240K)	**2** (260K)	**2** (273K)	**3** (180K)
Empirical formula	$C_{16}H_{30}N_2O_6$	$C_{16}H_{30}N_2O_6$	$C_{16}H_{30}N_2O_6$	$C_{14}H_{30}I_2O_6$
Formula weight	346.42	346.42	346.42	548.18
Temperature/K	240(2)	260(2)	273(2)	180.15
Crystal system	monoclinic	monoclinic	monoclinic	monoclinic
Space group	$P2_1/n$	$P2_1/n$	$P2_1/n$	$P2_1/n$
a/Å	9.14650(10)	9.13780(10)	9.1309(2)	9.0082(6)
b/Å	8.43580(10)	8.46360(10)	8.48250(10)	8.5752(5)
c/Å	13.6024(2)	13.6287(2)	13.6493(2)	14.2853(8)
α/°	90.00	90.00	90.00	90.00
β/°	104.9150(10)	104.8400(10)	104.7760(10)	107.142(3)
γ/°	90.00	90.00	90.00	90.00
Volume/Å^3	1014.17(2)	1018.87(2)	1022.22(3)	1054.48(11)
Z	2	2	2	2
ρ_{calc}g/cm^3	1.134	1.129	1.125	1.726
μ/mm^{-1}	0.086	0.086	0.085	3.003
F(000)	376.0	376.0	376.0	536.0
Crystal size/mm^3	0.3 × 0.2 × 0.2	0.3 × 0.2 × 0.2	0.3 × 0.2 × 0.2	0.15 × 0.15 × 0.05
Radiation	MoKα (λ = 0.71073)	MoKα (λ = 0.71073)	MoKα (λ = 0.71073)	MoKα (λ = 0.71073)
2Θ range for data collection/°	4.84 to 56.64	4.86 to 56.6	4.86 to 56.66	4.8 to 56.58
Index ranges	-12 ≤ h ≤ 12, -11 ≤ k ≤ 11, -18	-12 ≤ h ≤ 12, -11 ≤ k ≤ 11, -18	-12 ≤ h ≤ 12, -11 ≤ k ≤ 11, -18	-7 ≤ h ≤ 11, -11 ≤ k ≤ 8, -19 ≤ l
Reflections collected	27189	27352	27448	8388
Independent reflections	2525 [R_{int} = 0.0257, R_{sigma} = 0.0116]	2532 [R_{int} = 0.0252, R_{sigma} = 0.0117]	2540 [R_{int} = 0.0270, R_{sigma} = 0.0117]	2612 [R_{int} = 0.0190, R_{sigma} = 0.0189]
Data/restraints/parameters	2525/0/139	2532/0/139	2540/0/139	2612/0/101
Goodness-of-fit on F^2	1.095	1.093	1.071	1.030
Final R indexes [I>=2σ (I)]	R1 = 0.0552, wR2 = 0.1670	R1 = 0.0561, wR2 = 0.1752	R1 = 0.0579, wR2 = 0.1714	R1 = 0.0221, wR2 = 0.0489
Final R indexes [all data]	R1 = 0.0779, wR2 = 0.1839	R1 = 0.0829, wR2 = 0.1947	R1 = 0.0844, wR2 = 0.1915	R1 = 0.0252, wR2 = 0.0505
Largest diff. peak/hole / e Å^{-3}	0.12/-0.16	0.13/-0.15	0.11/-0.15	0.93/-0.89

Crystallographic details

Identification code	**3** (200K)	**3** (220K)	**3** (240K)	**3** (260K)
Empirical formula	C14H30I2O6	C14H30I2O6	$C_{14}H_{30}NO_6I_2$	$C_{14}H_{30}I_2O_6$
Formula weight	548.18	548.18	548.18	548.18
Temperature/K	200(2)	220(2)	240.15	260(2)
Crystal system	monoclinic	monoclinic	monoclinic	monoclinic
Space group	$P2_1/n$	$P2_1/n$	$P2_1/n$	$P2_1/n$
a/Å	9.0205(6)	9.0319(5)	9.0471(4)	9.0605(3)
b/Å	8.5963(4)	8.6191(4)	8.6470(3)	8.6754(2)
c/Å	14.2881(8)	14.2860(7)	14.2901(5)	14.2921(5)
α/°	90.00	90.00	90.00	90.00
β/°	107.101(3)	107.033(2)	106.938(2)	106.832(2)
γ/°	90.00	90.00	90.00	90.00
Volume/Å^3	1058.96(10)	1063.34(9)	1069.42(7)	1075.28(6)
Z	2	2	2	2
ρ_{calc}g/cm^3	1.719	1.712	1.702	1.693
μ/mm^{-1}	2.991	2.978	2.961	2.945
F(000)	536.0	536.0	536.0	536.0
Crystal size/mm^3	0.15 × 0.15 × 0.05	0.15 × 0.15 × 0.05	0.15 × 0.15 × 0.05	0.15 × 0.15 × 0.05
Radiation	MoKα (λ = 0.71073)	MoKα (λ = 0.71073)	MoKα (λ = 0.71073)	MoKα (λ = 0.71073)
2Θ range for data collection/°	4.78 to 56.56	4.78 to 56.6	4.78 to 56.62	4.78 to 56.62
Index ranges	-7 ≤ h ≤ 11, -11 ≤ k ≤ 8, -19 ≤ l	-7 ≤ h ≤ 11, -11 ≤ k ≤ 8, -19 ≤ l	-7 ≤ h ≤ 12, -11 ≤ k ≤ 8, -19 ≤ l	-7 ≤ h ≤ 12, -11 ≤ k ≤ 8, -19 ≤ l
Reflections collected	8433	8466	8537	8589
Independent reflections	2621 [R_{int} = 0.0197, R_{sigma} = 0.0187]	2638 [R_{int} = 0.0190, R_{sigma} = 0.0192]	2651 [R_{int} = 0.0190, R_{sigma} = 0.0193]	2666 [R_{int} = 0.0182, R_{sigma} = 0.0188]
Data/restraints/parameters	2621/0/101	2638/0/101	2651/0/101	2666/0/101
Goodness-of-fit on F^2	1.036	1.024	1.032	1.022
Final R indexes [I>=2σ (I)]	R1 = 0.0245, wR2 = 0.0550	R1 = 0.0272, wR2 = 0.0591	R1 = 0.0308, wR2 = 0.0692	R1 = 0.0334, wR2 = 0.0750
Final R indexes [all data]	R1 = 0.0292, wR2 = 0.0574	R1 = 0.0331, wR2 = 0.0622	R1 = 0.0386, wR2 = 0.0733	R1 = 0.0452, wR2 = 0.0814
Largest diff. peak/hole / e Å^{-3}	1.07/-0.96	1.05/-0.95	1.09/-0.97	1.05/-0.90

Crystallographic details

Identification code	**3** (273K)
Empirical formula	$C_{14}H_{30}I_2O_6$
Formula weight	548.18
Temperature/K	273(2)
Crystal system	monoclinic
Space group	$P2_1/n$
a/Å	9.0683(3)
b/Å	8.6955(2)
c/Å	14.2945(5)
α/°	90.00
β/°	106.751(2)
γ/°	90.00
Volume/Å^3	1079.34(6)
Z	2
ρ_{calc}g/cm^3	1.687
μ/mm^{-1}	2.934
F(000)	536.0
Crystal size/mm^3	0.15 × 0.15 × 0.05
Radiation	MoKα (λ = 0.71073)
2Θ range for data collection/°	4.78 to 56.66
Index ranges	-7 ≤ h ≤ 12, -11 ≤ k ≤ 8, -19 ≤
Reflections collected	8613
Independent reflections	2679 [R_{int} = 0.0194, R_{sigma} = 0.0197]
Data/restraints/parameters	2679/0/101
Goodness-of-fit on F^2	1.028
Final R indexes [I>=2σ (I)]	R1 = 0.0354, wR2 = 0.0795
Final R indexes [all data]	R1 = 0.0514, wR2 = 0.0879
Largest diff. peak/hole / e Å^{-3}	1.02/-0.82

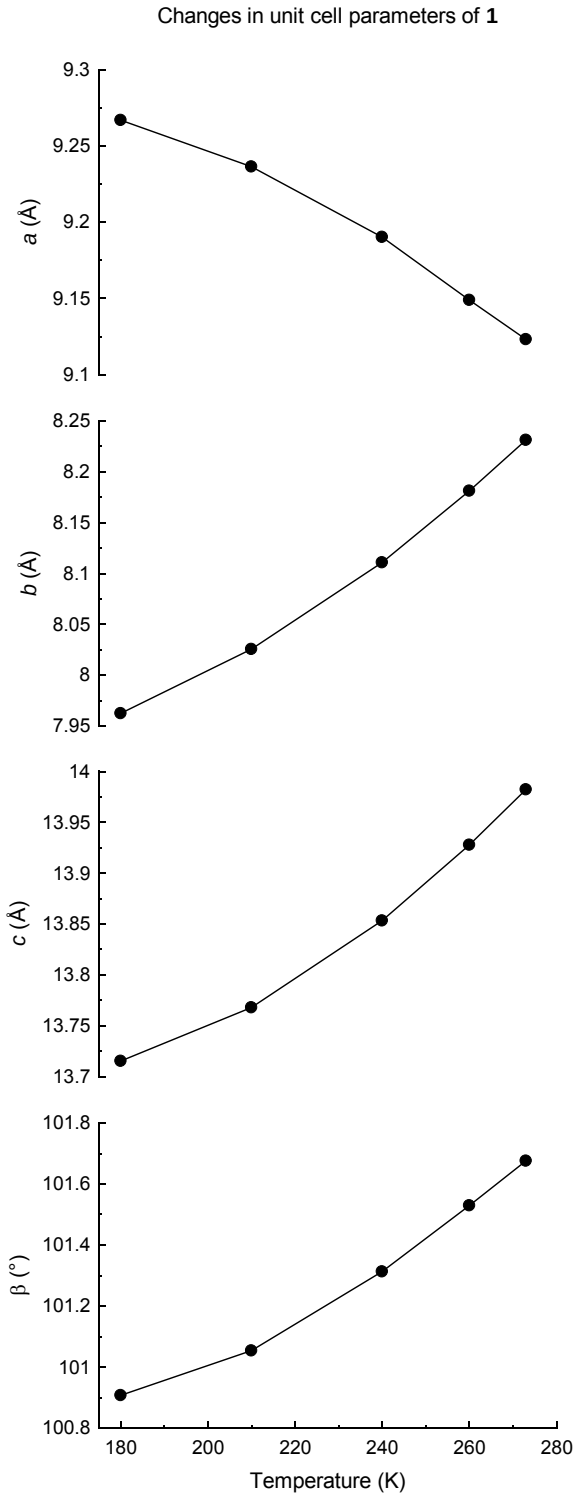

Figure S1. Unit cell parameters of **1** as a function of temperature.

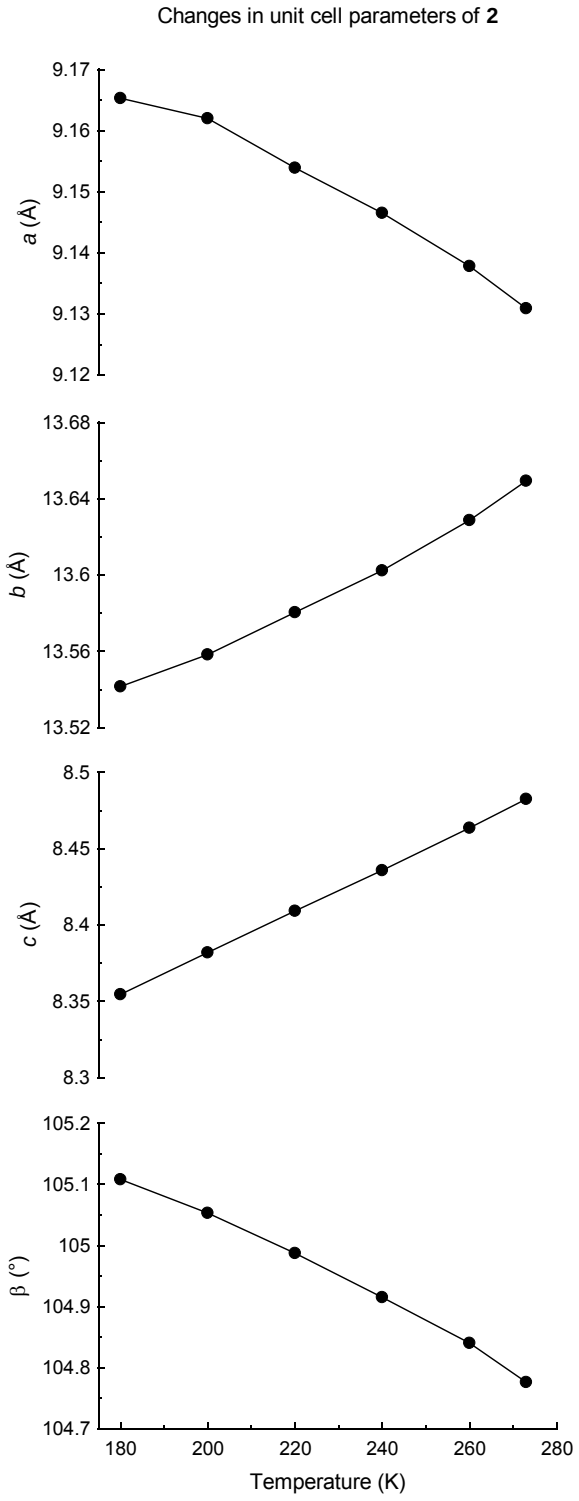

Figure S2. Unit cell parameters of **2** as a function of temperature.

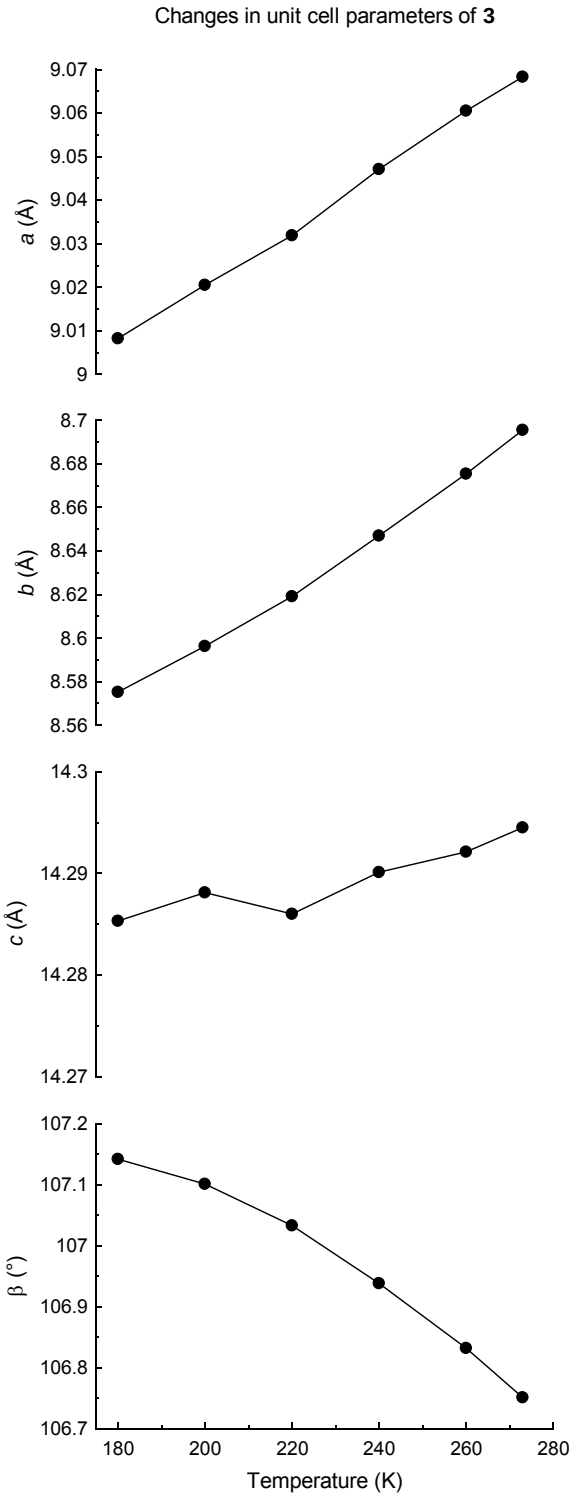

Figure S3. Unit cell parameters of **3** as a function of temperature.

Powder X-ray Diffraction

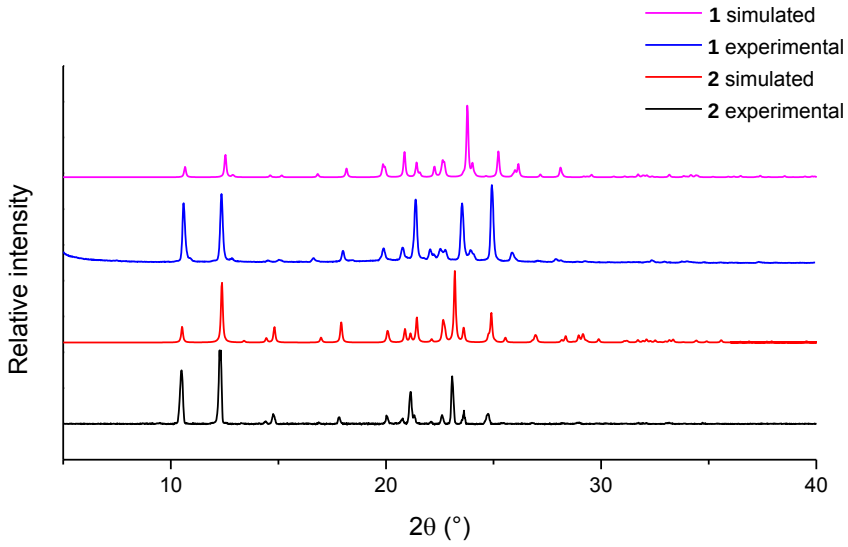

Figure S4. Comparison of the experimental and calculated PXRD patterns of **1** and **2**. It was not possible to collect an experimental PXRD pattern for **3** because the compound is very unstable under ambient conditions.

Thermogravimetric analysis

For compound **1** the experimental solvent mass loss is 31.38 %c while the calculated solvent mass loss is 31.60 % (Figure S5).

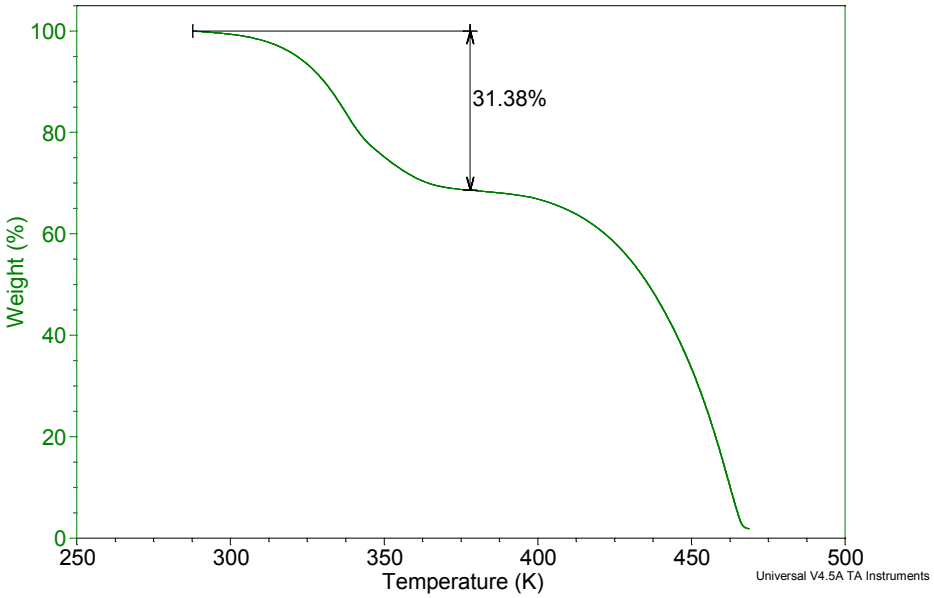

Figure S5. TGA trace for **1** heated at 10 K min^{-1} from room temperature to 473 K.

For compound **2** the experimental solvent mass loss is 22.15 % and the calculated solvent mass loss 23.70 % (Figure S6).

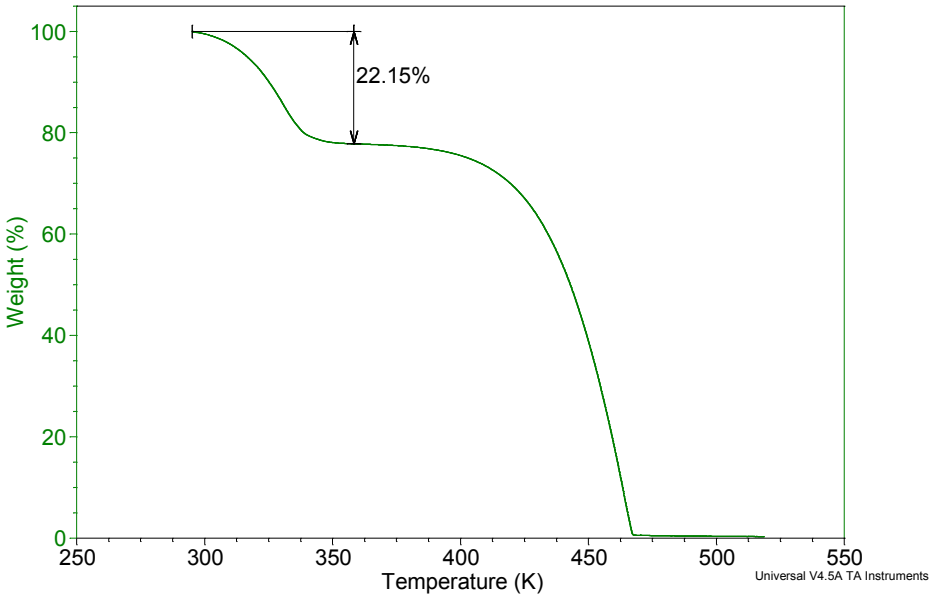

Figure S6. TGA trace for **2** heated at 10 K min^{-1} from room temperature to 473 K.

For compound **3** the calculated solvent mass loss is 51.78 % while the experimental solvent mass loss is 46.29 % (Figure S7).

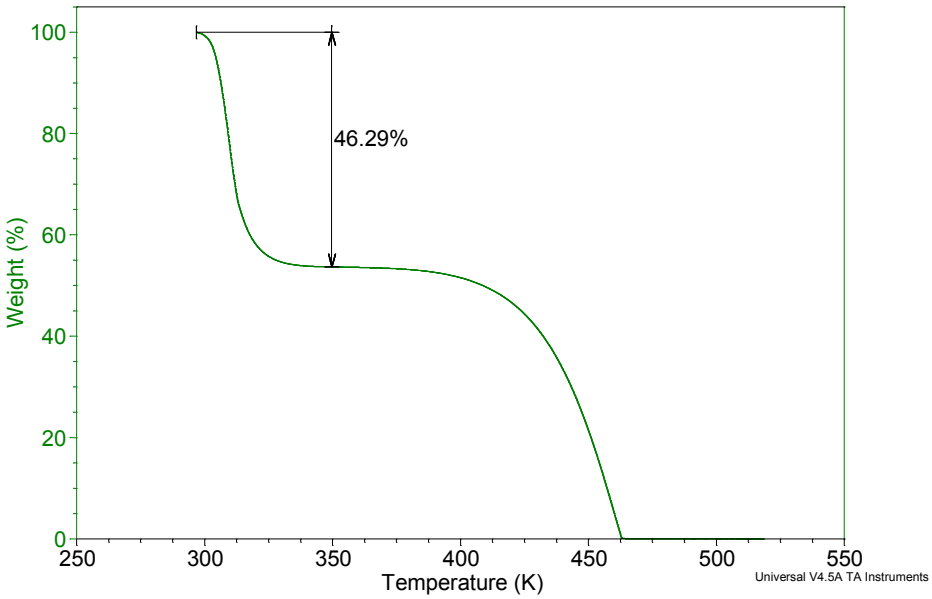

Figure S7. TGA trace for **3** heated at 10 K min^{-1} from room temperature to 473 K.

Differential scanning calorimetry

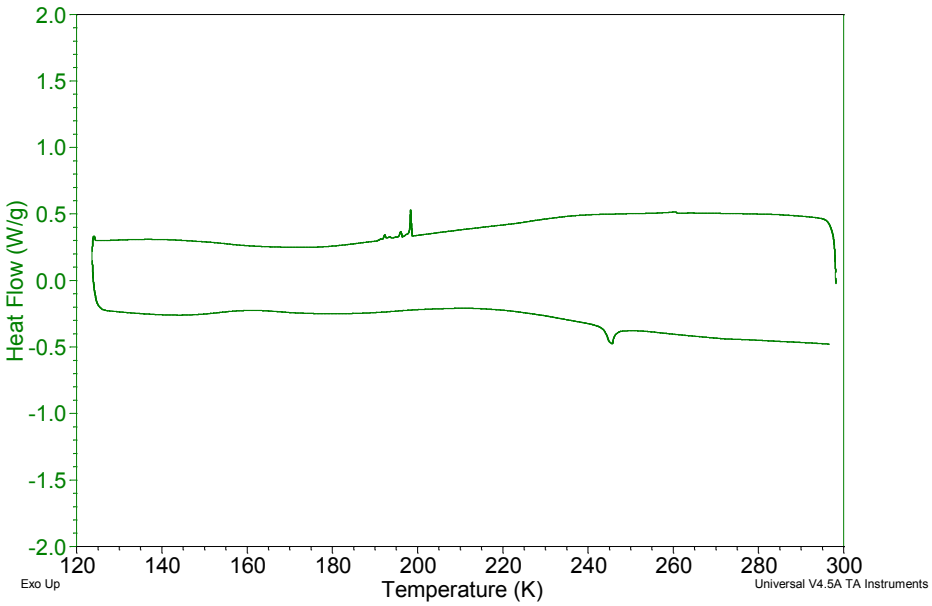

Figure S8. DSC trace for **1** where the temperature was ramped from 273 to 123 K and heated to back to 273 K.

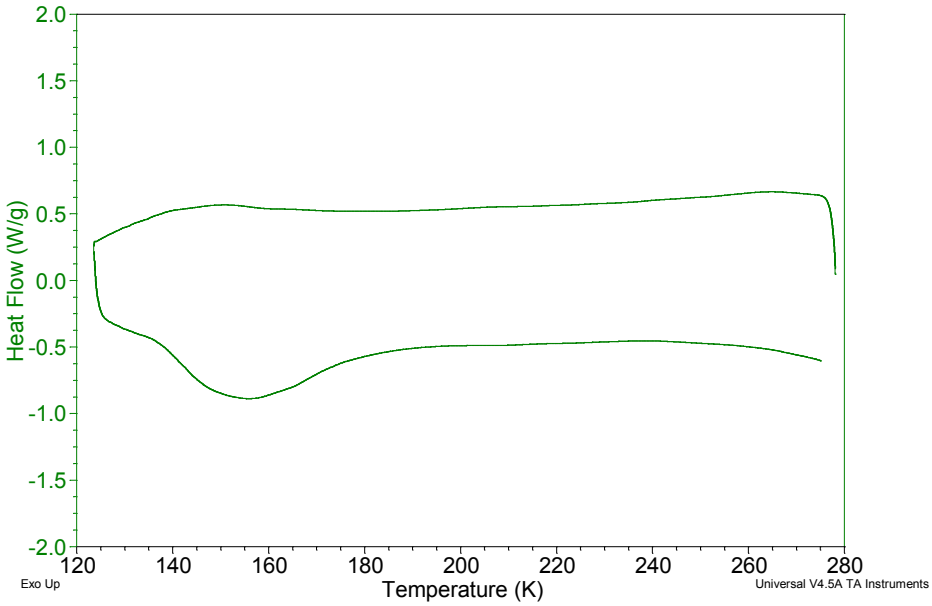

Figure S9. DSC trace for **3** where the temperature was ramped from 278 to 123 K and heated back to 278 K.

PASCal

PASCal calculations were carried out online at http://pascal.chem.ox.ac.uk using the Eulerian Finite strain setting.

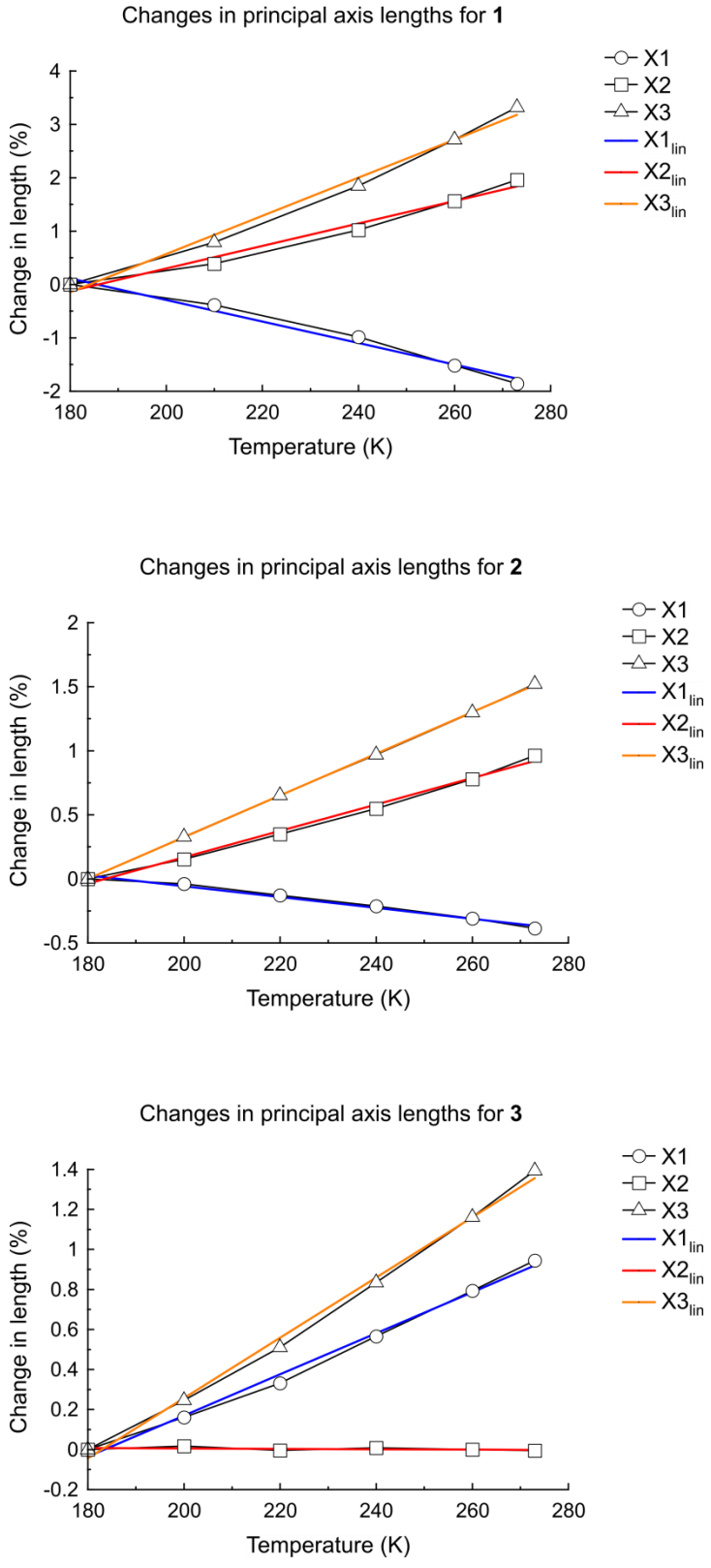

Figure S10. Changes in principal axis lengths as a function of temperature.

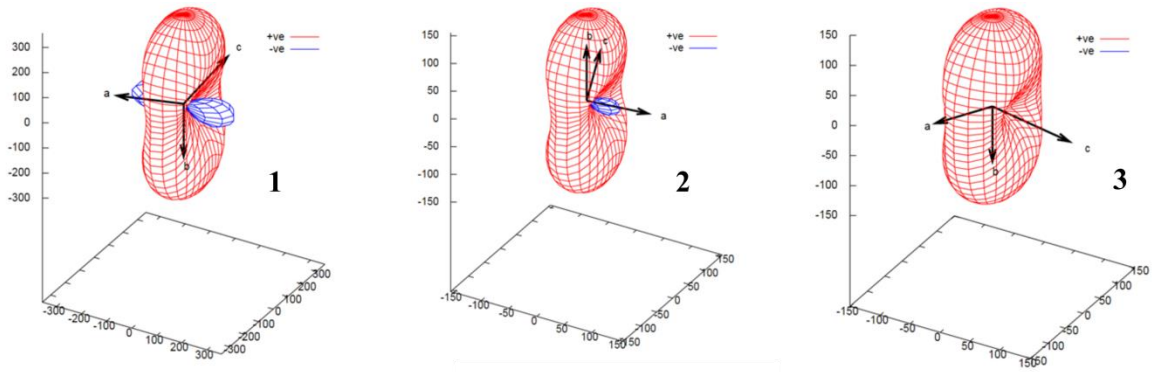

Figure S11. Expansivity indicatrices generated using PASCal.

Chapter 5

Activation-dependent breathing in a flexible metal-organic framework and the effects of repeated sorption/desorption cycling

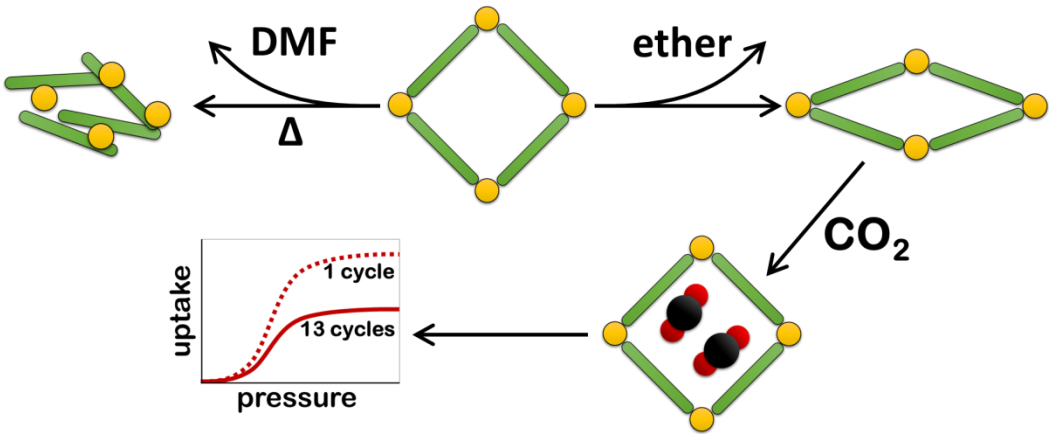

5.1 Communication (manuscript under review)

Contributions of the author:

- Design of project with Dr Abdelaziz Jouaiti
- Ligand synthesis with Dr Abdelaziz Jouaiti
- Preparation of the MOF
- Solvent exchange and supercritical CO_2 experiments
- Collection of single-crystal X-ray diffraction data
- Solution and refinement of single-crystal X-ray structures
- Recording of standard and pressure-resolved PXRD patterns
- Recording of TGA thermograms
- Sorption analysis with Charl X. Bezuidenhout
- Interpretation of results with Charl X. Bezuidenhout

Activation-dependent breathing in a flexible metal-organic framework and the effects of repeated sorption/desorption cycling

Emile R. Engel,[†] Abdelaziz Jouaiti,[‡] Charl X. Bezuidenhout,[†] Mir Wais Hosseini,*[‡] and Leonard J. Barbour*[†]

[†]Department of Chemistry and Polymer Science, University of Stellenbosch, Matieland 7602, Stellenbosch, South Africa

[‡]Laboratoire de Chimie de Coordination Organique, UMR CNRS 7140, Université de Strasbourg, F-67000, Strasbourg, France

Supporting Information Placeholder

ABSTRACT: A non-interpenetrated MOF with a paddle-wheel SBU has been activated by direct thermal evacuation, guest exchange with a volatile solvent, and supercritical CO_2 drying. Conventional thermal activation results in a mixture of crystalline phases and some amorphous content. Exchange with a volatile solvent prior to vacuum activation produces a pure breathing phase with high sorption capacity, selectivity for CO_2 over N_2 and CH_4, and substantial hysteresis. Supercritical drying can be used to access a guest-free open phase. Pressure-resolved differential scanning calorimetry was used to investigate the systematic loss of sorption capacity by the breathing phase as a function of successive cycles of sorption and desorption.

During synthesis of a metal-organic framework (MOF) the reaction solvent is usually trapped as a guest within cavities or channels of the porous framework. These typically high-boiling guest molecules are routinely removed by heating under dynamic vacuum. However this form of direct activation often leads to irreversible framework changes that reduce porosity.[1] MOF crystals often maintain their single-crystal character during solvent exchange,[2] i.e. when the MOF is submerged in a new guest solvent, allowing for guest exchange by diffusion. Employing a relatively volatile solvent for exchange potentially lowers the activation temperature, thereby increasing the probability of obtaining high-quality single crystals of an activated phase. Similarly, activation methods such as supercritical drying[3] and freeze-drying[4] have been shown to affect MOF properties by improving surface areas and pore performance.

A recent study of activation effects on the three-dimensional Zn carboxylate MOF FIR-3 included solvent exchange, freeze drying and supercritical drying.[5] Large variations in the resulting sorption capacity were observed for these three methods. In a separate study Park and co-workers investigated the effect of activation methods on the fine structure of SNU-77, also a three-dimensional Zn carboxylate.[6] Yang *et al.* were also able to optimise the sorption capacity of Cu-BTC by solvent exchange with various solvents prior to activation.[7] In general, however, detailed *structural* investigations of the effect of solvent-mediated activation are limited.

Gas sorption studies have been used to evaluate MOFs in terms of their utility for gas capture and separation. Indeed, the separation of commercially important gas mixtures such as flue gas emissions,[8] natural gas[9] and short-chain alkanes[10] are of particular interest, as is the direct-air capture of carbon dioxide.[11]

Flexible MOFs, often described as having soft porosity,[12] generally interpenetrate and the prevention of interpenetration is sometimes advantageous for maximising potential guest-free volume.[13] A variety of strategies[14] have been employed with success, including the selection of sterically bulky ligands.[15] In the present study we have prepared an analogue of the known doubly-interpenetrated MOF-508,[10,16] but we have appended phenyl groups to the dicarboxylic acid bridging ligand in order to prevent interpenetration.

We synthesised 2,5-diphenylbenzene-1,4-dicarboxylic acid (DPT) according to a literature procedure.[17] The non-interpenetrated MOF **1** was prepared by combining DPT, 4,4′-bipyridine and zinc nitrate tetrahydrate in DMF, and incubating at 100 °C for 24 h (Scheme 1). The framework has molecular formula $[Zn_2(C_{20}H_{12}O_4)_2(C_{10}H_8N_2)]_n$ and its as-synthesised, solvated phase is referred to as **1A**.

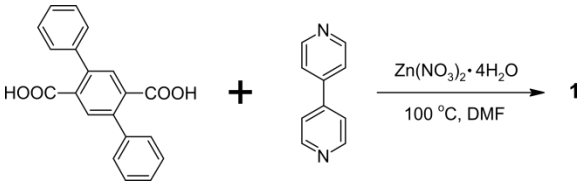

Scheme 1. Solvothermal synthesis of **1**.

Phase **1A** crystallizes in the space group *P*4/*ncc* and contains highly disordered DMF guest molecules, which could not be modelled (the residual electron density in the guest-accessible channels amounts to 1160 electrons per unit cell – see ESI). The pillared-layered structure of **1A** is based on

zinc paddle-wheel secondary building units and is analogous to that of MOF-508 but prevention of interpenetration greatly increases the potential free volume from 28% for MOF-508 (according to Hupp *et al.*[16a]) to 50.1% for **1A**. Both estimates were made using PLATON[18] (probe radius 1.2 Å). Figure S1 shows partial packing diagrams of **1A**, where phenyl substituents protrude into channels along [110] and [001].

Crystals of **1A** lose guest DMF (total percentage mass loss = 30.0%) in at least two steps according to thermogravimetric analysis (TGA) (Figure S2). A sample of **1A** was activated at 423 K under dynamic vacuum for 12 h but the resulting guest-free phase lost its single-crystal character. Powder X-ray diffraction (Figure S7) showed that the sample had transformed to what appeared to be a mixture of unknown phases and some amorphous content.

In an attempt to lower the temperature of activation, crystals of **1A** were submerged in diethyl ether for solvent exchange. The new solvent was replaced once a day for three days to ensure complete exchange of the included guest. The crystals showed minimal signs of cracking or other damage as a result of the exchange process and TGA (Figure S4) confirmed that all included guest is expelled below 330 K. Solvent-exchanged crystals were activated at ambient temperature under dynamic vacuum; some crystals had maintained their single-crystal character and it was therefore possible to record single-crystal diffraction data. The activated phase **1B** is an empty, collapsed version of **1A** (Figure 1) in which the connectivity of the MOF is preserved.

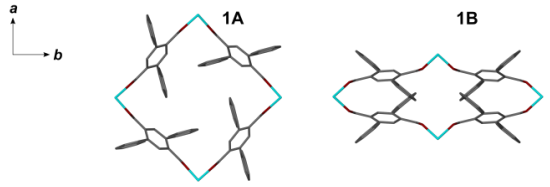

Figure 1. Perspective view along [001] showing the *open-channel* nature of **1A** (left) as compared to its *closed* counterpart **1B**. Hydrogen atoms and guest molecules have been omitted for clarity.

A sample of **1A** was similarly subjected to solvent exchange with ethyl acetate (TGA provided as Figure S5) and activated at 353 K under dynamic vacuum. Powder X-ray diffraction (PXRD, Figure S8) confirms that the same transformation to **1B** occurs for the samples activated *via* diethyl ether and ethyl acetate exchange, and that the single-crystal X-ray structure of **1B** is representative of the bulk. For further investigation, **1B** was routinely prepared by activation of **1A** *via* diethyl ether exchange.

It has been reported that treatment of a MOF with supercritical CO_2 can produce an activated phase of higher porosity than might be obtained by heating under dynamic vacuum.[3a] We treated **1A** with supercritical CO_2 for 48 h and PXRD (Figure S9) shows that the framework structure of the resultant activated phase resembles that of the as-synthesised version, **1A**.

Some of the crystals that had been subjected to the supercritical drying experiment were suitable for single-crystal X-ray diffraction. One of these was mounted in an environmental gas cell, which was then evacuated at ~2 x 10^{-3} mbar at room temperature for 12 h and thereafter sealed under these conditions. Single-crystal diffraction data were recorded at ambient temperature and, as expected, the structure resembles that of guest-free **1A** (we refer to this apohost form as **1C**; summation the residual electron density amounts to 18 electrons per unit cell – see ESI). In **1C** the phenyl rings of DPT are disordered over two positions, as are the pyridyl rings of the pillaring ligand, whereas in **1A** there is no crystallographic disorder. There is a related change in space group from $P4/ncc$ for **1A** to $P4$ for **1C**, and a change in the orientation and size of the unit cell. The disorder may be due to either the absence of guest molecules, the higher temperature of data collection (data for **1A** were collected at 173 K) or a combination of these factors. Nevertheless the connectivity and overall structure are preserved.

On multiple occasions samples of **1A** were dried under supercritical conditions. Although this produced phase pure **1C** in several instances, the experiment was not always reproducible. The method appears to be more reliable for smaller samples and we postulate that the presence of residual DMF interferes with this activation process (owing to the small volume of the supercritical fluid compartment of the apparatus). A phase-pure sample of **1C** from supercritical drying was analysed by FTIR, TGA and PXRDs. The FTIR spectrum (Figure S14) shows no evidence for entrapped CO_2, (i.e. no peak is observed at approximately 2300 cm^{-1}). However, the peak at 3430 cm^{-1} suggests that **1C** adsorbs water under ambient conditions, which is consistent with the TGA result for the same sample (Figure S6). A sample of **1C** was heated at 373 K under dynamic vacuum for 12 h, removed from the oven subjected to PXRD analysis under ambient conditions. This process was repeated for the same sample using temperatures of 423 K and then 523 K. From the resulting PXRD patterns (Figure S10) it is clear that the sample does not collapse or transform under these conditions.

Phase **1B** was exposed to supercritical CO_2 for 36 h, after which PXRD (Figure S11) indicated partial conversion to **1C**. A second, freshly activated sample of **1B** was also subjected to the same conditions for one week, after which the sample appeared to have almost entirely converted from **1B** to **1C**. However, most of the sample reverted to **1B** when subsequently evacuated at 523 K. Since this result is inconsistent with that for **1C** produced solely by supercritical drying, we propose that the conversion from **1B** to **1C** occurs *via* a metastable frustrated phase[19] that easily reverts to **1B**.

High pressure sorption analysis with N_2, CH_4 and CO_2 were carried out on a single sample of **1B** at 298

K. Informed by preliminary experiments, the order of gases was chosen to minimise carry-over effects. We tested N_2 first, then CH_4 and finally CO_2. It is clear from the sorption isotherms presented in Figure 2 that the compound has a far greater affinity for CO_2 over N_2 and CH_4.

We are presenting two cycles of CO_2 sorption. In the first cycle the sorption isotherm shows a broad gate-opening step beginning at ~25 bar. During the desorption leg of the first cycle most of the adsorbed CO_2 is retained down to a pressure of ~10 bar, below which it appears that gate closing occurs abruptly. In the second cycle, the gate-opening step is broader and begins at a lower pressure of ~20 bar. At 35 bar the sorption isotherm begins to resemble that of cycle 1. The desorption leg of cycle 2 also resembles that of cycle 1. The maximum uptake of CO_2 under the conditions used is 8.4 mmol g^{-1}, which is equivalent to 37 g of gas per 100 g of sorbent. In stark contrast the maximum uptakes of N_2 and CH_4 under the same conditions are a mere 0.081 and 0.23 mmol g^{-1}, respectively.

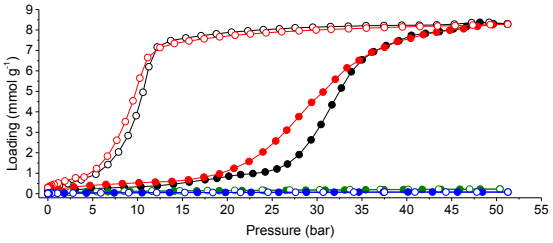

Figure 2. Sorption and desorption isotherms (shown with filled and empty circles, respectively) for **1** recorded at 298 K with test gases CO_2 (cycle 1 black, cycle 2 red), CH_4 (green) and N_2 (blue).

Variable-pressure PXRD (Figure S12) data were recorded with incremental CO_2 loading to further investigate the gate-opening event. A sample of **1B** was subjected to vacuum for the first data collection and then loaded with CO_2 in steps of 5 bar (all at ambient temperature). The structure remains unchanged over the pressure range 0-25 bar. However, between 25 and 30 bar there are clear changes in the PXRD pattern, indicating a phase transformation.

A comparison of the PXRD traces for **1B** under vacuum (Figure 3b) and of the same sample exposed *in situ* to 50 bar CO_2 (Figure 3d) shows that **1B** transforms, at least partially, to **1C** under CO_2 pressure. The gate-opening (or breathing)[20] event appears to be a transformation from **1B** to an open form that is a metastable frustrated variant of **1C**. The phase transformation to an open form is consistent with the definition of MOF breathing by Schneemann *et al*: "(reversible) transitions of metal-organic frameworks, during which the (substantial) displacement of atoms of the framework is accompanied by a change in unit cell volume ($\Delta V \neq 0$). Characteristic distances and angles of the unit cell change and the crystallographic space groups of the two distinct phases … may be different."[21] Reversibility is evident from the CO_2 sorption and desorption isotherms in Figure 2 as well as from the PXRD pattern (Figure S13) recorded after multiple sorption-desorption cycles.

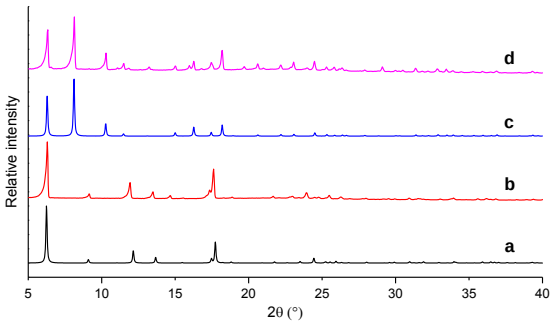

Figure 3. Comparison of (a) the calculated PXRD trace of **1B** from single-crystal diffraction data with (b) the experimental trace of a sample of **1B** under vacuum, (c) the calculated trace of **1C** and (d) the experimental trace recorded for the sample exposed *in situ* to 50 bar CO_2 pressure.

Figure S17 shows the CO_2 sorption isotherm for **1** together with those reported for MIL-53(Cr) hydrate[20a] and COMOC-2[20b] for qualitative comparison. The total sorption capacities for MIL-53(Cr) and **1** are comparable although **1** reaches equilibrium at higher pressure. In contrast to MIL-53(Cr), where selectivity of CO_2 over CH_4 is dependent on hydration of the framework,[20a] **1** shows comparatively high selectivity in its guest-free state. Both COMOC-2 and **1** retain CO2 over a remarkably large pressure range during desorption.

We used pressure-resolved differential scanning calorimetry (P-DSC) to investigate repeated cycling and its effect on the sorption capacity of **1**. We were thus able to obtain data for 13 sorption-desorption cycles over a period of 13 days, whereas the standard method of recording multiple sorption isotherms would have taken an estimated 50 days or more. The instrumental setup comprises a differential scanning calorimeter coupled to a gas syringe pump (details in ESI). The syringe pump is controlled by a computer programme to ensure delivery of a constant pressure gradient to the sample and reference chambers. The P-DSC output yields a thermogram of heat flow *vs* pressure (Figure S18) and from these data we derived plots of integral heat *vs* pressure for each sorption cycle (Figure S19). The first cycle is omitted for reasons described below. The integral heat is proportional to sorption loading and the profile of the integral heat *vs* pressure plot is thus a reliable approximation of expected sorption isotherms.

The maximum integral heat (proportional to the maximum sorption loading) was plotted against sorption-desorption cycle number to reveal systematic deterioration in sorption capacity with extended cycling (Figure 4). For all of the cycles, the gate-opening event occurs with an onset pressure of approximately 20 bar. However, the response to pressure, as evident from the sorption thermogram above this value, does not follow the same trend for

cycle 1 as for subsequent cycles (Figure S18). This implies that the first sorption experiment conditions the sample for subsequent gas inclusion – i.e. a 'memory' effect. Thus cycle 1 has been omitted from our analysis of the systematic decline in sorption capacity (Figure S19).

The fitted curve in Figure 4 tends to a final value of 61.92 J g^{-1} from an initial value of 160.35 J g^{-1} (details in ESI), implying that the sorption capacity of the material will ultimately be reduced to approximately 39% of its initial value.

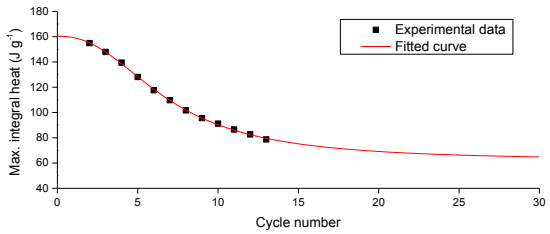

Figure 4. The maximum integral heat from pressure-DSC plotted against the cycle number of CO_2 sorption-desorption.

Although no appreciable loss of crystallinity was evident from PXRD analysis of **1** after 13 sorption/desorption cycles (Figure S13), subtle peak broadening occurs and we believe that partial sample degradation is responsible for the reduction in sorption capacity. Hupp and co-workers have described a robust paddle-wheel type MOF that maintains its sorption capacity through several sorption-desorption cycles.[22] They suggest that, in contrast, most MOFs that display dynamic sorption tend to lose uptake capacity because of extreme strain on coordination bonds, leading to bond breakage. However, we were not able to locate reported examples of this phenomenon for breathing MOFs. Kitagawa and co-workers described the effect of crystal downsizing, providing experimental to support the assertion that "reduction in the number of repeating units should be sufficient to regulate the cooperative nature of [structural transformations] and the effect of stress."[23] We postulate that the reduction in particle size in a sample of **1** with repeated fracturing of crystallites finally results in a particle size for which the stress induced by breathing is minimised. The mechanical degradation of particles of **1** is evident in the SEM images in Figure S20.

Direct activation of **1A** results in a loss of framework integrity, leaving **1** unusable for gas sorption. On the other hand, activation *via* solvent exchange not only preserves framework integrity but yields a collapsed phase **1B**, which exhibits gated breathing with relatively high uptake of CO_2. We have provided direct structural evidence of the difference between **1B** and **1C**, obtained by different activation methods. Our analysis of the effects of repeated CO_2 sorption-desorption cycling for **1** reveals a systematic decline in sorption capacity, suggesting that cycling effects may need to be investigated more routinely where MOFs, and particularly flexible MOFs, are proposed as industrial molecular storage and separation materials.

ASSOCIATED CONTENT

Supporting Information

Crystallographic information, PXRD patterns, TGA traces, NMR and FTIR spectra, and SEM images.

AUTHOR INFORMATION

Corresponding Authors

*ljb@sun.ac.za
*hosseini@unistra.fr

Notes

The authors declare no competing financial interest.

ACKNOWLEDGMENTS

ERE, CXB and LJB thank the SARChI Programme of the Department of Science and Technology, the National Research Foundation (South Africa) and the French Embassy in South Africa for financial support. AJ and MWH thank the University of Strasbourg, the CNRS, the International Centre for Frontier Research in Chemistry (icFRC), Strasbourg, the Labex CSC (ANR-10-LABX- 0026 CSC) within the Investissement d'Avenir program ANR-10-IDEX-0002-02 and the Institut Universitaire de France (IUF).

REFERENCES

(1) (a) Kitagawa, S.; Kitaura, R.; Noro, S. *Angew. Chem. Int. Ed.* **2004**, *43*, 2334. (b) Aggarwal, H.; Bhatt, P. M.; Bezuidenhout, C. X.; Barbour, L. J. *J. Am. Chem. Soc.* **2014**, *136*, 3776. (c) Mondloch, J. E.; Karagiaridi, O.; Farha, O. K.; Hupp, J. T. *CrystEngComm* **2013**, *15*, 9258.

(2) (a) Li, H.; Eddaoudi, M.; O'Keeffe, M.; Yaghi, O. M. *Nature* **1999**, *402*, 276. (b) Medishetty, R.; Jung, D.; Song, X.; Kim, D.; Lee, S. S.; Lah, M. S.; Vittal, J. J. *Inorg. Chem.* **2013**, 52, 2951.

(3) (a) Nelson, A. P.; Farha, O. K.; Mulfort, K. L.; Hupp, J. T. *J. Am. Chem. Soc.* **2009**, *131*, 458. (b) Gedrich, K.; Senkovska, I.; Klein, N.; Stoeck, U.; Henschel, A.; Lohe, M. R.; Baburin, I. a; Mueller, U.; Kaskel, S. *Angew. Chem. Int. Ed.* **2010**, *49*, 8489.

(4) Lohe, M. R.; Rose, M.; Kaskel, S. *Chem. Commun.*, 2009, 6056.

(5) He, Y.; Tan, Y.; Zhang, J. *Inorg. Chem.* **2012**, *51*, 11232.

(6) Park, H. J.; Lim, D.-W.; Yang, W. S.; Oh, T.-R.; Suh, M. P. *Chem. Eur. J.* **2011**, *17*, 7251.

(7) Yang, Y.; Shukla, P.; Wang, S.; Rudolph, V.; Chen, X.-M.; Zhu, Z. *RSC Adv.* **2013**, 3, 17065.

(8) Zhang, Z.; Zhao, Y.; Gong, Q.; Li, Z.; Li, J. *Chem. Commun.* **2013**, *49*, 653.

(9) (a) Yabing H.; Shengchang X.; Zhangjing Z.; Shunshun X.; Fronczek, F. R.; Krishna, R.; O'Keeffe, M.; Chen, B. *Chem. Commun.* **2012**, *48*, 10856. (b) Martín-Calvo, A.; García-Pérez, E.; Castillo, J. M.; Calero, S. *Phys. Chem. Chem. Phys.* **2008**, *10*, 7085.

(10) Chen, B.; Liang, C.; Yang, J.; Contreras, D. S.; Clancy, Y. L.; Lobkovsky, E. B.; Yaghi, O. M.; Dai, S. *Angew. Chem. Int. Ed.* **2006**, *45*, 1390.

(11) (a) Bhatt, P. M.; Belmabkhout, Y.; Cadiau, A.; Adil, K; Shekhah, O.; Shkurenko, A.; Barbour, L. J.; Eddaoudi, M. *J. Am. Chem. Soc.* **2016**. [Online early access]. DOI: 10.1021/jacs.6b05345. (b) Nugent, P.; Belmabkhout, Y.; Burd, S. D.; Cairns, A. J.; Luebke, R.; Forrest, K.; Pham, T.; Ma, S. Q.; Space, B.; Wojtas, L.; Eddaoudi, M.; Zaworotko, M. J. *Nature* **2013**, *495*, 80.

(12) Horike, S.; Shimomura, S.; Kitagawa. *Nat. Chem.* **2009**, *1*, 695.

(13) (a) James, S.L. *Chem. Soc. Rev.* **2003**, *32*, 276. (b) Jiang, H. L.; Makal, T. A.; Zhou, H. C. *Coord. Chem. Rev.* **2013**, *257*, 2232.

(14) (a) Eddaoudi, M.; Kim, J.; Rosi, N.; Vodak, D.; Wachter, J.; O'Keeffe, M.; Yaghi, O. M. *Science* **2002**, *295*, 469. (b) Shekhah, O.; Wang, H.; Paradinas, M.; Ocal, C.; Schupbach, B.; Terfort, A.; Zacher, D.; Fischer, R. A.; Woll, C. *Nat. Mater.* **2009**, *8*, 481. (c) Deshpande, R. K.; Waterhouse, G. I. N.; Jameson, G. B.; Telfer, S. G. *Chem. Commun.* **2012**, *48*, 1574.

(15) (a) Chun, H.; Dybtsev, N.; Kim, H.; Kim, K. *Chem.–Eur. J.*, **2005**, *11*, 3521. (b) Modrow, A.; Zargarani, D.; Herges, R.; Stock, N. *Dalton Trans.* **2011**, *40*, 4217.

(16) (a) Ma, B. Q.; Mulfort, K. L.; Hupp, J. T. *Inorg. Chem.* **2005**, *44*, 4912. (b) Chun, H.; Dybtsev, D. N.; Kim, H.; Kim, K. *Chem. Eur. J.* **2005**, *11*, 3521.

(17) Nakagawa, T.; Kumaki, D.; Nishida, J.; Tokito, S. *Chem. Mater.* **2008**, *20*, 2615.

(18) A.L.Spek, *Acta Crystallogr.* **2009**, *D65*, 148.

(19) Thallapally, P. K.; Dalgarno, S. J.; Atwood, J. L. *J. Am. Chem. Soc.*, **2006**, *128*, 15060.

(20) (a) Llewellyn, P. L.; Bourrelly, S.; Serre, C.; Filinchuk, Y.; Férey, G. *Angew. Chem. Int. Ed.* **2006**, *45*, 7751. (b) Wang, G.; Leus, K.; Couck, S.; Tack, P.; Depauw, H.; Liu, Y.-Y.; Vincze, L.; Denayer, J. F. M.; Van Der Voort, P. *Dalton Trans.* **2016**, *45*, 9485. (c) Salles, F.; Maurin, G.; Serre, C.; Llewellyn, P. L.; Knöfel, C.; Choi, H. J.; Filinchuk, Y.; Oliviero, L.; Vimont, A.; Long, J. R.; Férey, G. *J. Am. Chem. Soc.* **2010**, *132*, 13782.

(21) Schneemann, A.; Bon, V.; Schwedler, I.; Senkovska, I.; Kaskel, S.; Fischer, R. A. *Chem. Soc. Rev.* **2014**, *43*, 6062.

(22) Mulfort, K. L.; Farha, O. K.; Malliakas, C. D.; Kanatzidis, M. G.; Hupp, J. T. *Chem. Eur. J.* **2010**, *16*, 276.

(23) Sakata, Y.; Furukawa, S.; Kondo, M.; Hirai, K.; Horike, N.; Takashima, Y.; Uehara, H.; Louvain, N.; Meilikhov, M.; Tsuruoka, T.; Isoda, S.; Kosaka, W.; Sakata, O.; Kitagawa, S. *Science* **2013**, *339*, 193.

5.2 Supporting information

Activation-dependent breathing in a flexible metal-organic framework and the effects of repeated sorption/desorption cycling

Emile R. Engel, Abdelaziz Jouaiti, Charl X. Bezuidenhout, Mir Wais Hosseini,* Leonard J. Barbour*

Materials

All chemicals were purchased from Sigma Aldrich and used as received.

Synthesis

Synthesis of DPT

We synthesised 2,5-diphenylbenzene-1,4-dicarboxylic acid (DPT) according to a literature procedure[1] by coupling of phenyl boronic acid and 1,4-dibromo-2,5-dimethylbenzene to produce 1,4-diphenyl-2,5-dimethyl benzene. The 1,4-diphenyl-2,5-dimethyl benzene was purified by column chromatography and thereafter oxidised with potassium permanganate in pyridine to give the final product. (for ^{1}H NMR and ^{13}C NMR see Figure S15 and Figure S16).

Scheme S1. Synthesis of DPT.

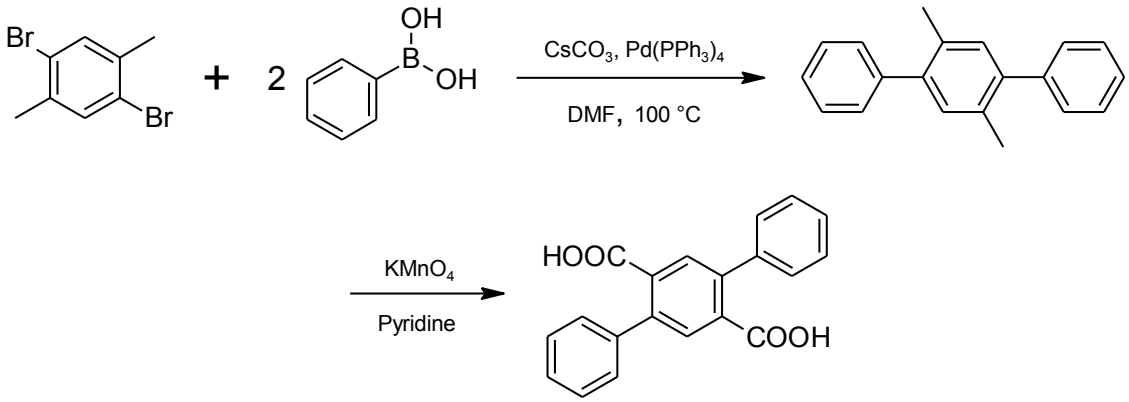

Solvothermal synthesis of **1**

The MOF **1** was prepared by combining 0.5 mmol (159.2 mg) of DPT, 0.25 mmol (39.0 mg) 4,4'-bipyridine and 0.5 mmol (130.7 mg) zinc nitrate tetrahydrate in 30 ml DMF and incubating at 100 °C. Small colourless rectangular blocks were harvested after 24 h. The as-synthesised version is referred to as **1A**.

Direct activation of **1A**

A sample of **1A** was evacuated at 423 K under dynamic vacuum for 12 h.

Preparation of **1B**

A sample of **1A** was soaked directly in 20 ml diethyl ether. The solvent was replaced 3 times over 3 days after which the sample was evacuated at room temperature for 12 h.

Preparation of **1C**

Approximately 10 mg of **1A** was activated using a Tousimis SAMDRI-PVT-3D advanced manual critical point drier. The sample was maintained under supercritical fluid CO_2 for 48 h before the chamber was slowly depressurised.

Single-crystal X-ray diffraction

Data for **1A** were collected using a Bruker D8 Venture equipped with a Photon II CPAD detector and an Oxford Cryosystems 800Plus cryostat, using graphite-monochromated Mo-Kα (λ = 0.71073 Å) radiation.

Data for **1B** and **1C** were collected using a Bruker APEX-II DUO diffractometer with CCD area-detector. The instrument employs a multilayer monochromator with MoKα radiation (λ = 0.71073 Å) from an Incoatec IμS microsource and is equipped with an Oxford Cryosystems 700Plus cryostat supplied with liquid N_2. For **1C** the crystal was mounted on a glass fibre inside an environmental gas cell. Prior to data collection the gas cell was evacuated at ~2×10^{-3} mbar for 12 h to remove any potential traces of guest molecules or adsorbed water vapour.

Data reduction was carried out by means of a standard procedure using the Bruker software package SAINT[2] and absorption corrections and correction of other systematic errors were performed using SADABS.[3] The structures were solved by direct methods using SHELXS-97 and refined using SHELXL-97.[4] X-Seed[5] was used as the graphical interface for the SHELX program suite. Hydrogen atoms were placed in calculated positions using riding models.

PLATON SQUEEZE calculations

For 1**A** SQUEEZE was used to account for guest molecules that could not be modelled. The structure for **1A** was refined against the modified .hkl file obtained from SQUEEZE. The residual electron density of 1160 is equivalent to 29 molecules of DMF per unit cell or 7.25 molecules of DMF per host formula unit, assuming that only DMF molecules are present as guests.

For **1B** and **1C** SQUEEZE was used only to calculate the total residual electron density present for each refined structure.

SQUEEZE result for **1B**:

```
_platon_squeeze_void_nr
_platon_squeeze_void_average_x
_platon_squeeze_void_average_y
_platon_squeeze_void_average_z
_platon_squeeze_void_volume
_platon_squeeze_void_count_electrons
_platon_squeeze_void_content
 1   0.000   0.190   0.000        10         0 ' '
 2   0.000   0.500   0.000        30         0 ' '
 3   0.000   0.810   0.000         9         0 ' '
 4   0.000   0.500   0.500        16         0 ' '
 5   0.500   0.000   0.000        30         0 ' '
 6   0.499   0.000   0.500        16         0 ' '
 7   0.500   0.310   0.000         9         0 ' '
```

```
   8  0.500  0.690  0.000        10          0 ' '
_platon_squeeze_void_probe_radius                  1.20
_platon_squeeze_details                           ?
```

SQUEEZE result for **1C**:

```
  _platon_squeeze_void_nr
  _platon_squeeze_void_average_x
  _platon_squeeze_void_average_y
  _platon_squeeze_void_average_z
  _platon_squeeze_void_volume
  _platon_squeeze_void_count_electrons
  _platon_squeeze_void_content
   1  0.117  0.649  0.496        24          3 ' '
   2  0.502  0.499  0.565       185          6 ' '
   3  0.347  0.110  0.496        23          3 ' '
   4  0.653  0.889  0.496        23          3 ' '
   5  0.889  0.347  0.496        23          3 ' '
_platon_squeeze_void_probe_radius                  1.20
_platon_squeeze_details                           ?
```

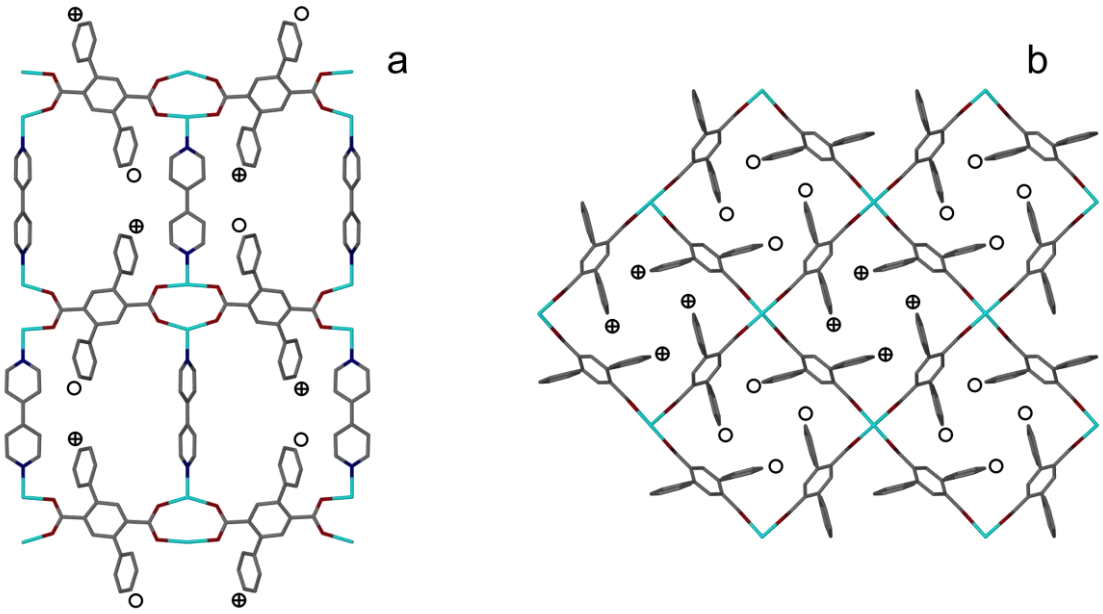

Figure S1. Partial packing diagrams for **1A** viewed along (a) [110] and (b) [001]. The circles containing plus signs and the empty circles denote phenyl rings above and below the plane, respectively. Guest molecules have been omitted for clarity.

Table S1. Crystallographic data and structure refinement parameters

Identification code	**1A**	**1B**	**1C**
Empirical formula	$C_{50}H_{32}N_2O_8Zn_2 \cdot 29C_3H_7NO$	$C_{50}H_{32}N_2O_8Zn_2$	$C_{50}H_{32}N_2O_8Zn_2$
Formula weight	919.52*	919.52	919.52
Temperature (K)	100(2)	100(2)	296(2)
Crystal system	tetragonal	orthorhombic	tetragonal
Space group	*P*4/*ncc*	*Cmmm*	*P*4
a (Å)	15.4030(4)	7.8499(6)	10.8893(7)
b (Å)	15.4030(4)	19.4380(14)	10.8893(7)
c (Å)	28.1736(7)	14.1432(10)	14.0416(9)
α (°)	90.00	90.00	90.00
Volume ($Å^3$)	6684.3(3)	2158.1(3)	1665.0(2)
Z	4	2	1
ρ_{calc} (g $cm^{-3)}$	0.914	1.415	0.917
μ (mm^{-1})	0.755	1.169	0.758
F(000)	1880.0	940.0	470.0
Crystal size (mm^3)	0.31 × 0.24 × 0.21	0.10 × 0.08 × 0.05	0.27 × 0.18 × 0.17
Radiation	MoKα (λ = 0.71073)	MoKα (λ = 0.71073)	MoKα (λ = 0.71073)
2θ range for data collection (°)	3.92 to 56.58	2.88 to 56.62	2.9 to 54.18
Index ranges	-20 ≤ h ≤ 20, -20 ≤ k ≤ 20, -36 ≤ l ≤ 37	-10 ≤ h ≤ 10, -25 ≤ k ≤ 25, -18 ≤ l ≤ 18	-13 ≤ h ≤ 13, -13 ≤ k ≤ 13, -17 ≤ l ≤ 17
Reflections collected	114948	32957	44680
Independent reflections	4160 [R_{int} = 0.0396, R_σ = 0.0152]	1535 [R_{int} = 0.0726, R_σ = 0.0265]	3692 [R_{int} = 0.0520, R_σ = 0.0241]
Completeness to θ_{max} (%)	99.8	99.7	99.9
Data/restraints/parameters	4160/0/142	1535/2/124	3692/187/194
Goodness-of-fit on F^2	1.077	1.046	1.242
Final R indexes [I>=2σ (I)]	R1 = 0.0452, wR2 = 0.1219	R1 = 0.0386, wR2 = 0.0885	R1 = 0.0431, wR2 = 0.0940
Final R indexes [all data]	R1 = 0.0505, wR2 = 0.1261	R1 = 0.0520, wR2 = 0.0951	R1 = 0.0571, wR2 = 0.1052
Largest diff. peak/hole (e $Å^{-3}$)	0.83/-0.35	0.73/-0.71	0.51/-0.90
Flack parameter			0.51(11)

**Framework only. Guest molecules could not be modelled.*

Thermogravimetric analysis (TGA)

TGA was carried out using a TA Instruments Q500 analyzer with constant N_2 flow at a rate of 50 cm^3 min^{-1}. Samples were loaded into aluminium sample pans and heated at 10 K min^{-1} from room temperature to decomposition. The mass loss of 30.0 % for **1A** is equivalent to 21.6 molecules of DMF per unit cell, which is consistent with the estimated value of 29 from the single-crystal X-ray structure, considering that DMF is lost rapidly at room temperature during TGA sample preparation.

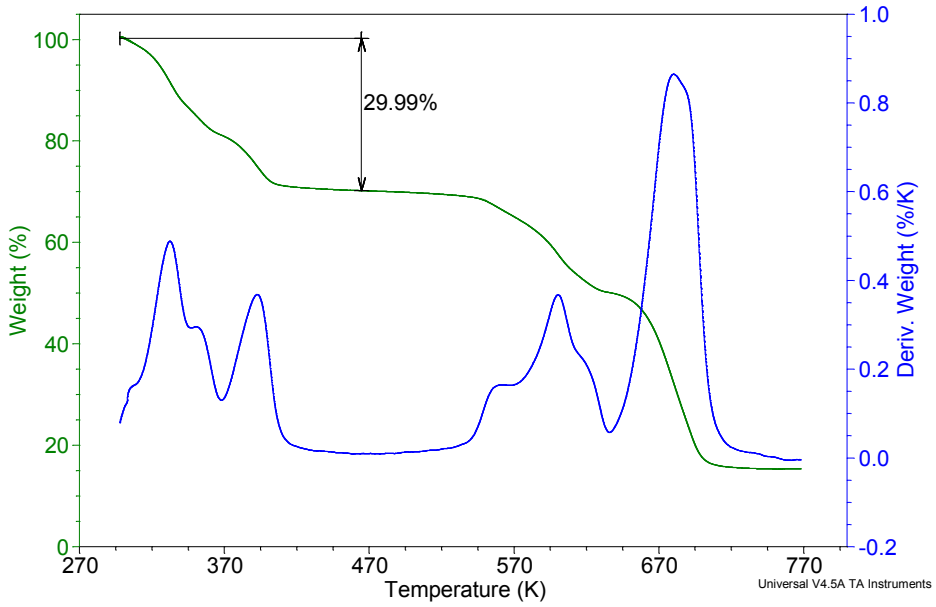

Figure S2. TGA trace for **1A**.

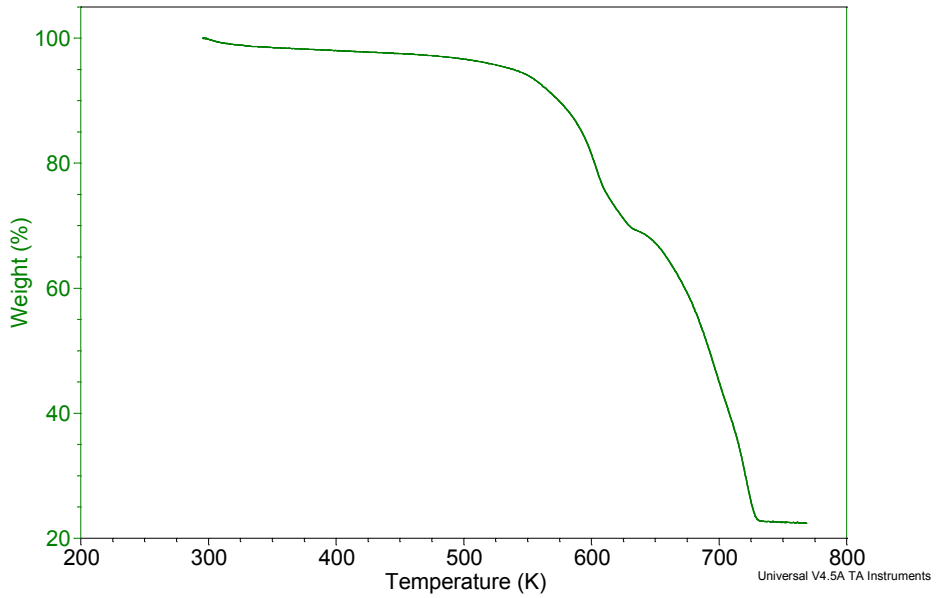

Figure S3. TGA trace for **1** after direct activation of **1A** at 423 K.

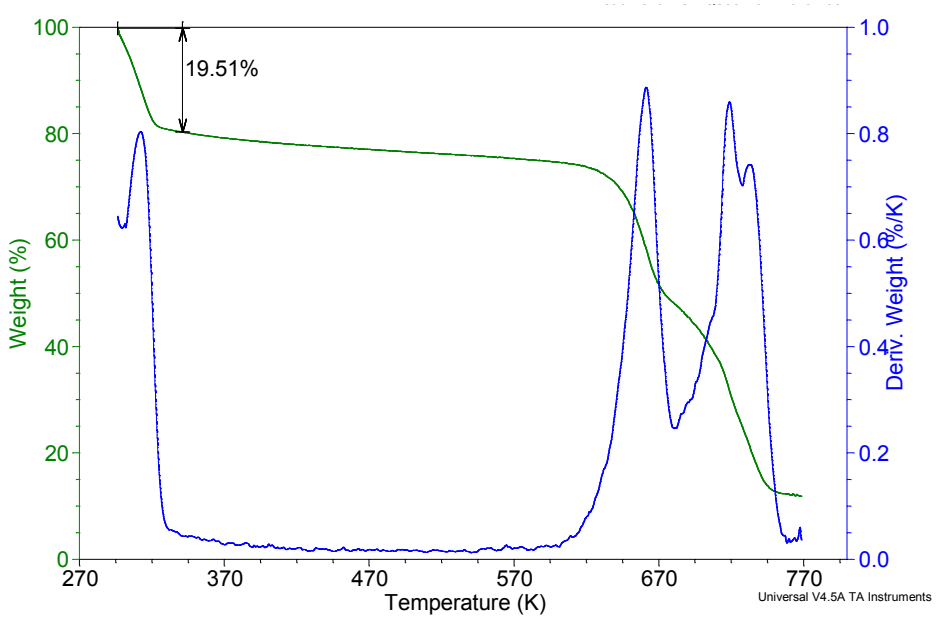

Figure S4. TGA trace for **1** after solvent exchange of **1A** with diethyl ether.

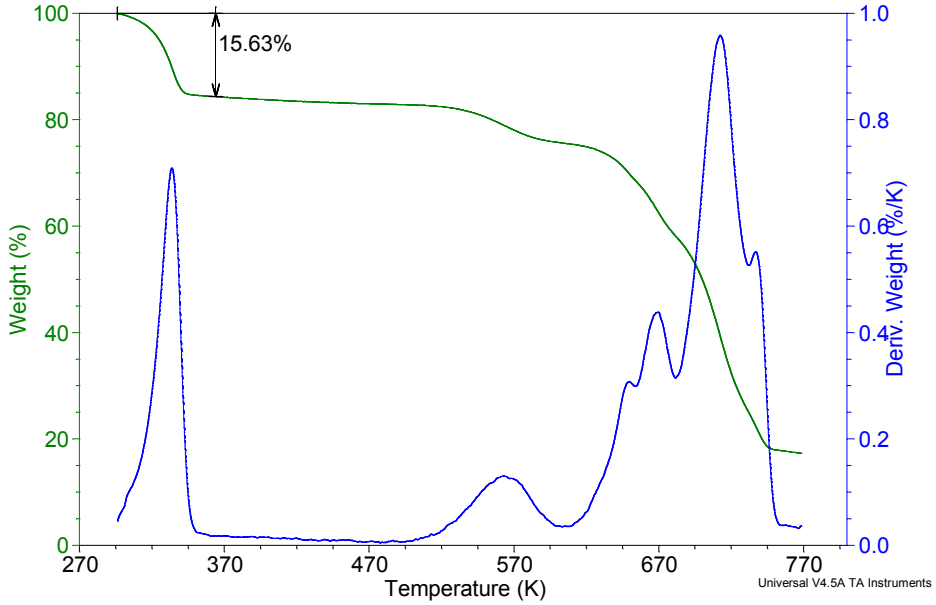

Figure S5. TGA trace of **1** after solvent exchange of **1A** with ethyl acetate.

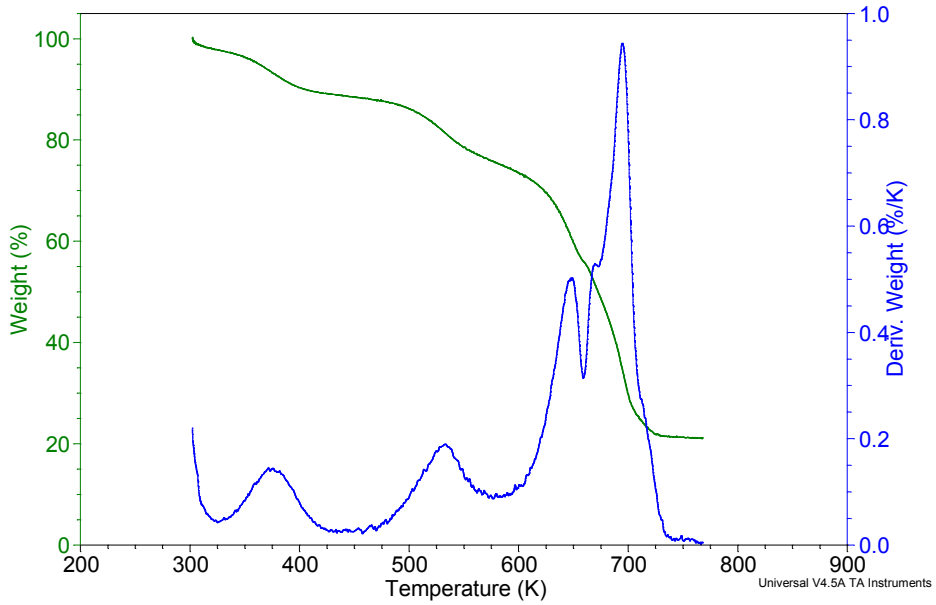

Figure S6. TGA trace for **1C** obtained from supercritical drying.

Powder X-ray diffraction (PXRD)

PXRD data at ambient pressure were collected using a Bruker D2 PHASER and a equipped with Lynxeye 1D detector and Ni-filtered Cu K_α radiation (λ = 1.5418 Å; 30 kV, 10 mA generator parameters; restricted by a 1.0 mm divergence slit and a 2.5 Soller collimator).

Pressure-resolved PXRD data (Figure S) were collected using Cu Kα radiation (λ= 1.5418 Å, 40 kV and 30 mA) on a PANalytical X'pert PRO instrument operating in Bragg-Brentano geometry. The sample was prepared in an environmental gas cell. Data were collected at 5 bar increments of CO_2 gas loading from vacuum to 50 bar with an equilibration time of at least 6 h allowed for each step.

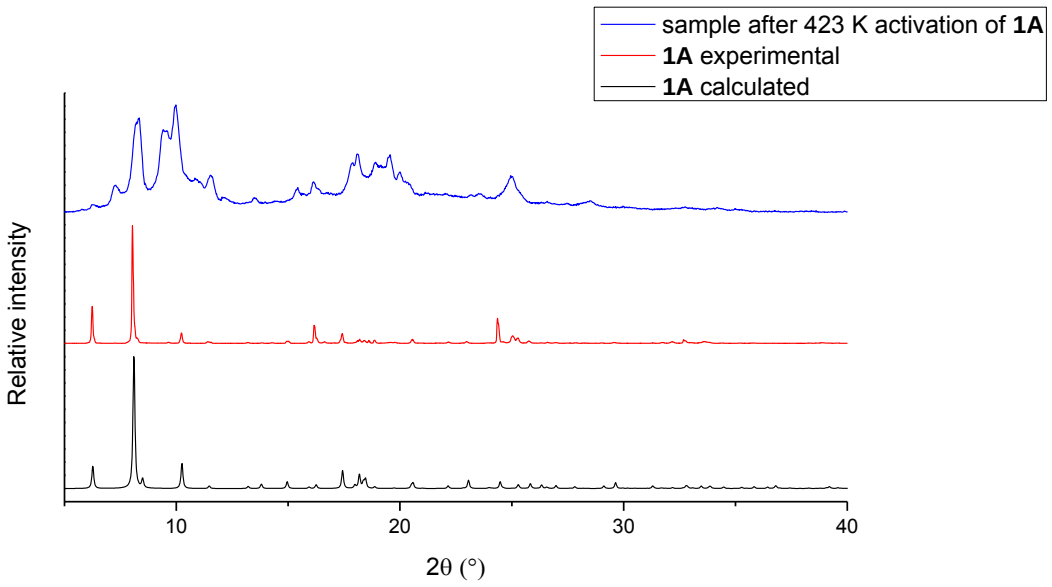

Figure S7. Comparison of the experimental patterns of **1A** calculated from single-crystal diffraction data, **1A** as synthesised and a sample after activation of **1A** at 423 K under dynamic vacuum.

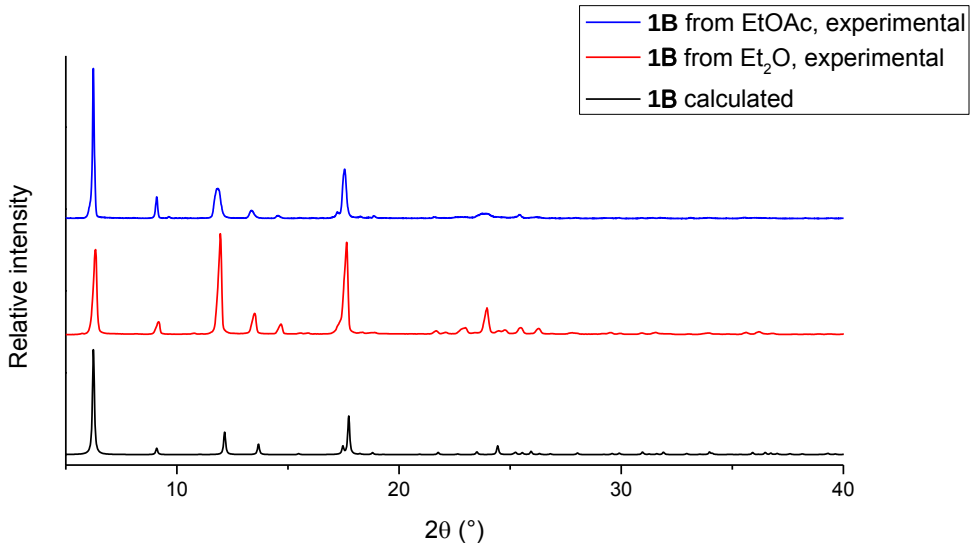

Figure S8. Experimental PXRD patterns of **1B**, obtained by activation via diethyl ether and ethyl acetate solvent exchange, compared with the **1B** pattern calculated from single-crystal diffraction data.

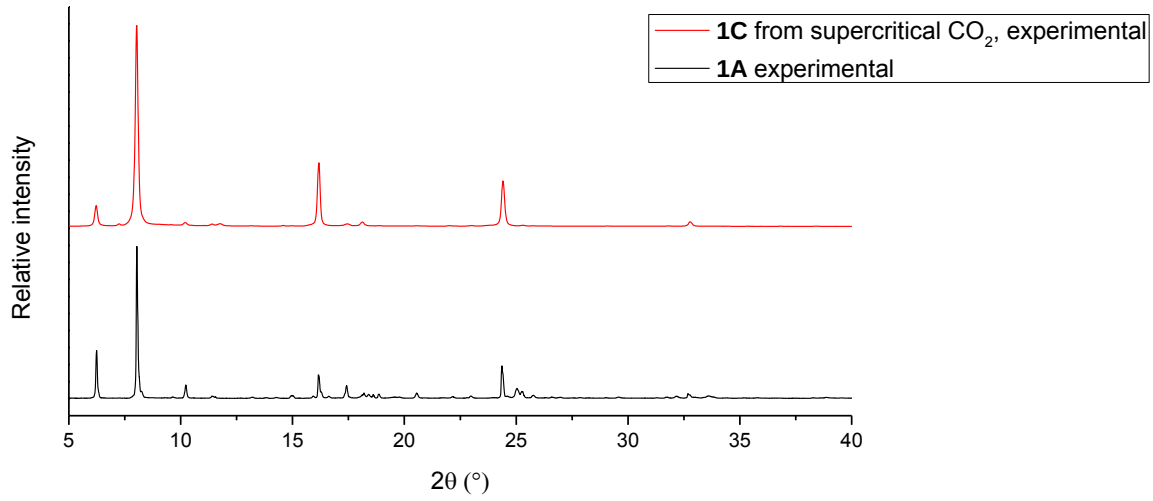

Figure S9. Experimental PXRD patterns of **1A** as synthesised and **1C** from supercritical drying.

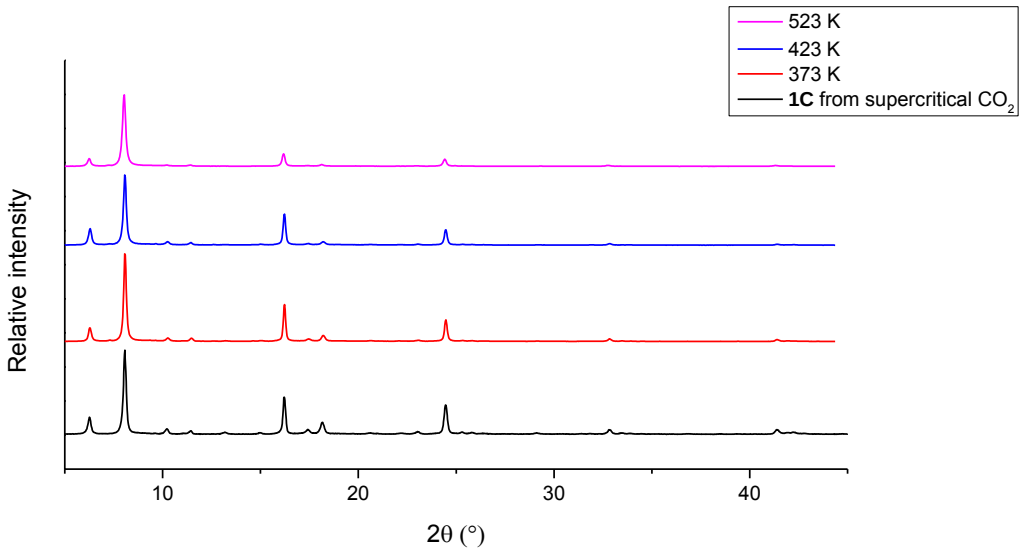

Figure S10. Comparison of PXRD patterns of **1C** from supercritical drying and heated under dynamic vacuum at 373, 423 K and 523 K.

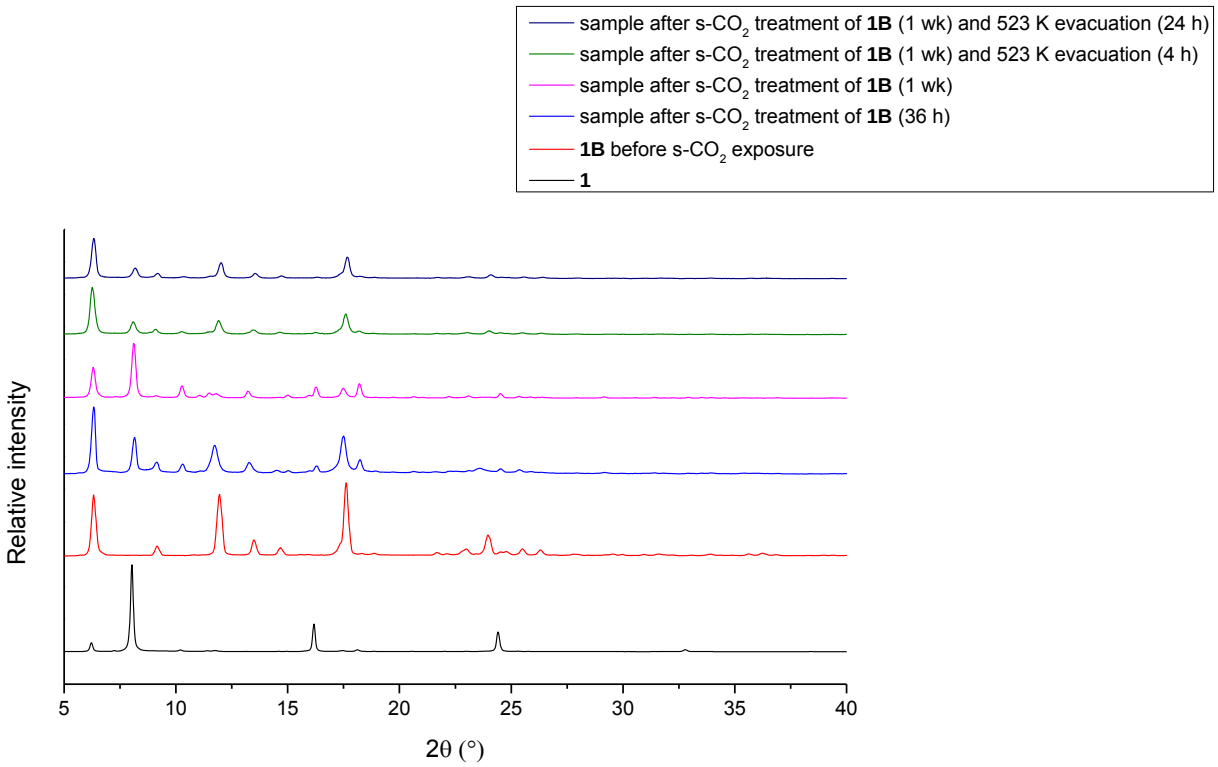

Figure S11. Experimental PXRD patterns of **1C** as obtained by supercritical drying of **1A**, **1B** before exposure to supercritical CO_2 and sample after various treatments of **1B** with supercritical CO_2 and high temperature evacuation.

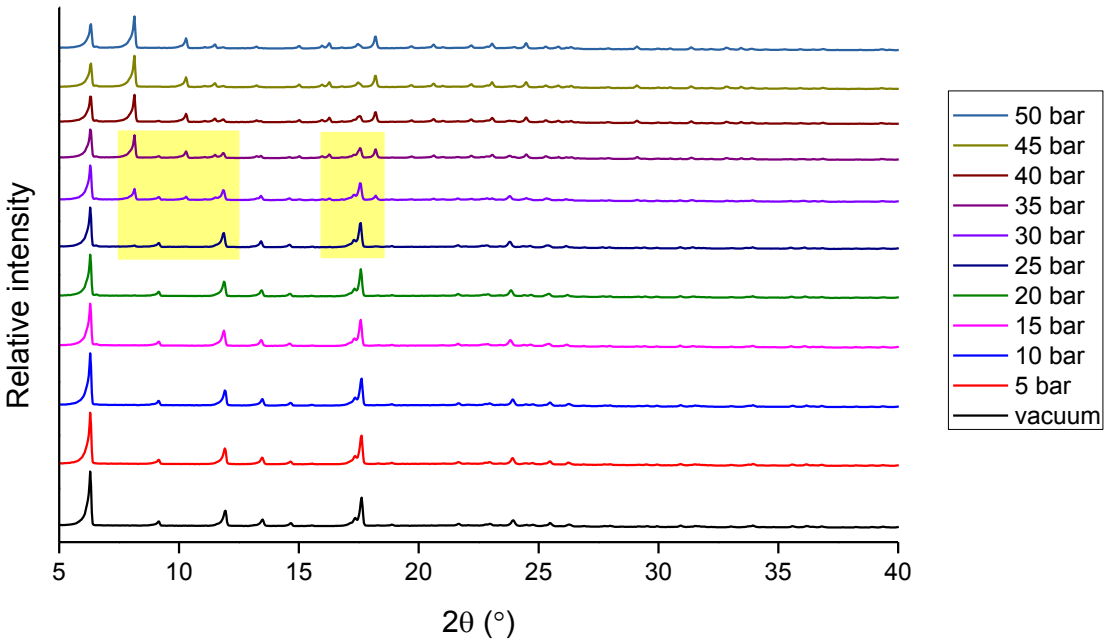

Figure S12. Pressure-resolved PXRD patterns for a sample of **1** that was loaded as form **1B** (vacuum) and pressurised in an environmental gas cell with CO_2 at 298 K.

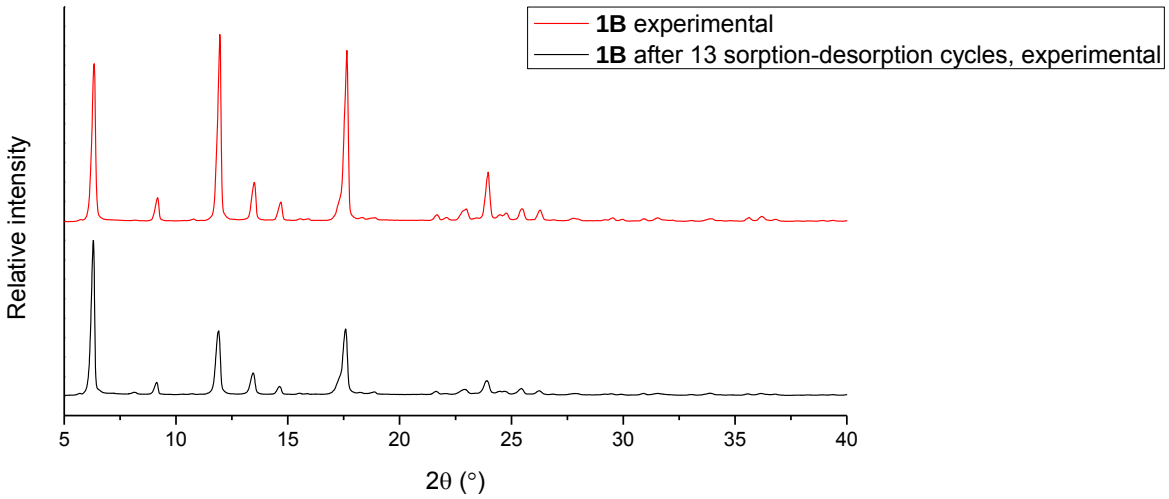

Figure S13. PXRD pattern of **1B** after 13 CO_2 sorption/desorption cycles on PCTPro-E&E gas sorption analyser.

FTIR

The FTIR spectrum was collected using a Thermo Nicolet iS10 spectrometer with ATR attachment.

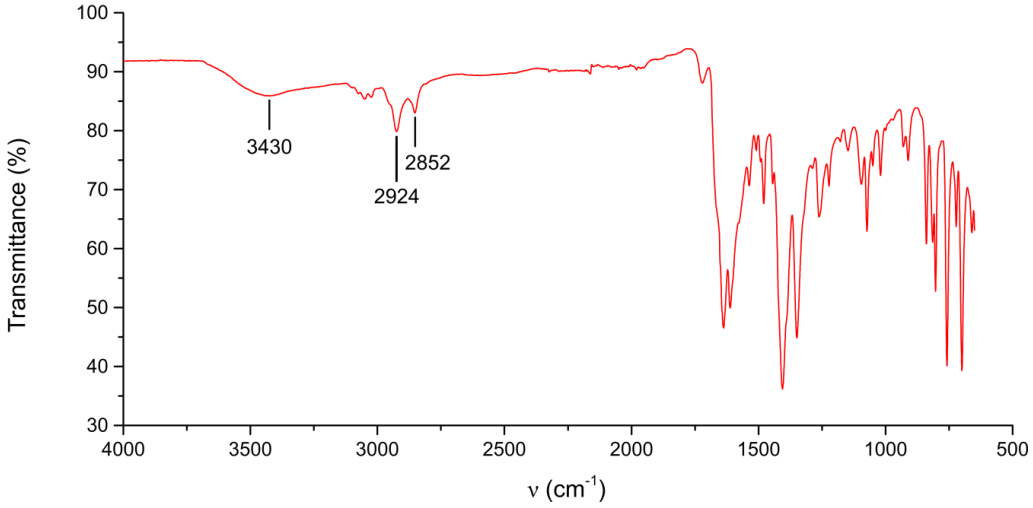

Figure S14. FTIR of **1C** obtained from supercritical drying.

NMR

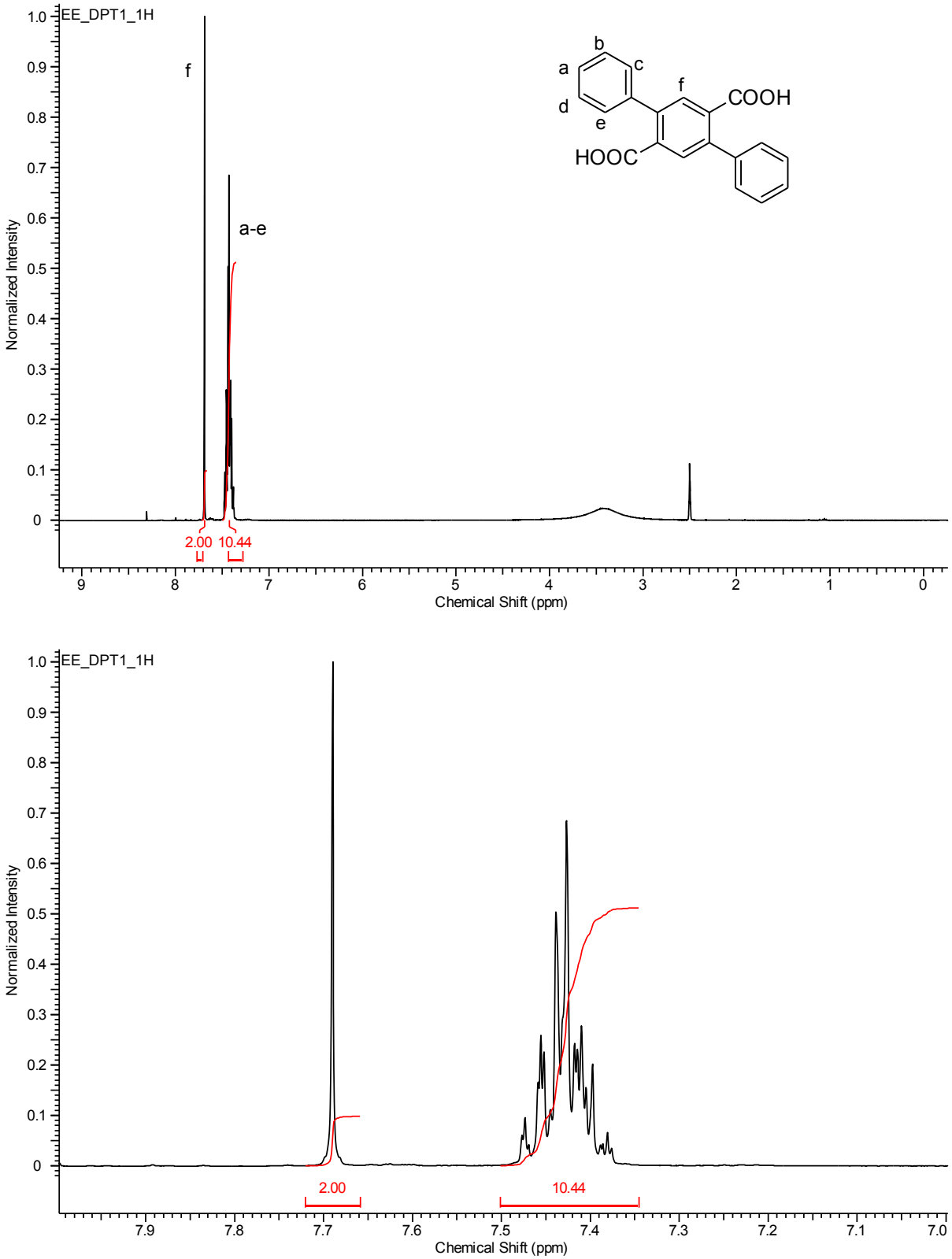

Figure S15. ^{1}H NMR for DPT (Varian Unity Inova, 400 MHz, DMSO-d6, 25 °C).

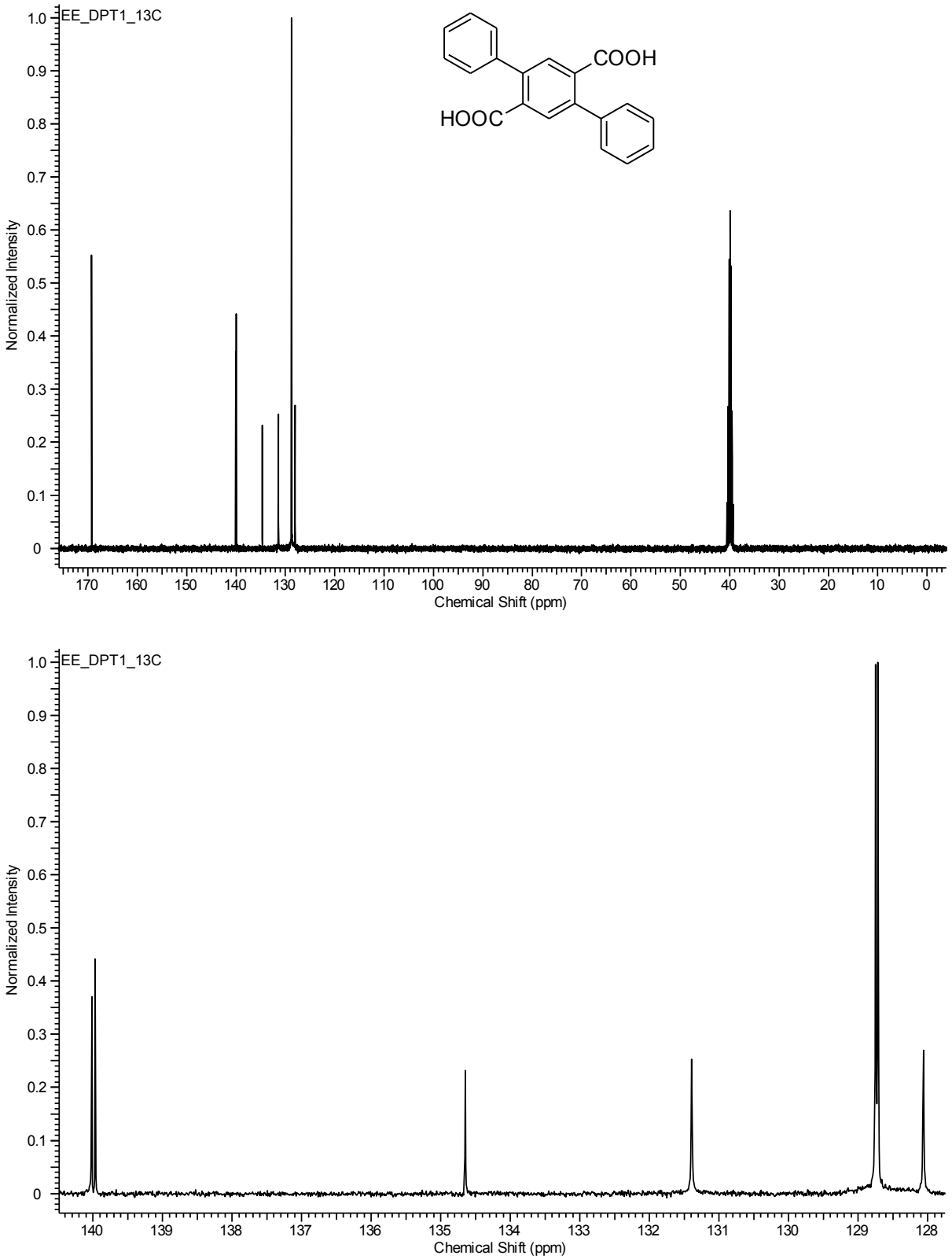

Figure S16. ^{13}C NMR for DPT (Varian Unity Inova, 100 MHz, DMSO-d6, 25 °C).

Sorption

Sorption data were collected using a Setaram PCTPro-E&E volumetric sorption analyser with MicroDoser attachment.

The freshly-activated sample of **1B** (65.0 mg) was outgassed for 12 h at 323 K before the first sorption run. Between sorption-desorption cycles, the sample was outgassed for 12 h at 298 K.

Sorption and desorption isotherms for MIL-53(Cr)[6] and COMOC-2[7] were reproduced using WebPlotDigitizer.[8]

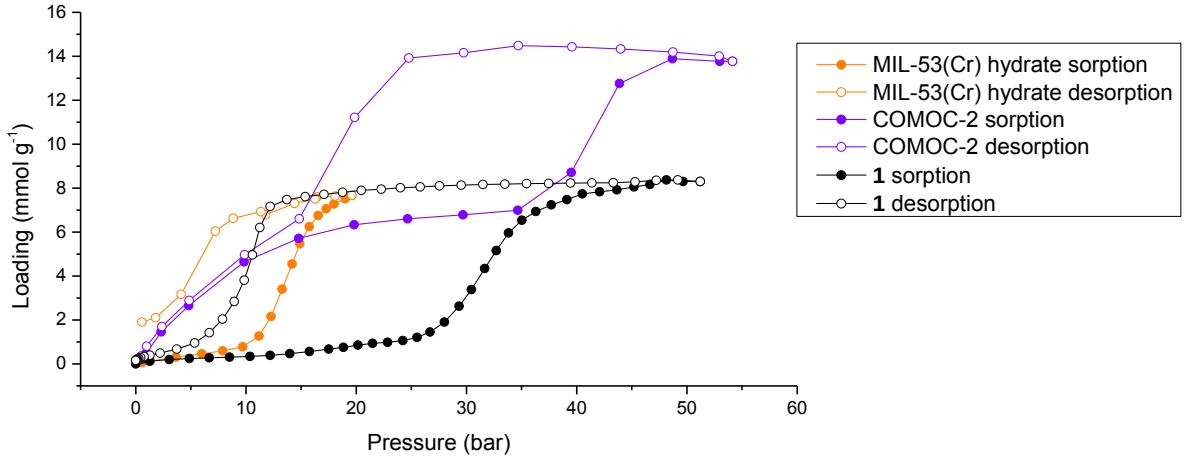

Figure S17. CO_2 sorption and desorption isotherms for MIL-53(Cr) at 304 K, COMOC-2 at 303 K and **1** at 298 K.

Pressure-DSC

Pressure-DSC refers to pressure-resolved differential scanning calorimetry. These experiments were carried out using a Setaram μDSC7 Evo module equipped with a high pressure sample holder. The instrument measures heat flow (like a conventional DSC) as a function of pressure. It was coupled to a Teledyne ISCO 260D syringe pump, controlled using software developed in-house and used to supply gas, ensuring a constant pressure gradient of 0.1 bar min^{-1}.

A sample of 34.7 g was used. Before cycle 1 and between sorption-desorption cycles, the sample was evacuated for 1 h at 353 K.

Note that for the plot of Maximum Integral Heat vs. Cycle Number (Figure 4 in main text) the maximum heat was divided by the sample mass.

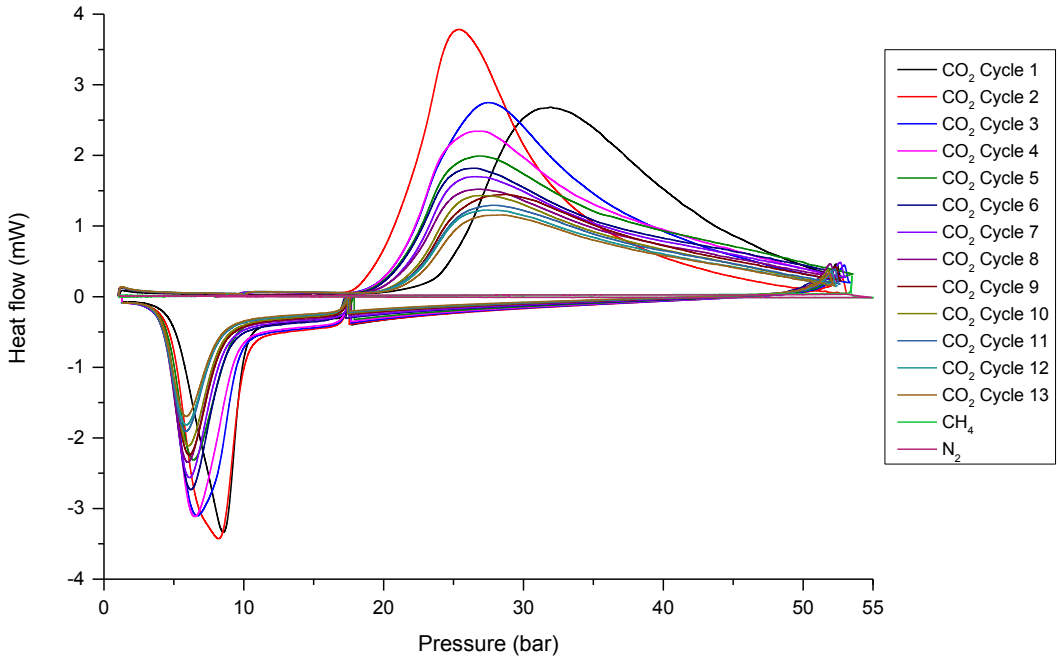

Figure S18. Pressure-DSC traces for **1** according to test gas and sorption/desorption cycle number.

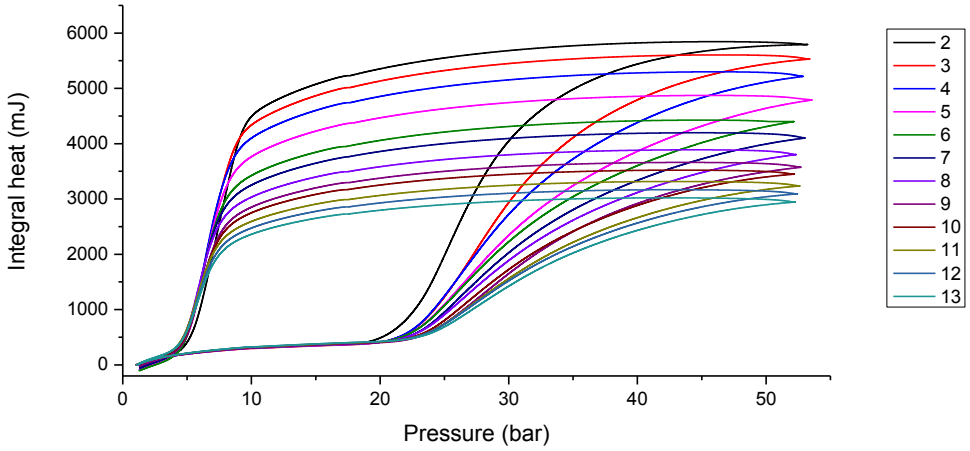

Figure S19. Integral heat vs. pressure for **1** according to the cycle number of CO_2 sorption/desorption cycles.

Table S2. Details of the fitted curve of maximum integral heat vs. cycle number (Figure 4 in main text)

Equation	$y = START + (END - START)\ \frac{x^n}{k^n + x^n}$	
Adj. R^2	0.99933	
	Value	**Standard Error**
START	160.34763	1.33653
END	61.92288	2.86115
k	6.81796	0.15095
n	2.35332	0.13124

SEM

SEM images were collected on a Zeiss Merlin FE instrument. The samples were prepared in a high-pressure steel vessel. A freshly prepared sample of **1B** was placed in the vessel and the vessel pressurised with CO_2 to 50 bar and allowed to equilibrate for at least 3 h. Thereafter the chamber was evacuated for a further 3 h. This procedure was repeated 20 times, with portions removed for SEM analysis before starting the experiment, after 5 cycles and after 20 cycles.

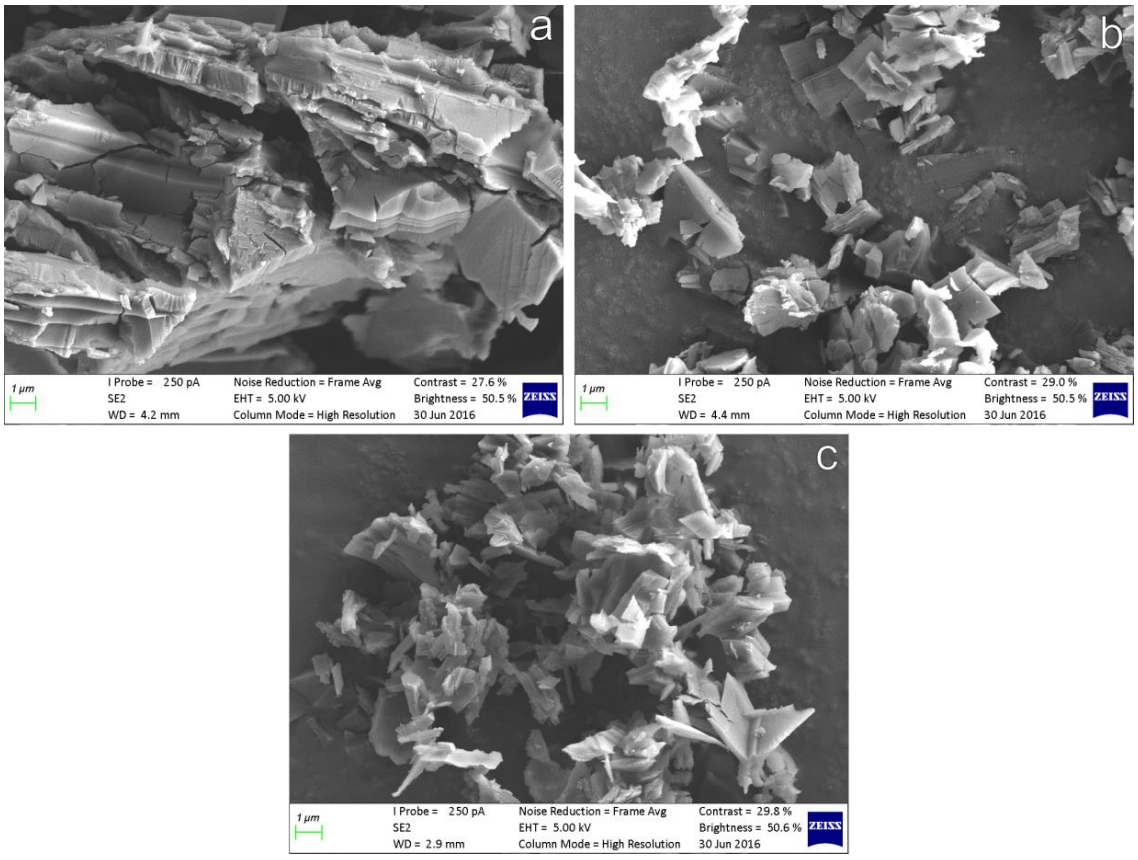

Figure S20. Comparative SEM images of samples of **1B** after (a) 0, (b) 5 and (c) 20 single-point sorption-desorption cycles of CO_2 up to 50 bar at 295 K.

References

1 Nakagawa, T.; Kumaki, D.; Nishida, J.; Tokito, S.; Yamashita, Y. *Chem. Mater.* **2008**, *20*, 2615.

2 *SAINT Data Reduction Software*, Version 6.45; Bruker AXS Inc., Madison, WI, 2003.

3 (a) *SADABS*, version 2.05; Bruker AXS Inc., Madison, WI, 2002. (b) Blessing, R. H. *Acta Crystallogr.* **1995**, *A51*, 33.

4 Sheldrick, G. M. *Acta Crystallogr.* **2008**, *A64*, 112.

5 Barbour, L. J. *Supramol. Chem.* **2001**, *1*, 189.

6 Llewellyn, P. L.; Bourrelly, S.; Serre, C.; Filinchuk, Y.; Férey, G. *Angew. Chemie Int. Ed.* **2006**, *45*, 7751.

7 Wang, G.; Leus, K.; Couck, S.; Tack, P.; Depauw, H.; Liu, Y.-Y.; Vincze, L.; Denayer, J. F. M.; Van Der Voort, P. *Dalton Trans.* **2016**, *45*, 9485.

8 Rohatgi, A. *WebPlotDigitizer*, Version 3.10; Austin, Texas, USA, 2016.

Chapter 6
Concluding remarks

Guest inclusion is a fundamental aspect of supramolecular chemistry that still holds enormous potential for scientific exploration. In this thesis, the investigation of guest effects on dynamic properties of solid-state inclusion compounds has been primarily concerned with anisotropic thermal expansion and porosity.

At first a simple known inclusion compound was investigated for which anisotropic thermal expansion had apparently been overlooked. Two structures of the same compound with large deviations in unit cell parameters had been flagged in a reported Cambridge Structural Database (CSD) search for polymorphs. Unusual thermal expansion behaviour for this compound was confirmed by temperature-resolved single-crystal X-ray diffraction. It transpired that the structure of an analogue of this solvate – with identical host and crystal packing but a different guest molecule – was present in the CSD. The known analogue was reproduced and a novel analogue prepared so that our thermal expansion study could be extended to an isoskeletal series. We had aimed to observe guest-dependent changes in thermal expansion behaviour, if any, and elucidate a general mechanism to account for thermal expansion across the series. Our remarkable results for these organic molecular inclusion compounds supported the prospect of using guest replacement to modulate solid-state properties. Encouraged, we decided to broaden our investigation of guest effects on dynamic solid-state properties to a different class of materials, namely MOFs. Given the prominence of MOFs in modern supramolecular chemistry, it was clear that controlling MOF properties via guest replacement would be attractive to a broad audience. We had also noted the abundance of literature reports on guest-responsive behaviour in MOFs. Our goal would be to probe the effects of solvent-mediated activation and supercritical CO_2 drying on structure and porosity. Gas sorption would provide another opportunity to interrogate guest effects, with the incoming gas serving as a potential new guest.

For the nitromethane solvate of 18-crown-6 (**18C6N**), exceptionally large uniaxial NTE and volumetric PTE were observed in the absence of strong directional interactions. For the isoskeletal series based on **18C6N** it was shown, for the first time for molecular inclusion compounds, that anisotropic thermal expansion could be greatly modified by guest replacement even where crystal packing remains unchanged.

The isoskeletal series that we described comprises solvates that are unstable at room temperature when removed from their mother liquor. Nevertheless, our results represent a

proof of concept. For the purpose of demonstrating practical utility under realistic operating conditions, the author recommends that a future study be focused on a series of compounds that *are* stable at room temperature and across a broad temperature range. Furthermore, the minimisation of side-on interactions will likely be associated with a less complex mechanism of anisotropic thermal expansion than seen here. The author recommends identifying a series where host-guest interactions are isolated within cavities. Typical clathrate compounds that show anisotropic thermal expansion and include a variety of guests would be ideal. For such a system it might be easier to identify a trend in thermal expansion based on guest properties, allowing for tunability.

The number and variety of novel MOFs that chemists have produced over the past two decades is staggering. At the time of writing, the SciFinder database contained 7570 publications (1995-2016) mentioning the term “metal-organic framework”. Including the related terms “coordination network” and “porous coordination polymer” adds thousands more articles. While the prospect of wide-ranging applications has contributed to the rapid proliferation of this relatively young area of chemistry, MOFs have arguably not yet lived up to their promise.

Our investigation of the MOF $[Zn_2(C_{20}H_{12}O_4)_2(C_{10}H_8N_2)]_n$ (**1**) highlights the importance of the method of activation when preparing a MOF for gas sorption. Direct activation, solvent-mediated activation and supercritical CO_2 drying yielded remarkably different activated phases. The phase obtained by activation after solvent exchange is a collapsed form that expands under CO_2 pressure. This sorption by *breathing* occurs via a gate-opening step with very broad hysteresis.

Solvent exchange is a simple method that might unlock alternative activated phases of MOFs that collapse upon direct activation. Specific research is needed to explain exactly how different solvent guests interact with frameworks before and during activation, and how these interactions might induce structural changes.

The hysteresis observed for **1** is among the largest ever observed but initial attempts at a quantitative comparison with previously-reported examples proved challenging. In MOF chemistry, hysteresis is a relatively common phenomenon that warrants greater scrutiny. The author has, with co-workers, begun an inquiry into the following:

- How has hysteresis been quantified in other fields?
- In chemistry, how might hysteresis be quantified for MOFs and other porous solids?
- Which MOFs exhibit the greatest hysteresis?

Our analysis, by pressure-DSC, of the effects of repeated sorption/desorption cycling is the first of its kind. The systematic decline in uptake capacity that we have revealed for **1** has

significant implications for MOFs as molecular storage and separation materials. It might be that, in addition to **1**, other flexible frameworks are susceptible to a decline in uptake capacity with repeated cycling. If the declining capacity is indeed related to damage caused to the framework under stress of breathing, the presence of labile coordination bonds, as in **1**, naturally increases the probability of this decline. More research into the effects of sorption/desorption cycling on MOFs is certainly warranted and our pressure-DSC method, which scans heat flow as a function of pressure, is ideal for such studies. Our method records data for multiple cycles far more rapidly than can be achieved by standard volumetric or gravimetric sorption analysis. As the drive towards application becomes more fervent, bold claims that a particular MOF will be ideal for industrial gas storage or separation by pressure swing adsorption really need to be accompanied by evidence that the material maintains high uptake capacity after many cycles of sorption and desorption.

Appendix

The attached disk contains the following supporting files and videos.

- Chapter 3:
  - CIF data files and CheckCIF reports
- Chapter 4:
  - CIF data files and CheckCIF reports
  - Video showing thermosalient behaviour of the acetonitrile solvate as a single-crystal
  - Video showing thermosalient behaviour of the acetonitrile solvate as a powder
  - Video showing concerted motion of columns of the nitromethane solvate
- Chapter 5:
  - CIF data files and CheckCIF reports